DEVELOPMENT OF IN-PLANE MODELS FOR THE ANALYSIS OF DEAD-ENDED AND ANODE BLEEDING OPERATION MODES AND THE CELL DEGRADATION WITH CARBON CORROSION

by
OMID BABAIE RIZVANDI

Submitted to the Graduate School of Engineering and Natural Sciences
in partial fulfillment of
the requirements for the degree of
Doctor of Philosophy

Sabanci University

July 2019

DEVELOPMENT OF IN-PLANE MODELS FOR THE ANALYSIS OF DEAD-ENDED AND ANODE BLEEDING OPERATION MODES AND THE CELL DEGRADATION WITH CARBON CORROSION

APPROVED BY:

Prof. Dr. Serhat Yeşilyurt
(Thesis Supervisor)

Prof. Dr. Selmiye Alkan Gürsel

Assoc. Prof. Dr. Güllü Kızıltaş Şendur

Prof. Dr. Ilker Tarı

Assoc. Prof. Dr. Mustafa Fazıl Serincan

DATE OF APPROVAL: 09/07/2019

ABSTRACT

DEVELOPMENT OF IN-PLANE MODELS FOR THE ANALYSIS OF DEAD-ENDED AND ANODE BLEEDING OPERATION MODES AND THE CELL DEGRADATION WITH CARBON CORROSION

OMID BABAIE RIZVANDI

Ph.D. Dissertation

Thesis Advisor: Prof. Dr. Serhat Yeşilyurt

Keywords: Proton exchange membrane fuel cell; Pseudo-three-dimensional model; Dead-ended anode operation mode; Anode bleeding operation mode; Carbon corrosion

Low durability and high cost are main drawbacks against commercialization of the proton exchange membrane fuel cell (PEMFC). The anode-bleeding (AB) operation mode offers a very high hydrogen utilization and cost reduction by eliminating additional components for the recovery of hydrogen in the flow-through mode and avoids the carbon corrosion reaction (CCR), which causes degradation of the catalyst layer and occurs typically when the bleeding rate is set to zero in the dead-ended (DEA) mode. Three-dimensional (3D) models are necessary for the analysis of PEMFCs. However, computational cost of 3D models is extremely high because of the strong nonlinearity due to complex interactions in the cell. In this dissertation, a pseudo-three-dimensional (P3D) two-phase and non-isothermal model is developed to reduce the computational cost and predict the cell performance with high accuracy. Results demonstrate that the P3D model results compare very well with ones from 3D model and experimental data from the literature. The P3D model is used to investigate the effects of geometric and operation parameters on the cell performance under DEA and AB operation modes. Moreover, the bleeding rate is optimized to sustain a stable transient cell voltage without the CCR in the cathode catalyst layer (CCL) while hydrogen utilization is kept at more than 99%. Furthermore, effects of the anode flow field design on the cell performance under the AB operation mode are investigated. Lastly, the P3D model is used to study effects of cell degradation on transport properties of the CCL.

ÖZET

ANOT-KAPALI VE ANOT-SIZINTILI ÇALIŞMA MODLARI İLE KARBON KOROZYONU SEBEBİYLE OLUŞAN HÜCRE BOZULMASININ ANALİZİ İÇİN AYNI-DÜZLEMSEL MODELLERİN GELİŞTİRİLMESİ

OMID BABAIE RIZVANDI

Ph.D. Tezi

Tez Danışmanı: Prof. Dr. Serhat Yeşilyurt

Anahtar kelimeler: Proton değişim membranlı yakıt pili, yalancı üç boyutlu model, anot-kapalı çalışma modu, anot-sızıntılı çalışma modu, karbon korozyonu

Dayanıklılık ve yüksek maliyet, proton değişim membranlı yakıt pillerinin (PDMYP) ticarileştirilebilmesi önündeki en büyük engellerdendir. Anot-sızıntılı (AS) çalışma modu, hidrojen geri kazanımı için gereken ek bileşenleri eleyerek çok yüksek hidrojen kullanım oranları ve düşük maliyetler sunar ve anot-kapalı (AK) modda sızıntı oranı sıfır olduğunda meydana gelen ve katalizör tabakanın aşınmasına sebep olan karbon korozyon reaksiyonunun (KKR) önlenmesini sağlar. PDMYP'lerin analizi için üç boyutlu modeller gerekmektedir. Fakat 3 boyutlu modellerde sayısal maliyet, yakıt hücresi içindeki kompleks etkileşimlerin sebep olduğu kuvvetli doğrusalsızlık sebebiyle oldukça fazladır. Bu tez önerisinde, sayısal maliyeti azaltmak ve hücre performansını yüksek doğrulukta tahmin edebilmek için yalancı üç-boyutsal (Y3B), iki fazlı ve izotermal olmayan bir model geliştirilmiştir. Elde edilen bulgulara göre Y3B modeli üç boyutlu modellerle ve deneysel verilerle çok iyi örtüşmektedir. Y3B modeli, geometri ve çalışma parametrelerinin AK ve AS modunda çalışan hücrelerin performansına etkisini araştırmak için kullanılmıştır. Ayrıca sızıntı miktarı, çalışma süresince stabil bir voltaj elde edilecek ve katot katalizör tabakada karbon korozyonuna sebep olmayacak ve aynı zamanda % 99'dan daha yüksek bir hidrojen kullanım oranı verecek şekilde optimize edilmiştir. Buna ek olarak, anot akış alanı tasarımının AS modunda çalışan hücrenin performansına etkileri araştırılmıştır. Son olarak, Y3B model, hücre yıpranmasının katot katalist tabakanın (KKT) taşınım özelliklerine olan etkisini çalışmak için kullanılmıştır.

… to Hana, my wife and best friend

ACKNOWLEDGMENTS

I would like to express my sincere gratitude and appreciation to my advisor Professor Dr. Serhat Yeşilyurt for his continuous support throughout this research and writing of this thesis. I would like to thank him for his patience, encouragement and guidance. I would also like to thank my committee members: Professor Dr. Selmiye Alkan Gürsel, Associate Professor Dr. Güllü Kızıltaş Şendur, Professor Dr. Ilker Tarı, and Associate Professor Dr. Mustafa Fazıl Serincan for serving as my committee members and their insightful comments and suggestions.

I would like to thank my beloved wife, Hana, and daughter, Sophia, for supporting me spiritually. Words cannot express how grateful I am to them.

TABLE OF CONTENTS

LIST OF FIGURES

LIST OF TABLES

LIST OF SYMBOLS AND ABBREVIATIONS

Abbreviation

AB	Anode bleeding
BOL	Beginning of life
BV	Butler-Volmer
CCR	Carbon corrosion reaction
Ch	Channel
CL	Catalyst layer
CCL	Cathode catalyst layer
DEA	Dead-ended anode
DOF	Number of degrees of freedom
ECSA	Electrochemical surface area
EOL	End of life
Eq	Equation
Exp	Experiment
FD	Finite difference
FT	Flow-through
GDL	Gas diffusion layer
HOR	Hydrogen oxidation reaction
IP	In-plane
MEA	Membrane electrode assembly
MPL	Micro-porous layer

OEA	Open-ended anode
ORR	Oxygen reduction reaction
P3D	Pseudo-three-dimensional
PEMFC	Proton exchange membrane fuel cell
RH	Relative humidity
seg	Segment
Sim	Simulation
St	Stoichiometric ratio
TP	Through-plane
ULF	Ultra-low flow
Ut	Utilization
sp-sp	Serpentine-serpentine
st-sp	Straight-serpentine
int-sp	Interdigitated-serpentine

Symbols

a	Water activity
c	Concentration (mol m^{-3})
D	Diffusion coefficient (m^2 s^{-1})
F	Faraday's constant (96485 C mol^{-1})
h	Height (m)
i	Volume reaction rate (A m^{-3})
J	Current density (A m^{-2})
k	Thermal conductivity (W m^{-1} K^{-1})
K	Permeability (m^2)
L	Length (m)

N	Mass flux (kg m^{-2} s^{-1})
n_d	Electro-osmotic drag coefficient
p	Pressure (Pa)
R	Universal gas constant (8.314 J mol^{-1} K^{-1})
Re	Reynolds number
R_{solid}	Electric resistance of the cell components (Ω m^2)
s	Water saturation
S	Source terms
T	Temperature (K)
$t_{0.5V}$	Time it takes for the cell voltage to drop to 0.5 V
$\mathbf{u}$	Velocity vector (m s^{-1})
V	Potential (V)
v	Molar volume (m^3 mol^{-1})
w	Width (m), mass fraction
x	Molar fraction

Greek letters

∇	Vector differential operator
δ	Thickness
ρ	Density
σ	Electrical conductivity, surface tension
θ	Contact angle
μ	Dynamic viscosity
ε	Porosity
α	Charge transfer coefficient
Φ	Thiele modulus of the spherical pellets

ϕ	Potential
λ	Water content in the electrolyte
η	Activation overpotential

Subscripts and superscripts

ads	Adsorption
an	Anode
av	Average
C	Carbon
c	Capillary
ca	Cathode
ch	Channel
cond	Condensation
conv	Convective
des	Desorption
diff	Diffusive
eff	Effective
eq	Equilibrium
evap	Evaporation
f	Fluid
g	Gas
in	In-plane
l	Liquid
m	Electrolyte
mem	Membrane
Naf	Nafion

pell	Pellet
ref	Reference
rev	Reversible
s	Solid
th	Through-plane

Chapter 1

INTRODUCTION AND LITERATURE REVIEW

1.1. Background and motivation

The proton exchange membrane fuel cell (PEMFC) is one of the most promising energy conversion devices that can be used for stationary and portable applications due to its high efficiency, high energy density, low operating temperature, fast startup, and zero emission of greenhouse gasses. However, progress is necessary to improve its durability and reduce the cost of energy delivered by PEMFC to accelerate its commercialization. High platinum content of the catalyst layers (CL) and components used in the hydrogen storage play a major role in the high cost of the PEMFC. Therefore, while lowering the platinum loading, hydrogen utilization must be improved without causing a performance loss due to the carbon corrosion and the platinum degradation in the CLs. While the PEMFC lasts more than 30,000 hours for stationary applications, which do not require frequent load changes, it lasts about 3000 hours for automotive applications [1,2].

Three dimensional (3D) models are necessary for the flow field design and analysis of PEMFCs such as water and thermal management. PEMFC models must consider several phenomena such as mass, momentum, heat and charge transport, electrochemical reactions and phase change to predict the cell performance. Therefore, the computational cost of 3D models is extremely high because of complex interactions of the model variables in each layer of the cell and between the layers. Numerous studies can be found in the literature using 1D and 2D-through-plane models for the analysis of PEMFCs. However, these models do not give information about the in-plane distributions of the model variables, which are essential for the flow field design and degradation analysis of PEMFCs. Therefore, novel modeling approaches with lower computational cost and high accuracy in predicting the cell performance are essential.

1.2. Literature review on PEMFC modeling

Due to complexity of interactions between the distributions of gas species, liquid water, current density and temperature in the layers of PEMFC, computational cost of 3D models of a full PEMFC is too restrictive for design optimization of flow fields as well as analysis of the cell. Therefore, physical complexity of PEMFC is studied with 1D or 2D models to attain insight in a reasonable computational time [3-11]. Typically, 3D models are either limited to portions of a PEMFC, [12-18], or based on simplifying assumptions of the underlying physics such as isothermal and single-phase transport [19-22].

Some of the recent studies include the development of a 3D model by Rostami et al. [18] to investigate the effect of the bend size of the serpentine flow fields on the PEMFC performance. Authors used single-phase assumption to model the flow, mass transport, and electrochemical reactions kinetics for a single turn of a serpentine gas channel and active area of 20 mm^2 with 400K elements in the numerical mesh. Vazifeshenas et al. [21] developed a 3D model to study the effectiveness of a novel compound flow field design in comparison to common parallel and serpentine designs based on single-phase model of a PEMFC with an active area of 25 cm^2 and with 690 K elements in the numerical mesh. Hu et al. [13] developed a 3D model to study the distribution of flow and species, and electrochemical reaction kinetics of a PEMFC with interdigitated and conventional flow fields. They used about 400 K elements to mesh the PEMFC which consists of a single channel with the length and width of 6 and 0.07 cm and half of the ribs on each side of the channel and other components between them. Karvonen et al. [19] developed two- and three-dimensional models of only cathode flow field to improve the existing parallel channel design and showing its effects on the uniformity of the velocity profile in gas channels, with a numerical mesh that consists of 1.2M degrees-of-freedom (DOF) for a 12 by12.6 cm flow field. Yesilyurt [16] developed a transient three-dimensional, single-phase, and iso-thermal model of a U-section of a PEMFC with an active area of 1.2 cm^2 and serpentine flow fields for the anode and cathode to study transient responses of the cell against the step changes in the load (cell voltage), cathode pressure drop, and relative humidity of the reactant at the cathode inlet. In our previous work [23], we developed a 3D

model with 3M DOF for the anode flow field with parallel channels to investigate an optimum feed and exhaust headers design for a uniform flow distribution in a PEMFC with straight channels and active area of 336 cm^2.

A vast number of two-dimensional models of PEMFC in literature, e.g. [8-11], are for studying the distribution of concentrations of gas species, liquid water saturation, temperature, current density, deformation and stresses in the through-plane (TP) direction. However, these models cannot be used to investigate the in-plane (IP) distributions. Raj et al. [24] compared distributions from 3D and 2D-TP models and observed significant multidimensional effects near the cathode channel for high current densities and low stoichiometric flow ratios for the cathode.

Recently, Nandjou et al. [25] developed a P3D model of a PEMFC to investigate the temperature and humidity distributions and the effect of the flow field design on the water and thermal management of the cell. Authors considered the flow distribution and transport equations in all layers of the cell including channels, gas diffusion layers (GDLs), micro-porous layers (MPLs), and the catalyst layers (CLs), and compared the polarization curves, and current density and temperature distributions from the model with experimental data from a 220-cm^2 PEMFC. In our previous work [26] we developed a single-phase, isothermal P3D model for a small cell that consists of 8 parallel channels and a double serpentine for the anode and cathode flow fields, respectively, an active area of 1.3 cm^2. Flow and species distributions are obtained in the channels and GDLs, and through-plane resistive relations are used to obtain species concentrations in the CLs from the GDLs since in-plane distributions are not changed notably in very thin layers such as CLs. The model was validated by comparing the polarization curve from the model against the one reported by Ye & Van Nguyen [15]. Moreover, we investigated the effects of the stoichiometric ratios of the anode and cathode flows on the cell performance, hydrogen utilization, and species distributions over the active area.

1.3. Literature review on operation modes of the anode

Common modes of the PEMFC operation are the dead-ended anode (DEA) operation, which closes the anode exit [27-30], and the flow-through mode that relies on the recovery and recirculation of the fuel in the anode [31-35]. In both operation modes, intermittent purge strategies are necessary to discharge nitrogen and liquid water to avoid fuel starvation [36-38].

Several studies have been conducted to investigate the effects of the operation parameters on the cell performance under the DEA operation mode, e.g. [39-42]. Yang et al. [39] experimentally studied the effects of the operation parameters on cell performance under DEA operation. The authors report that the average time between two successive purges, i.e. the mean purge-interval, decreases with the cell current density and the relative humidity of the cathode reactants and increases with the anode pressure and the stoichiometric flow ratio at the cathode inlet. Lee et al. [40] experimentally investigated the effects of operation parameters on water transport across the membrane under DEA operation. They visually observed the accumulation of liquid water in the anode flow field and measured the cell voltage during transients. The authors report that the voltage drop increases with the cell current density and humidity of the reactants, and it takes longer for the voltage to drop to 0.2 V as the flow stoichiometric ratio at the cathode inlet increases. Similar effects of the operation parameters on the cell performance are reported in transient studies of the DEA operation with two-phase models of the PEMFC [41,42].

Anode bleeding (AB) is another operation mode used to achieve high hydrogen utilization by allowing a continuous ultra-low flow (ULF) at the anode exit to discharge nitrogen and liquid water while maintaining a very high level of hydrogen utilization [31,43-48]. Recently, Eskin and Yesilyurt [45] developed an experimental setup to control the bleeding rate with high precision to achieve very high utilization of hydrogen and a stable cell voltage. The authors achieved utilization rates of 99.88% and 99.74% for the cells with active areas of 25 and 8.17 cm^2, respectively, with a stable cell voltage transient by operating the anode side with a pressure of 1 atm higher than the cathode side, which decreases the nitrogen crossover through the membrane to the anode side. Meyer et al. [48]

operated a lab scale PEMFC stack with 5 cells having an active area of 60 cm^2. An optimum hydrogen utilization of 95.5% was obtained for the bleeding rate of 1.77% and the anode pressure of 0.43 bar more than the cathode side.

Anode bleeding was coupled with the fuel recirculation operation mode by bleeding the anode outlet before the connection with the inlet [31,46,47]. Rabbani et al. [46] developed a dynamic model of the PEMFC to study the effects of different purge strategies on the cell performance including the fixed purge-interval, automated purge based on the level of nitrogen at the anode exit, and anode bleeding. According to the authors [46], bleeding rate of 3% is enough to limit the nitrogen concentration at the anode flow field to less than 1%. Steinberger et al. [47] studied the anode recirculation in a PEMFC with nitrogen in the feed gas to investigate the effects of discontinuous and continuous (bleeding) purge strategies on the utilization of fuel. The authors reported that AB is an efficient and simple strategy to operate the anode side with up to 30% nitrogen in the anode feed gas achieving a fuel utilization between 80 and 100%. Wang et al. [31] developed a quasi-two-dimensional transient model of a PEMFC with anode recirculation to optimize discontinuous and continuous purge strategies. The authors reported that anode bleeding of 3% is optimal for the energy efficiency of the system, and bleeding rates more than 5% have a negligible effect.

1.4. Literature review on flow field design

Considerable research and development have been targeted on the optimization of the flow field configurations such as parallel, serpentine, interdigitated, and combined designs, e.g. [49-53]. A single serpentine channel may lead to uniform distribution of the reactants over the active area, but causes a high pressure drop and parasitic power loss [54]. Parallel straight channels offer a low pressure drop, about an order of magnitude less than a serpentine channel, but have an intrinsic flow maldistribution problem that results in starvation of the reactant gases in portions of the active area [55-60]. Interdigitated flow fields improve the liquid water removal from the GDLs and enhance the transport of

reactants from the channels to the CLs, as first proposed by Nguyen [61], but operates at high pressure drops. Flow non-uniformity of the parallel straight channels flow fields can be improved by utilizing the feed and exhaust headers configurations [53,62-64]. Shimpalee and co-workers [65-67] studied the effect of the channel length and the number of the channels, channel and rib dimensions, and different serpentine flow field configurations on the cell performance and uniformity of the reactants and current density over the active area.

Maharudrayya et al. [50] studied one-dimensional steady model of the Z and U-type parallel channel configurations. Authors investigated the effect of dimensions of the channels and configurations of the feed and exhaust headers on the uniformity of the flow distribution in the channels. For the assessment of the uniformity of the flow distribution, they used two performance metrics as the normalized difference between the maximum and minimum flow rates of the channels, and the rms (root mean square) of these flow rates. They reported that uniformity of the flow can be improved efficiently by an appropriate design of the feed and exhaust headers as well as channels geometries. Kee et al. [52] studied one-dimensional channel network model of the flow distribution in the solid oxide fuel cells. Authors illustrated the importance of the effect of the pressure distribution in the headers on the uniformity of the flow distribution through the channels; similar study was done by [50]. Wei et al. [63] developed an evolutionary algorithm to optimize the configuration of the baffles in the feed and exhaust headers of the flow field for uniform flow distribution through the channels. Jackson et al. [53] studied a network model of the flow distribution of the Z-type channel configurations. They demonstrated that typical maldistribution occurs in the middle channels, which can be improved to a uniform flow distribution in the channels by increasing the widths of the feed and exhaust headers.

Watkins et al. [68] suggested a single serpentine channel for the flow field which connects to the inlet and outlet manifolds from its ends. This design yields a long path of the reactants flow which results in significant pressure loss and considerable flow gradients between the inlet and outlet manifolds. Furthermore, the water flooding (blockage) is possible in this design, since all water droplets are formed and accumulated in a single channel and more power is needed to remove them from the channel. Authors found that by

using some parallel serpentine channels the mentioned disadvantages of a single serpentine channel can be improved [69]. By changing the number of the serpentine channels, the desired pressure drop can be achieved. They claimed that the performance of the cell can be increased 50% by using serpentine channels for the flow field. In a similar study, Li et al. [70] studied serpentine flow fields with the active areas of 50, 100, 200, 300, and 441 cm^2. Authors reported that using serpentine channels enhance the performance of the cell since they remove the liquid water formed in the cell effectively. Their results of the neutron imaging technique indicate no liquid water in the cell for the mentioned cases.

1.5. Literature review on carbon corrosion and cell degradation

Carbon materials such as Black pearls BP2000, Ketjen black, and Vulcan-XC 72 are widely used as the catalyst support in the PEMFC due to their high thermal and electrical conductivity and low cost [71]. However, these alternatives are all prone to the carbon corrosion reaction (CCR) and have similar degradation properties due to the low equilibrium potential (0.207 V) of the CCR.

In automotive applications, 90% of cell degradation is attributed to fast load transients and frequent cycles of start-up and shut-down [72]. One of the important mechanisms causing cell degradation is the hydrogen starvation that takes place during these transients. Nitrogen and oxygen diffuse through the membrane from the cathode and form a hydrogen-air interface in the anode and cause the reverse current mechanism in the cell as described by Reiser et al. [73]. The hydrogen-air interface in the anode flow field divides the cell into active and passive parts. The active part operates normally with hydrogen oxidation reaction (HOR) at the anode and oxygen reduction reaction (ORR) at the cathode. In the passive part, due to the lack of hydrogen and the presence of oxygen and nitrogen in the anode, ORR takes place in the anode and carbon corrosion and oxygen evolution reactions (CCR and OER, respectively) in the cathode, hence the current is reversed. The corrosion reaction in the cathode catalyst layer (CCL) takes place in the carbon support for platinum nanoparticles and results in a reduction of the electrochemical

surface area (ECSA), loss of the hydrophobicity, and clogging of the pores by liquid water or the ionomer, thus the transport resistance of the CCL increases [74-79]. It is believed that the carbon corrosion in the CCL is one of the important degradation mechanisms in PEM fuel cells [80].

Reiser et al. [73] developed a one-dimensional model to describe the potential profile during the start-up of the cell because of the CCR. According to the authors, the local electrolyte potential drops to -0.59 V in the hydrogen-starved region of the cell where the cathode interfacial potential can be as high as 1.44 V, which favors the CCR. These findings have been confirmed experimentally by [81-84]. Meyers et al. [85] developed a one-dimensional model with resistive relations for species transport in the through-plane (TP) direction to investigate both CCR and OER under conditions of maldistribution of the hydrogen along the anode electrode in steady state and transient operations. The authors reported that CCR and OER are negligible when the hydrogen distribution is uniform, whereas these reactions lead to significant damage to the CCL when there is local starvation of hydrogen.

Several studies have been conducted to investigate the effects of the CCR on cell performance. Tang et al. [86] used a scanning electron microscope to observe the CCL under frequent start-up and shut-down cycles. The experiments revealed that the thickness of the CCL is reduced to about one-third of its initial thickness due to CCR. Lin et al. [87] observed about a 60% drop in the CCL thickness near the anode outlet, where the hydrogen starvation is expected the most, after 1800 start-up cycles. Apart from the start-up and shut-down cycling, load transients, DEA operation, and the clogging of the anode flow field due to the accumulation of liquid water also cause local starvation [88-91]. Chen et al. [92] developed a one-dimensional, isothermal and along-the-channel model to investigate the effects of the DEA operation on the CCR and the performance of a cell. The authors included the crossover and accumulation of nitrogen and oxygen in the anode, and the decrease in the ECSA using a power-law relationship based on the ratio of the remaining carbon and its initial level. Authors also reported that the corrosion rate at the anode exit is at least twice as high as at the inlet right before the purge and a non-recoverable voltage loss due to the CCR. Kulikovsky [93] developed a physical model of the CL performance

for the polarization curve prediction to quantify the changes in the model parameters (oxygen diffusivity, proton conductivity, and exchange current density) by adjusting these parameters for the polarization curves fitting before and after the degradation of the cell. According to that study [93], the exchange current density does not change significantly while the oxygen diffusivity and proton conductivity of the cathode CL change dramatically. Dhanushkodi et al. [94] developed a CCR kinetic model to evaluate the carbon loss during accelerated stress tests (AST). The authors suggested an exponential relation for the performance losses as a function of the carbon loss.

Chapter 2

A PSEUDO-THREE-DIMENSIONAL, TWO-PHASE, AND NON-ISOTHERMAL MODEL FOR PEM FUEL CELL

Three-dimensional (3D) models of the proton exchange membrane fuel cell (PEMFC) are necessary to study important issues such as water and thermal management and flow field design, but not practical due to computational cost of simulation of a full cell. In this chapter, a pseudo-three-dimensional (P3D) model is developed to mitigate the computational cost of 3D models. The model includes in-plane (IP) transport equations in channels and gas diffusion layers explicitly, and through-plane (TP) transport is based on resistance relationships through the thin membrane and catalyst layers. Polarization curves and distributions of species for a small section of a fuel cell that consists of straight channels, gas diffusion layers (GDL), catalyst layers (CLs) and the membrane are compared with the results from a full 3D model of the same cell for the variations in the channel height, GDL thickness, widths of the channels and ribs, operation temperature, and relative humidity of the reactant gases at the inlets. Overall, results from the P3D model compare very well with the ones from the full 3D model.

2.1. Methodology

A small section of a PEMFC that has straight channels on each side, as shown in Fig. 1, is used to demonstrate the essential elements of the approach without loss of generality, and to make comprehensive comparisons between the 3D and P3D models. Because of the symmetry between the anode and cathode sides, channels and ribs on both sides overlap. However, this is not necessary for the general case of different flow fields, [26]. In the resulting 2D domain, height-averaged conservation equations of mass, momentum, species,

liquid water, charge, and energy are coupled and solved together. Through-plane (TP) fluxes are treated as reactions and membrane is modeled as a thin-layer that resists against transport of protons (ionic current) and conducts dissolved water by adsorption and desorption at the anode and cathode CLs.

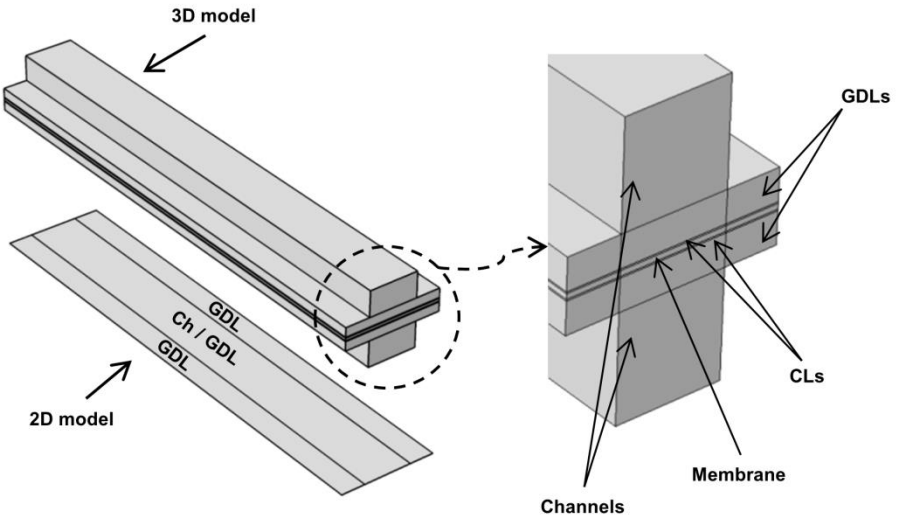

Figure 1: Computational domains for the 3D and P3D models; channels and GDLs are projected on a single surface to form the computational domain for the P3D model

2.1.1. Governing equations

Navier-Stokes equations are used to obtain the velocity field in the channels and Brinkman correction is used for the porous media, Maxwell-Stefan equations for the transport of gas species by diffusion and advection, and Butler-Volmer equations are used for the anode electrochemical reactions and an agglomerate model is used for cathode kinetics. Diffusion of liquid water saturation in the cathode side, dissolved water generation and transport through the membrane, and temperature distribution are also included in the model.

In the following discussion, 3D model equations are described first, and then the details of the P3D implementation are given. Cell geometric parameters and operation condition are listed in Table 1, and model parameters and values are listed in Table 2.

Table 1: Cell geometry and operating conditions

Parameter	Value	Description
L	1×10^{-2} m	Channel length
w_{ch}	1×10^{-3} m	Channel width
w_{rib}	1×10^{-3} m	Rib width
h_{ch}	1×10^{-3} m	Channel height
h_{GDL}	3×10^{-4} m	GDL thickness
δ_{CL}	15×10^{-6} m	CL thickness
δ_m	50×10^{-6} m	Membrane thickness
ε_{GDL}	0.7	GDL porosity
ε_{CL}	0.2	CL porosity
T, T_{ref}	343 and 298 K	Operatimg and reference temperatures
p, p_0	1.5 and 1 atm	Operating and reference pressures
$RH_{\{an,ca\}}$	1 and 1	Anode and cathode inlet relative humidity
$St_{\{an,ca\}}$	3 and 3	Anode and cathode flow stoichiometric ratios

Table 2: Parameters and their values used in the model

Parameter	Value	Description
K_{GDL}	3×10^{-12} m^2	GDL intrinsic permeability [15]
K_{CL}	3×10^{-14} m^2	CL intrinsic permeability [15]
K_{cond}	1 s^{-1}	Condensation coefficient [15]
K_{evap}	5×10^{-5} Pa^{-1}s^{-1}	Evaporation coefficient [15]
$\sigma_{GDL}^{\{th,in\}}$	500 and 5000 S m^{-1}	GDL through and in-plane electric conductivities [99]
σ_{CL}	500 S m^{-1}	CL electric conductivity [99]

$k_{GDL}^{\{th,in\}}$	1.7 and 21 W m^{-1} K^{-1}	GDL through and in-plane thermal conductivities [99]
k_{CL}	1 W m^{-1} K^{-1}	CL thermal conductivity [99]
k_{mem}	0.95 W m^{-1} K^{-1}	Membrane thermal conductivity [99]
Nu	2.98	Nusselt number for laminar flow in a rectangular channel with constant temperature at the channel perimeter
ρ_{mem}	1.98×10^{3} kg m^{-3}	Dry membrane density
EW	1.1×10^{3} kg mol^{-1}	Membrane equivalent weight
V_m	9×10^{-4} m^3 mol^{-1}	Membrane molar volume
$\alpha_{\{an,ca\}}$	0.7 and 0.7	Anodic and cathodic charge transfer coefficients
$i_{(an,ca)}^{ref,343K}$	2×10^{8} and 1×10^{4} A m^{-3}	Exchange current densities at 343 K [15]
$c_{\{H_2,O_2\}}^{ref}$	37.6 and 5.24 mol m^{-3}	H_2 and O_2 reference concentrations
$c_{SO_3}^{0}$	1.2×10^{3} mol m^{-3}	Concentration of sulfonic in the membrane
D_s^{ch}	1×10^{-3} m^2 s^{-1}	Channel capillary diffusivity [15]
$h_s^{GDL\text{-}ch}$	6.5×10^{-6} m s^{-1}	Mass transport coefficient for the liquid water transport
$J_{loss,0}$	20 A m^{-2}	Parasitic current density
R_{solid}	4×10^{-6} Ω m^2	Cell components electric resistance
r_{pell}	1×10^{-7} m	Catalyst pellet radius
δ^{Naf}	1×10^{-8} m	Ionomer (Nafion) thickness

2.1.1.1. 3D model equations

Table 3 shows the governing equations of conservation of mass, momentum, species, electronic charge, ionic charge, liquid water, dissolved water in the electrolyte (CLs and membrane), and energy.

Table 3: Governing equations

	Equation	Eq. #	Domains
Mass	$\nabla\cdot(\rho\mathbf{u})=S_{mass}$	(1)	Channels, GDLs, and CLs
Momentum	$\begin{cases}\rho\mathbf{u}\cdot\nabla\mathbf{u}=-\nabla p+\mu\nabla^2\mathbf{u} \\ \rho\mathbf{u}\cdot\nabla\mathbf{u}=-\nabla p+\mu\nabla^2\mathbf{u}-\dfrac{\mu}{K}\mathbf{u}\end{cases}$	(2)	Channels GDLs and CLs
Species	$\nabla\cdot\left(-\rho w_i\sum_j D_{ij}\nabla x_j\right)+\rho(\mathbf{u}\cdot\nabla)w_i=S_i$	(3)	Channels, GDLs, and CLs
Charge	$\begin{cases}\nabla\cdot(-\sigma_s\nabla\phi_s)=S_{\phi_s} \\ \nabla\cdot(-\sigma_m\nabla\phi_m)=S_{\phi_m}\end{cases}$	(4)	GDLs and CLs CLs and membrane
Liquid water	$\nabla\cdot(-\rho_l D_s\nabla s)+\nabla\cdot\left(\rho_l\dfrac{\mu_g}{\mu_l}\dfrac{K^l}{K^g}\mathbf{u}\right)=S_{liq}$	(5)	Cathode CL, GDL and channels
Dissolved water	$\nabla\cdot\left(-\dfrac{\rho_{mem}}{EW}D_{H_2O}^{Naf}\nabla\lambda\right)+\nabla\left(-\dfrac{n_d}{F}\sigma_l\nabla\phi_l\right)=S_\lambda$	(6)	CLs and membrane
Energy	$(\rho c_p)_{eff}\mathbf{u}\cdot\nabla T+\nabla\cdot(-k_{eff}\nabla T)=S_T$	(7)	All layers

The equations (1) and (2) represent the conservation of mass and momentum. Navier-Stokes equations are used to obtain the velocity field in the channels, and Brinkman equations, [101,102], are used in the porous mediums, GDLs and CLs.

Maxwell-Stefan equation, (3), is used to model transport of species by advection and diffusion in all layers except the membrane. Hydrogen, water vapor, and nitrogen are species used in the anode side; and oxygen, water vapor, and nitrogen are used at the cathode side. This equation can be applied to two species out of three to calculate their mass fractions and the value of the last one is determined by the conservation law:

$$\sum w_i = 1 \tag{8}$$

Binary diffusion coefficient of the species in the channels can be obtained from [104]:

$$D_{ij} = 3.16\times10^{-8}\left(\frac{T_0^{1.75}}{p_0\left(v_i^3+v_j^3\right)^2}\right)\left(\frac{1}{M_i}+\frac{1}{M_j}\right)^{1/2} \tag{9}$$

Bruggeman correction is used to determine diffusion coefficients of the species in the GDLs and CLs [105]:

$$D_{ij}^{\{\mathrm{GDL,CL}\}} = D_{ij}\varepsilon_{\{\mathrm{GDL,CL}\}}^{1.5} \tag{10}$$

Conservation of charge, equation (4), is used for the electrolyte, membrane and CLs, and the solid phase in CLs and GDLs.

Liquid saturation-based approximations are commonly used to model two-phase transport in irregular porous media consisting of hydrophilic and hydrophobic pores [4,114-116]. In this study, advection-diffusion of the liquid water saturation is modeled by equation (5) based on the form developed by Ye & Van Nguyen [15]. Conservation of liquid saturation is included in the cathode layers because of its effect on the gas transport and the cell performance due to flooding in the cathode CL and GDL due to water generation from the oxygen reduction reaction and the electro-osmotic drag from the anode side at high current densities [15,99,117-119]. Moreover, conservation equations for the liquid water can be applied to the anode side as well when necessary, for example when liquid water accumulates in the anode side due to hydrogen starvation during dead-ended anode (DEA) or anode bleeding (AB) operation modes, as considered for the models used in chapters 3 and 4 for the DEA and AB modes.

In the model, a constant capillary diffusivity, D_s, is used for the channel and in the GDL and CL it is given by [15]:

$$D_s = -\frac{K_l}{\mu_l}\frac{dp_c}{ds} \tag{11}$$

where, p_c is the capillary pressure which is a function of the water saturation and defined as the difference between the pressures of the two phases of the water [15]:

$$p_c = p_g - p_l \tag{12}$$

The experimental correlation suggested by Ye & Van Nguyen, [15], is used to determine the capillary pressure as a function of the water saturation in the cathode GDL and CL:

$$p_c = \left(e^{-a1(s-c)} - e^{a2(s-c)}\right)d + b \tag{13}$$

where *a1, a2, b, c,* and *d* are constants, given by [15]. Liquid and gas permeabilities in the GDL and CL are [15]:

$$\begin{aligned} K_{GDL}^{l} &= K_{GDL}s^{4.5} \quad , \quad K_{GDL}^{g} = K_{GDL}(1-s)^{4.5} \\ K_{CL}^{l} &= K_{CL}s^{3} \quad , \quad K_{CL}^{g} = K_{CL}(1-s)^{3} \end{aligned} \tag{14}$$

Based on the liquid water in the cathode GDL and CL following correction to the gas diffusion coefficient of the species is included [15]:

$$D_{i,s} = D_i \left(1-s\right)^2 \tag{15}$$

Water in the membrane enhances the ionic conductivity of the membrane. The excess water in the CLs and GDLs acts like a barrier against the reactants transport. Therefore, one of the important challenges in the PEM fuel cell is the water management which depends on the operation temperature, relative humidity (RH) of the reactant gases at the inlets, and the cell current density [120]. Transport of the dissolved water in the CLs and membrane is obtained from the conservation of the dissolved water, equation (6). The water diffusion coefficient in the electrolyte phase, $D_{H_2O}^{Naf}$, is given by [15]:

$$D_{H_2O}^{Naf} = \begin{cases} 3.1\times10^{-7}\lambda\left(e^{0.28\lambda}-1\right)e^{(-2436/T)} & 0<\lambda<3 \\ 4.17\times10^{-8}\lambda\left(161e^{-\lambda}+1\right)e^{(-2436/T)} & 3\le\lambda<17 \end{cases} \tag{16}$$

The electro-osmotic drag coefficient is given by [15]:

$$n_d = \frac{2.5}{22}\lambda \tag{17}$$

Thermal management is paramount in the operation of the PEM fuel cell due to the effect of the temperature distribution on the liquid water formation. In many studies, e.g. [99], authors claimed that the coupling between water and thermal management cannot be ignored in two-phase models. Temperature distribution in all layers is obtained from the energy conservation equation (7). Definitions of the parameters used in the energy conservation equation (7), are given in Table 4.

Table 4: Parameters of the energy conservation equation

Parameter	Definition
Effective thermal conductivity	$k_{eff} = \varepsilon k_f + (1-\varepsilon)k_s$
Fluid thermal conductivity	$k_f = sk_f^l + (1-s)k_f^g$
Gas mixture thermal conductivity [42]	$k_f^g = \sum_i \frac{x_i k_i}{\sum_j x_j \Phi_{ij}}$
Function Φ_{ij} [42]	$\Phi_{ij} = \frac{\left[1+\left(\frac{\mu_i}{\mu_j}\right)^{0.5}\left(\frac{M_j}{M_i}\right)^{0.25}\right]^2}{\left[8\left(1+\frac{M_i}{M_j}\right)\right]^{0.5}}$
Gas mixture viscosity [42]	$\mu = \sum_i \frac{x_i \mu_i}{\sum_j x_j \Phi_{ij}}$
Gas mixture specific heat capacity [42]	$c_p = \sum_i w_i c_{p,i}$

Source terms of the transport equations listed in Table 3 are depicted in Table 5. Mass and species source terms, equations (18) and (19), are the electrochemical reactions of the hydrogen and oxygen in the anode and cathode CLs, respectively, mass exchange of the water vapor with the dissolved water at the anode CL, and phase change of the water in the cathode channel, GDL, and CL, equation (23).

Table 5: Source terms for the governing equations

Source term	Eq. #	Unit
$S_{mass} = \begin{cases} -\frac{M_{H_2} i_{an}}{2F} - M_{H_2O} S_\lambda & \text{(anode CL)} \\ -\frac{M_{O_2} i_{ca}}{4F} - S_{phase} & \text{(cathode CL)} \\ -S_{phase} & \text{(cathode Ch and GDL)} \\ 0 & \text{(elsewhere)} \end{cases}$	(18)	kg m^{-3} s^{-1}
$S_i = \begin{cases} -\frac{M_{H_2} i_{an}}{2F} & (H_2, \text{ anode CL}) \\ -M_{H_2O} S_\lambda & (H_2O, \text{ anode CL}) \\ -\frac{M_{O_2} i_{ca}}{4F} & (O_2, \text{ cathode CL}) \\ -S_{phase} & (H_2O, \text{ cathode Ch, GDL, and CL}) \\ 0 & \text{(elsewhere)} \end{cases}$	(19)	kg m^{-3} s^{-1}
$S_{\phi_s} = \begin{cases} -i_{an} & \text{(anode CL)} \\ +i_{ca} & \text{(cathode CL)} \end{cases}$	(20)	A m^{-3}
$S_{\phi_m} = \begin{cases} +i_{an} & \text{(anode CL)} \\ -i_{ca} & \text{(cathode CL)} \end{cases}$	(21)	A m^{-3}
$S_{liq} = \begin{cases} S_{phase} + \left(\frac{i_{ca}}{2F} - S_\lambda \right) M_{H_2O} & \text{(cathode CL)} \\ S_{phase} & \text{(cathode Ch and GDL)} \end{cases}$	(22)	kg m^{-3} s^{-1}
$S_{phase} = \begin{cases} K_{cond} \Delta p \frac{\varepsilon_{GDL} (1-s) x_{H_2O} M_{H_2O}}{RT} & \Delta p = x_{H_2O} p - p_{sat} \geq 0 \\ K_{evap} \Delta p \varepsilon_{GDL} s \rho & \Delta p = x_{H_2O} p - p_{sat} < 0 \end{cases}$	(23)	kg m^{-3} s^{-1}
$S_\lambda = \begin{cases} \frac{k_{ads}}{\delta_{CL}} \frac{\rho_{mem}}{EW} \left(\lambda^{eq} - \lambda \right) & \text{(anode CL)} \\ \frac{k_{des}}{\delta_{CL}} \frac{\rho_{mem}}{EW} \left(\lambda^{eq} - \lambda \right) + \frac{i_{ca}}{2F} & \text{(cathode CL)} \end{cases}$	(24)	molm^{-3}s^{-1}

$$S_T = \begin{cases} i\left(\eta_{ca} + T\dfrac{dE}{dT}\right) + \sigma_m^{CL}\left(\nabla\phi_m\right)^2 + \sigma_s^{CL}\left(\nabla\phi_s\right)^2 + h_{fg}S_{liq} & \text{(cathode CL)} \\ i\eta_{an} + \sigma_m^{CL}\left(\nabla\phi_m\right)^2 + \sigma_s^{CL}\left(\nabla\phi_s\right)^2 & \text{(anode CL)} \\ \sigma_{GDL}^{th}\left(\nabla\phi_s\right)^2 + h_{fg}S_{liq} & \text{(cathode GDL)} \\ \sigma_{GDL}^{th}\left(\nabla\phi_s\right)^2 & \text{(anode GDL)} \\ \sigma_m^{mem}\left(\nabla\phi_m\right)^2 & \text{(membrane)} \end{cases} \quad (25) \quad \text{W m}^{-3}$$

The source term of the dissolved water at the CLs, given by (24), is proportional to the difference between the equilibrium and local levels of the membrane water content. The equilibrium membrane water content, λ^{eq}, is a function of the operation temperature and the water activity, a_w, and determined by the linear interpolation of the experimental data reported by Ge et al. [108] for the operation temperatures of 303 and 353 K.

The water activity is expressed by the following relationship, where the water saturation is only considered in the cathode side:

$$a_w = x_{H_2O}\frac{p}{p_{sat}} + 2s \tag{26}$$

Adsorption and desorption coefficients, k_{ads} and k_{des}, are given by [108]:

$$k_{ads} = 1.14\times10^{-5} f_v \exp\left[2416\left(\frac{1}{T_{ref}} - \frac{1}{T}\right)\right] \tag{27}$$

$$k_{des} = 4.59\times10^{-5} f_v \exp\left[2416\left(\frac{1}{T_{ref}} - \frac{1}{T}\right)\right] \tag{28}$$

where f_v is the volumetric ratio of the liquid water in the electrolyte:

$$f_V = \frac{\lambda V_{H_2O}}{V_{mem} + V_{H_2O}} \tag{29}$$

Four types of contributions to the source term of the energy conservation equation in (25) are considered: the reversible heat generation of the oxygen reduction reaction at the

cathode CL, the irreversible heat generation due to the activation overpotentials at the CLs; the ohmic losses in the GDLs, CLs, and membrane; and the latent heat generation of the water condensation in the cathode GDL and CL.

The source term of the conservation of the electronic and ionic charges are defined by the volume reaction rate at the anode and cathode CLs, equations (20) and (21). Anodic volume reaction rate is determined by the concentration-dependent Butler-Volmer equation:

$$i_{an} = i_{an}^{ref}\left[\frac{c_{H_2}}{c_{H_2}^{ref}}\exp\left(\frac{\alpha_{an}F\eta_{an}}{RT}\right) - \exp\left(\frac{-\alpha_{ca}F\eta_{an}}{RT}\right)\right] \tag{30}$$

Here, η_{an} is the activation overpotential which is defined as the difference between the potentials of the solid and electrolyte phases:

$$\eta_{an} = \phi_s - \phi_m \tag{31}$$

The reference current density is a function of the operation temperature and determined via Arrhenius-type relation [15]:

$$i_{an}^{ref} = i_{an}^{ref,343K}\exp\left[\frac{6.6\times10^4}{R}\left(\frac{1}{343} - \frac{1}{T}\right)\right] \tag{32}$$

Agglomerate model is used to determine the volume reaction rate in the cathode CL, [15]:

$$i_{ca} = 4F\frac{p_{O_2}}{H_{O_2}^{Naf}}\left(\frac{\delta^{Naf}}{a_{ratio}D_{O_2}^{Naf}} + \frac{\delta_{liq}}{a_{ratio}D_{O_2}^{liq}}\frac{H_{O_2}^{liq}}{H_{O_2}^{Naf}} + \frac{1}{\xi k_\eta}\right)^{-1} \tag{33}$$

Definitions of all parameters used in the above equation, (33), are summarized in Table 6.

Table 6: Parameters of the agglomerate model

Parameter	Definition
Effectiveness factor of the spherical agglomerate	$\xi = \frac{3\Phi \coth(3\Phi) - 1}{3\Phi^2}$
Thiele modulus of the spherical pellets, [111]	$\Phi = \frac{r_{pell}}{3}\sqrt{\frac{k_\eta}{D_{O_2}^{Naf}\left(1-\varepsilon_{CL}\right)}}$
Reaction rate constant	$k_\eta = \frac{i_{ca}^{ref}}{4Fc_{O_2}^{ref}}\exp\left(-\frac{\alpha_{ca}F}{RT}\eta_{ca}\right)$
Activation overpotential	$\eta_{ca} = \phi_s - \phi_m - \phi^{equil}$
Reference concentration of oxygen, [15]	$c_{O_2}^{ref} = \frac{p}{H_{O_2}^{Naf}}$
Henry's constant of oxygen in the Nafion, [112]	$H_{O_2}^{Naf} = 1.33\times10^5 \exp\left(\frac{-666}{T}\right)$
Henry's constant of oxygen in the liquid water, [112]	$H_{O_2}^{liq} = 5.08\times10^5 \exp\left(\frac{-498}{T}\right)$
Diffusivity of the dissolved oxygen in the Nafion, [112]	$D_{O_2}^{Naf} = 3.1\times10^{-7} \exp\left(\frac{-2768}{T}\right)$
Diffusivity of the dissolved oxygen in the liquid water, [112]	$D_{O_2}^{liq} = 1.98\times10^{-9}\frac{\mu_l(293)}{\mu_l(T)}\frac{T}{293}$
Thickness of the liquid water film around the catalyst pellet	$\delta_{liq} = s\frac{\varepsilon_{CL}}{a_{ratio}}$
Effective agglomerate surface area over the volume of the CL	$a_{ratio} = \frac{2\left(1-\varepsilon_{CL}\right)}{r_{pell}+\delta^{Naf}}$

2.1.1.2. P3D model

Mass, momentum, and species

Brinkman equations are solved over the anode and cathode channels and GDLs to obtain the flow distribution. Inside the channels, permeability is defined by the Hele-Shaw relation for a viscous flow between two parallel plates at a small distance [103]:

$$K_{ch} = \frac{h_{ch}^2}{12} \tag{34}$$

For the channels, mass source is defined based on the TP diffusive and convective fluxes between the channel and GDL. Diffusive flux of each species from the channel to the GDL is given by [25]:

$$N_{diff,i}^{ch-GDL} = D_i^{ch,GDL} \frac{2\left(\rho^{ch} w_i^{ch} - \rho^{GDL} w_i^{GDL}\right)}{\left(h_{ch} + h_{GDL}\right)} \tag{35}$$

where $D_i^{ch,GDL}$ is the equivalent mass diffusivity of species *i* that is defined by volumetric average of the channel and GDL diffusivities:

$$D_i^{ch,GDL} = \frac{h_{ch} D_i^{ch} + h_{GDL} D_i^{GDL}}{h_{ch} + h_{GDL}} \tag{36}$$

Diffusive flux of each species from the GDL to the channel is negative of the one from the channel to the GDL:

$$N_{diff,i}^{GDL-ch} = -N_{diff,i}^{ch-GDL} \tag{37}$$

To determine the convective flux of the species between the channel and GDL, a convective velocity in the TP direction is defined by Darcy's law based on the pressure difference between the channel and GDL [25]:

$$u_z^{ch-GDL} = \frac{K_{ch,GDL}}{\mu} \frac{2\left(p_{ch} - p_{GDL}\right)}{\left(h_{ch} + h_{GDL}\right)} \tag{38}$$

Here, $u_z^{ch\text{-}GDL}$ is the TP convective velocity from the channel to the GDL and $K_{ch,GDL}$ the cumulative permeability of the channel and GDL which is defined by the volumetric average of the channel and GDL permeabilities:

$$K_{ch,GDL} = \frac{h_{ch}K_{ch} + h_{GDL}K_{GDL}}{h_{ch} + h_{GDL}} \tag{39}$$

The convective fluxes are:

$$N_{conv,i} = \rho u_z^{ch-GDL} w_i \tag{40}$$

In addition to the diffusive and convective fluxes between the channels and GDLs, mass sources due to electrochemical reactions and water vapor mass exchange with the liquid water and dissolved water are defined based on the TP fluxes in the GDLs. The outward flux of hydrogen that takes part in the reaction at the anode catalyst layer is given by [106]:

$$N_{H_2}^{an} = -\frac{M_{H_2}}{2F}\left(J_{cell} + J_{loss}\right) \tag{41}$$

Here, J_{loss} is the parasitic current density due to the loss of hydrogen diffuses to the cathode side and defined as a function of the mole fraction of the hydrogen [106]:

$$J_{loss} = J_{loss,0} x_{H_2} \tag{42}$$

where $J_{loss,0}$ is a constant, given in Table 2, that is determined from the permeance of hydrogen through the membrane.

The outward flux of the oxygen takes part in the reaction at the cathode catalyst layer is determined by [106]:

$$N_{O_2}^{ca} = -\frac{M_{O_2}}{4F}\left(J_{cell} + J_{loss}\right) \tag{43}$$

Net water transport from the anode GDL to the membrane is given by:

$$N_{H_2O}^{an} = -k_{ads}\frac{\rho_{mem}}{EW}\left(\lambda_{an}^{eq} - \lambda_{an}\right)M_{H_2O} \tag{44}$$

Here, λ_{an} is the membrane water content at the membrane/anode interface and k_{ads} is given by (27). At the cathode side, however, water vapor exchanges mass with the liquid water

and liquid water interacts with the dissolved water. Therefore, water vapor flux at the cathode GDL is only due to phase change:

$$N_{H_2O}^{ca} = -S_{phase} h_{GDL} \tag{45}$$

Reaction rates of the species are defined based on the volumetric representation of TP fluxes as reactions:

$$S_i = \frac{N_i}{d_{eff}} \tag{46}$$

where d_{eff} is the effective depth of the medium:

$$d_{eff} = \frac{V_{Total}}{A_{active}} \Rightarrow \begin{cases} d_{eff,GDL} = \varepsilon h_{GDL} \\ d_{eff,ch} = h_{ch} \end{cases} \tag{47}$$

Here, V_{Total} is the total volume available to the species and A_{active} is the active area.

Electrochemical model

Anode electrode is chosen as the ground electrode and cathode electrode potential is the cell potential and obtained by subtraction of the activation overpotentails, η_{an} and η_{ca}, and ionic and ohmic potential drops, ΔV_m and ΔV_{ohm}, from the reversible cell potential, V_{rev}, as follows:

$$V_{cell} = V_{rev} - \eta_{an} - \eta_{ca} - \Delta V_m - \Delta V_{ohm} \tag{48}$$

The reversible cell potential is given by [109]:

$$V_{rev} = V_0 - \frac{RT}{2F} \ln \left[\frac{a_{H_2O}}{a_{H_2} \sqrt{a_{O_2}}} \right] \tag{49}$$

where a_i is the ratio of the pressure of species i to the operation pressure, and V_0 is the open-circuit potential:

$$V_0 = 1.23 - 0.00083 \times \left(T - T_{ref} \right) \tag{50}$$

Resistance of the electrolyte phase, membrane and CLs, against the proton transport (ionic current) leads to a potential drop which is a function of the electrolyte water content and the current density. Ionic conductivity of the membrane is approximated by a quadratic relation over the membrane based on its value at the middle of the membrane and at the membrane-anode and -cathode interfaces:

$$\sigma_m(z) = \underbrace{\frac{2\left(\sigma_m^{an} + \sigma_m^{ca}\right) - 4\sigma_m^{mem}}{\delta_m^2}}_{A} z^2 + \underbrace{\frac{4\sigma_m^{mem} - \sigma_m^{ca} - 3\sigma_m^{an}}{\delta_m}}_{B} z + \underset{C}{\sigma_m^{an}} \tag{51}$$

where, $\sigma_m(z)$ is the ionic conductivity of the membrane as a function of TP direction, and superscripts *mem*, *ca*, and *an* denote the corresponding values at the middle of the membrane, and at the cathode and anode interfaces, respectively. Ionic conductivity of the electrolyte is also a function of the water content and temperature [15]:

$$\sigma_m^{\{an,ca,mem\}} = \left(-0.326 + 0.514\lambda^{\{an,ca,mem\}}\right) \exp\left[1268\left(\frac{1}{303} - \frac{1}{T}\right)\right] \tag{52}$$

Thus, the ionic potential loss over the thickness of the membrane is obtained from:

$$\Delta V_{m,mem} = \int_0^{\delta_m} \frac{J_{cell}}{\sigma_m} dz = \frac{2J_{cell}}{\sqrt{4AC - B^2}} \tan^{-1}\left(\frac{\delta_m \sqrt{4AC - B^2}}{2C + B\delta_m}\right) \tag{53}$$

where the coefficients, *A*, *B* and *C* are the coefficients of the quadratic form of the ionic conductivity given by (51).

Ionic potential loss in the catalyst layers are obtained from the ionomer conductivity values in the anode and catalyst layers, $\sigma_{m,CL}^{an}$ and $\sigma_{m,CL}^{ca}$, which are taken the same as the membrane conductivity values at the anode and cathode interfaces respectively in this study. However, conductivity of the ionomer and the additional transport losses in the catalyst layers has drawn much attention in recent studies, and can be set to different values based on experimental measurements for fresh and aging catalyst layers [93,121-124].

Based on our observations form the 3D model and other models reported in literature [110], reaction rates in CLs, $i_{\{an,ca\}}$ given by equations (30) and (33), increase more than linearly with the distance from the GDL interface. Assuming a quadratic relation and integrating the reaction rate over the catalyst layer thickness to match the local current density, we obtain the potential loss over the CLs as follows:

$$\Delta V_{m,\mathrm{CLs}} = \frac{J_{cell}\delta_{CL}}{4}\left(\frac{1}{\sigma_{m,CL}^{an}} + \frac{1}{\sigma_{m,CL}^{ca}}\right) \tag{54}$$

As more comprehensive catalyst layer models are developed, this assumption can be modified to include properties such as Pt loading and effects of aging in catalyst layers. The total ionic loss is the sum of the ionic losses in the membrane and CLs:

$$\Delta V_m = \Delta V_{m,\mathrm{mem}} + \Delta V_{m,\mathrm{CLs}} \tag{55}$$

Ohmic loss due to the resistance of the solid components in the cell is given by:

$$\Delta V_{ohm} = R_{solid} J_{cell} \tag{56}$$

Here, R_{solid} is the total electric resistance of the cell components.

Anode activation overpotential is obtained from the concentration-dependent Butler-Volmer equation:

$$\eta_{an} = \frac{RT}{F\alpha_{an}} \ln\left(c_{H_2}^{ref}\left(\frac{J_{cell}}{i_{an}^{ref}\delta_{CL}} + \sqrt{\left(\frac{J_{cell}}{i_{an}^{ref}\delta_{CL}}\right)^2 + 4\frac{c_{H_2}^{CL}}{c_{H_2}^{ref}}}\right) \Big/ 2c_{H_2}^{CL}\right) \tag{57}$$

Here, $c_{H_2}^{CL}$ is the concentration of hydrogen in the catalyst layer which is defined based on its level in the GDL and transport resistances of the GDL and CL against its transport to the active sides of the CL to take part in the reaction [106]:

$$c_{H_2}^{CL} = c_{H_2}^{GDL} - \underbrace{\left(\frac{h_{GDL}\varepsilon_{GDL}}{D_{H_2O-H_2}^{GDL}} + \frac{0.5\delta_{CL}\varepsilon_{CL}}{D_{H_2O-H_2}^{CL}} \right)}_{R_{GDL}^{an}+R_{CL}^{an}} N_{H_2}^{an} \tag{58}$$

Current density is defined from the volume reaction rate in the cathode CL, by the agglomerate model, multiplied by the thickness of the CL:

$$J_{cell} = 4F \frac{p_{O_2}}{H_{O_2}^{Naf}} \left(\frac{\delta^{Naf}}{a_{ratio} D_{O_2}^{Naf}} + \frac{\delta_{liq}}{a_{ratio} D_{O_2}^{liq}} \frac{H_{O_2}^{liq}}{H_{O_2}^{Naf}} + \frac{1}{\xi k_\eta} \right)^{-1} \delta_{CL} \tag{59}$$

where p_{O_2} is the partial pressure of oxygen in the catalyst layer:

$$p_{O_2} = x_{O_2}^{CL} p_0 \tag{60}$$

Here, $x_{O_2}^{CL}$ is the mole fraction of oxygen in the catalyst layer which is defined based on its level in the GDL and transport resistances of the GDL and CL against its transport to the active sides of the CL to take part in the reaction [106]:

$$x_{O_2}^{CL} = x_{O_2}^{GDL} - \underbrace{\left(\frac{h_{GDL}\varepsilon_{GDL}}{D_{N_2-O_2}^{GDL}} + \frac{0.5\delta_{CL}\varepsilon_{CL}}{D_{N_2-O_2}^{CL}} \right)}_{R_{GDL}^{ca}+R_{CL}^{ca}} \frac{RT_0}{p_0} N_{O_2}^{ca} \tag{61}$$

Parameters used in the above equation are defined in Table 6. Substituting the current density obtained from the two-phase agglomerate model, equation (59), in the definitions of the potential losses and solving the equation (48), the cathode activation overpotential is calculated.

Liquid water transport

In the P3D model, the water saturation is defined only in the cathode side similarly to the 3D model. The source term of the conservation of the liquid water saturation, equation (5), defined in the cathode GDL as the sum of the liquid water sources from the phase change, water generation from the reduction reaction of oxygen, mass exchange with

the dissolved water in the membrane [15], and liquid water transport from the GDL to the channel:

$$S_{liq} = S_{phase} + \left(\frac{J_{cell}}{2Fh_{GDL}} - S_{\lambda} \right) M_{H_2O} + S_{liq}^{GDL-ch} \tag{62}$$

Here, $S_{liq}^{GDL\text{-}ch}$ is the source term used to add the transport of the liquid water from the GDL to the channel due to the difference between the level of the water saturations in the GDL and channel:

$$S_{liq}^{GDL-ch} = -\frac{\rho_l}{h_{GDL}} \left(\frac{\left(h_{ch} + h_{GDL}\right)}{2D_s^{GDL,ch}} + \frac{1}{h_s^{GDL-ch}} \right)^{-1} \left(s_{GDL} - s_{ch}\right) \tag{63}$$

where $D_s^{GDL,ch}$ is the equivalent capillary diffusivity of the GDL and channel which is determined from the volume average of the GDL and channel capillary diffusivities, D_s^{GDL} and D_s^{ch}, respectively:

$$D_s^{GDL,ch} = \frac{D_s^{GDL} h_{GDL} + D_s^{ch} h_{ch}}{h_{GDL} + h_{ch}} \tag{64}$$

The mass transport coefficient, $h_s^{GDL\text{-}ch}$, is used to correct the diffusion of the water saturation from the GDL to the channel.

The source term of the conservation of the liquid water saturation in the cathode channel is defined as the sum of the phase change and liquid water transport from the GDL to the channel, Eq. (63).

Membrane water transport

The source term of the conservation of the dissolved water, equation (6), in the anode and cathode sides are given by:

$$S_{\lambda}^{an} = \frac{k_{ads}}{h_{GDL}} \frac{\rho_{mem}}{EW} \left(\lambda_{an}^{eq} - \lambda_{an} \right) \tag{65}$$

$$S_{\lambda}^{ca} = \frac{k_{des}}{h_{GDL}} \frac{\rho_{mem}}{EW} \left(\lambda_{ca}^{eq} - \lambda_{ca} \right) + \frac{J_{cell}}{2Fh_{GDL}} \tag{66}$$

In order to obtain the through-plane distribution of water in the membrane, a 3-dof finite-difference formula is used: membrane/anode interface, λ_{an}, membrane/cathode interface, λ_{ca}, and at the middle of the membrane, λ_{mem}. Equality of the flux of the dissolved water that goes to or comes from the membrane to the flux from the source term at the anode and cathode GDLs and the continuity of the flux of the dissolved water through the membrane are used as three-constraint equations to obtain λ_{an}, λ_{ca} and λ_{mem}.

$$-\frac{\rho_{mem}}{EW} D_{H_2O}^{Naf,an} \frac{-3\lambda_{an} + 4\lambda_{mem} - \lambda_{ca}}{\delta_m} + \frac{2.5}{22} \lambda_{an} \frac{J_{cell}}{F} = S_{\lambda}^{an} h_{GDL} \tag{67}$$

$$-\frac{\rho_{mem}}{EW} D_{H_2O}^{Naf,\mathrm{ca}} \frac{3\lambda_{ca} - 4\lambda_{mem} + \lambda_{an}}{\delta_m} + \frac{2.5}{22} \lambda_{ca} \frac{J_{cell}}{F} = S_{\lambda}^{ca} h_{GDL} \tag{68}$$

$$\begin{aligned} &-\frac{\rho_{mem}}{EW} D_{H_2O}^{Naf,an} \frac{-3\lambda_{an} + 4\lambda_{mem} - \lambda_{ca}}{\delta_m} + \frac{2.5}{22} \lambda_{an} \frac{J_{cell}}{F} = \\ &-\frac{\rho_{mem}}{EW} D_{H_2O}^{Naf,\mathrm{ca}} \frac{3\lambda_{ca} - 4\lambda_{mem} + \lambda_{an}}{\delta_m} + \frac{2.5}{22} \lambda_{ca} \frac{J_{cell}}{F} \end{aligned} \tag{69}$$

Heat transfer

Temperature distribution over the channels and GDLs are obtained by solving energy conservation equation (7). The source terms for the energy equation in the cathode and anode GDLs are defined as:

$$S_T^{ca,GDL} = \frac{J_{cell}}{h_{GDL}} \left(\eta_{ca} + T \frac{dE}{dT} \right) + \frac{J_{cell}^2}{\sigma_m^{an}} + \frac{J_{cell}^2}{\sigma_{GDL}^{th}} + h_{fg} S_{liq} \tag{70}$$

$$S_T^{\mathrm{an},GDL} = \frac{J_{cell}}{h_{GDL}} \eta_{an} + \frac{J_{cell}^2}{\sigma_m^{ca}} + \frac{J_{cell}^2}{\sigma_{GDL}^{th}} \tag{71}$$

Temperature difference between the anode and cathode GDLs leads to the heat transfer through the CLs and membrane. Resistive relationship for the heat flux from the cathode GDL to the anode GDL is given by:

$$q_T''^{ca-an} = \left(\frac{\delta_m}{k_m} + 2\frac{\delta_{CL}}{k_{CL}} + \frac{h_{GDL}}{k_{GDL}^{th}} \right)^{-1} \left(T_{GDL}^{ca} - T_{GDL}^{an} \right) \tag{72}$$

Heat fluxes from the GDL to the ribs and channel are:

$$q_T''^{GDL-rib} = \frac{2k_{GDL}^{th}}{h_{GDL}} \left(T_{GDL} - T_0 \right) \tag{73}$$

$$q_T''^{GDL-ch} = \left(\frac{h_{GDL}}{2k_{GDL}^{th}} + \frac{1}{h_{ch}} \right)^{-1} \left(T_{GDL} - T_{ch} \right) \tag{74}$$

Heat transfer through the graphite plate is not considered because of the high thermal conductivity of the graphite plate. Moreover, the temperature at the rib/GDL interface is the same as the operation temperature. In equation (74), h_{ch} is the convective heat transfer coefficient in the channel:

$$h_{ch} = Nu \frac{K_{eff,ch}}{D_h} \tag{75}$$

where Nu is the Nusselt number and D_h the hydraulic diameter of the channel.

Through-plane heat fluxes in the channel are the heat flux from the GDL to the channel due to the temperature difference between them, as given by (74), and the heat flux to the upper wall of the channel:

$$q_T''^{ch-wall} = h_{ch} \left(T_{ch} - T_0 \right) \tag{76}$$

2.1.2. Boundary conditions

Following set of the boundary conditions are used for the 3D and P3D models.

At the inlets, a constant velocity based on the stoichiometric ratio at the reference current density, here $10^4 A/m^2$, is specified:

$$u_{in}^{an} = St_{an} \frac{10^4}{2F} A_{active} \frac{RT_0}{p_0} \frac{1}{h_{ch} w_{ch}} \tag{77}$$

$$u_{in}^{ca} = St_{ca} \frac{10^4}{4F} A_{active} \frac{RT_0}{p_0} \frac{1}{h_{ch} w_{ch}} \frac{1}{0.21} \tag{78}$$

The cathode inlet velocity is divided by 0.21 which is the molar ratio of oxygen in dry air. Mass fractions of the species at the inlets are defined based on the relative humidity of the reactants at the inlets:

$$w_{H_2O,an}^{in} = \frac{M_{H_2O}}{M_{an}^{in}} RH_{an} \frac{p_{sat}}{p_0}, w_{H_2,an}^{in} = \frac{M_{H_2}}{M_{an}^{in}} \left(1 - RH_{an} \frac{p_{sat}}{p_0} \right) \tag{79}$$

$$w_{H_2O,\mathrm{ca}}^{in} = \frac{M_{H_2O}}{M_{ca}^{in}} RH_{ca} \frac{p_{sat}}{p_0}, w_{O_2,\mathrm{ca}}^{in} = \frac{M_{O_2}}{M_{ca}^{in}} \left(1 - RH_{ca} \frac{p_{sat}}{p_0} \right) 0.21 \tag{80}$$

Here, M^{in} is the molar mass of the species at the inlets. Moreover, the inlet temperature is set to the operation temperature.

At the outlets, outflow boundary condition is used for all species, liquid water, and temperature:

$$-\mathbf{n} \cdot \rho D_{ij} \nabla w_i = 0 \quad , \quad -\mathbf{n} \cdot D_s \nabla s = 0 \quad , \quad -\mathbf{n} \cdot q'' = 0 \tag{81}$$

where **n** is the normal vector to the outlet boundary. In addition, the outlet pressure is set to the operation pressure.

No-slip boundary condition is used at the walls of the modeling domain. Ground and cell potentials are set to the outer walls of the anode and cathode GDLs, respectively, for the 3D model.

2.1.3. Numerical approach

Brinkman, Maxwell-Stefan, Butler-Volmer, liquid water, dissolved water, and conservation of energy equations are coupled and solved numerically by the commercial finite element package, COMSOL Multiphysics. The unknowns of the 3D model are: the velocity and pressure at the anode and cathode sides; hydrogen and water vapor mole fractions at the anode side and oxygen and water vapor mole fractions at the cathode side; electrolyte and electric potentials; liquid water saturation at the cathode side; membrane water content at the membrane and CLs; and the temperature in all layers; total of 13 variables. The unknowns of the P3D model are: the velocity and pressure in the anode and cathode channels and GDLs; hydrogen and water vapor mole fractions at the anode channel and GDL and oxygen and water vapor mole fractions at the cathode channel and GDL; current density and cathode activation overpotential; liquid water saturation in the cathode GDL and channel; membrane water content at the anode and cathode/membrane interfaces and the middle of membrane; and the temperature in the channels and GDLs; total of 27 variables.

A structural mesh with the grid system of $10 \times 30 \times 26$ ($x \times y \times z$) with uniform grid in y direction and non-uniform grid in x and z directions is used for the 3D model, as shown in Fig. 2a. Number of elements and number of degree of freedom (DOF) are about 6.2 K and 71.2 K, respectively, for the 3D model. Quadrangular linear elements over the channel and ribs with 2 layers boundary layer at the channel/rib interface is used for the cell section used in the numerical study for the P3D, as shown in Fig. 2b. For the P3D model, number of elements and DOF are 450 and about 12 K, respectively. Fully-coupled solver with Newton iterations and direct PARDISO (parallel sparse direct solver) is used to solve the linear system of equations. Table 7 shows the comparison of the P3D and 3D models in terms of DOF, CPU time, and the required RAM (random access memory). It is concluded that the P3D model is about 40 times faster than the 3D model. Typically, the CPU time increases with the square of the DOF in addition to the increasing bandwidth of the sparse system due to increases connection between the nodes.

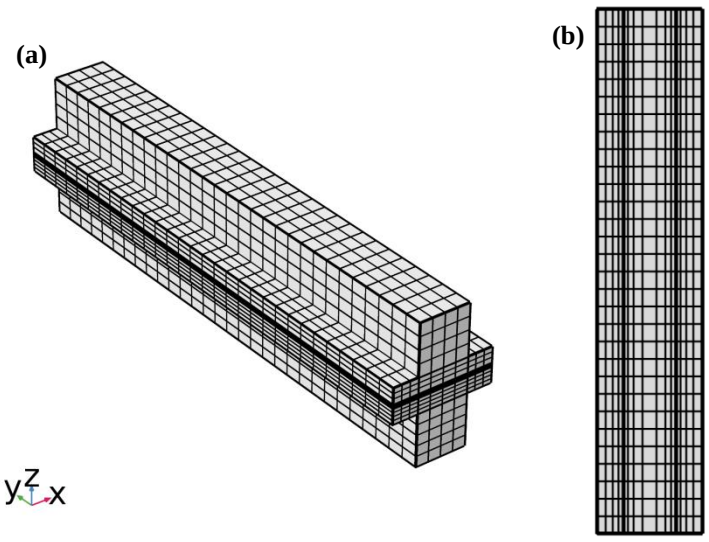

Figure 2: Mesh distribution for: a) 3D model; b) P3D model

Table 7: Comparison of the computational costs of the P3D and 3D models

Study	DOF	CPU time	RAM
P3D	12.27 K	1 min 6 s	3.05 GB
3D	71.2 K	41 min 19 s	4.85 GB

2.2. Results

2.2.1. Polarization curves

Agreement between the polarization curves from the P3D and 3D models is remarkable, as demonstrated in Fig. 3a, for the base operation parameters and model parameters listed in Tables 1 and 2. In order to assess the accuracy of the P3D model further, sensitivity analysis is carried out with respect to variations of the channel height, GDL thickness, widths of the channels and ribs, operation temperature, and relative

humidity (RH) of the reactant gases at the inlets with the three-dimensional model, as illustrated in Fig. 3. The P3D model predicts the 3D model polarization curves very well at low current densities ($< 10^4$ A/m^2) and deviates slightly at higher current densities because of higher consumption of species that leads to higher gradient of species in the land-channel area.

Figure 3b shows the effect of the channel height on the cell performance. Agreement is better for thinner channels which is consistent with the Brinkman approximation for the flow of a viscous fluid between two parallel plates separated by a small distance. Thickness of the GDL is an important parameter that affects the cell performance. Utilizing a thicker GDL results in a lower cell performance, Fig. 3c, because of the higher resistance against the transport of the reactants from channels to CLs, more liquid accumulation in the GDLs, and higher electrical resistance in the TP direction [125]. Moreover, a wider channel results in a better cell performance since reactants diffuse easily to the CL from the channels [126], as demonstrated in Fig. 3d. A deviation between the 3D and P3D polarization curves at high current densities is seen for narrower channel which shows the limit of the P3D model in following cross-sectional diffusion of the species, especially oxygen, under the rib in the GDL of the 3D model. However, a very good agreement between the polarization curves is seen for the designs with the same width for the channel and rib and wider channel which are common choices for practical designs.

Membrane must be hydrated well to enhance its ionic conductivity, reduce its resistance against the transport of the protons, and enhance the cell performance. Water from the reduction of oxygen at the cathode CL is not enough to hydrate the membrane. Therefore, humidification of the reactant gases at the inlets is necessary. The operation temperature of the cell is also important due to its effect on the ionic conductivity of the membrane, reaction kinetics, and the saturation pressure. The cell performance is enhanced with the increase in the operation temperature and the inlet relative humidity because of the higher membrane ionic conductivity and the electrode kinetics [127], as shown in Figs. 3e and 3f.

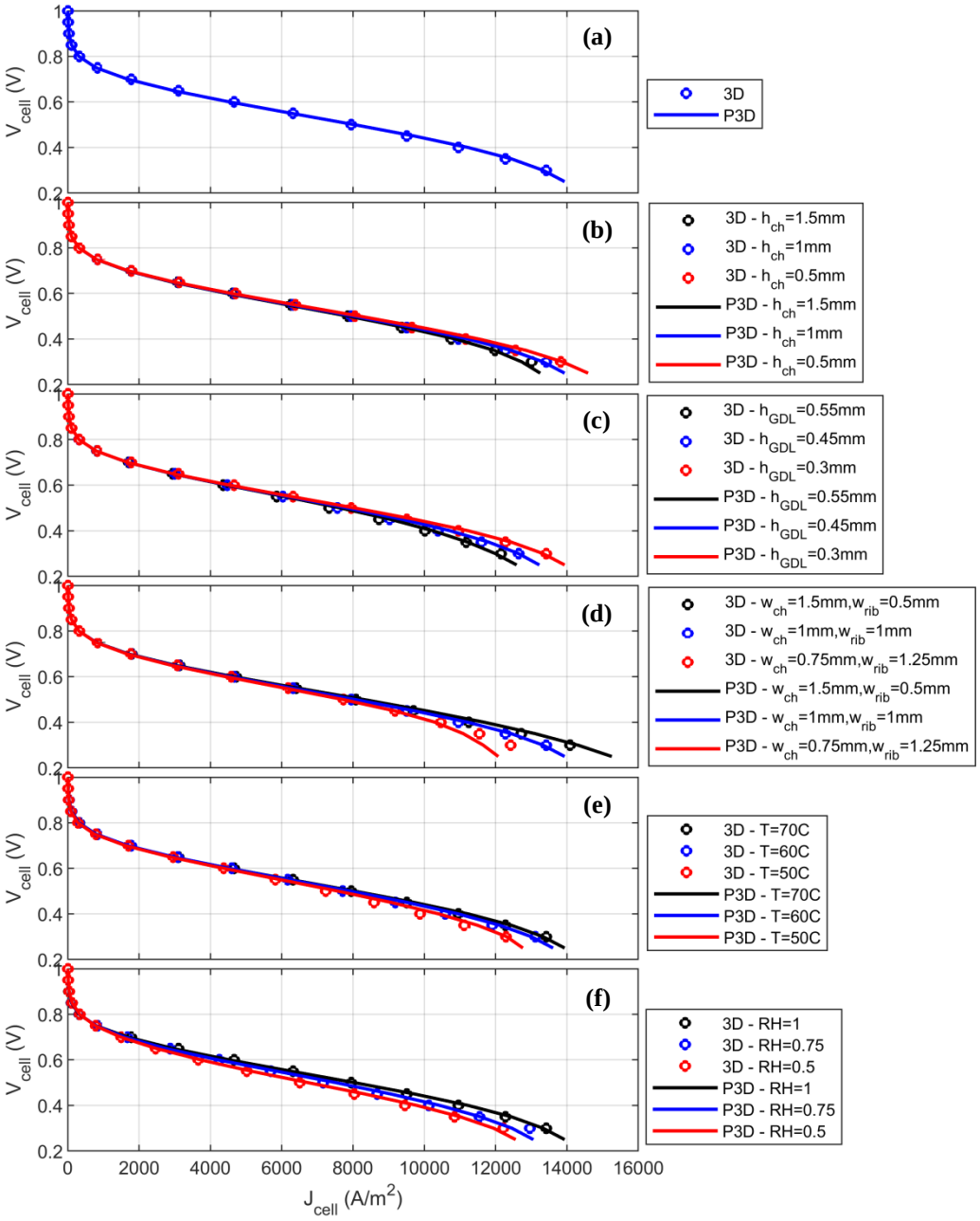

Figure 3: Comparison of the polarization curves of the 3D and P3D models for: a) base operation and model parameters; and the variations of: b) height of the channel, c) thickness of the GDL, d) widths of the cahnnels and ribs, e) operation temperature, f) relative humidity of the reactant gases at the inlets $RH_{an}=RH_{ca}=RH$

2.2.2. Distribution of species

Distributions of species, water saturation, temperature, and the dissolved water in the membrane are compared for the P3D and 3D models at a high current density, $J_{cell} = 1.1\times10^{4}\text{A/m}^2$, in Figs. 4 and 5. Distributions labeled with (a), (b), (c), and (d) are from the 3D model; and (e), (f), (g), and (h) are from the P3D model. For the 3D model, distributions of the species, water saturation, and temperatures are averaged in the **z**-direction in the GDL.

Figures 4a and 4e show the water saturation in the cathode GDL from the 3D and P3D models, respectively. More liquid water accumulates under the ribs than the channels due to increased resistance to transport in the porous GDLs. Comparison of the Figs. 4a and 4e shows a good agreement between the liquid water saturation levels in the P3D and 3D models.

Thermal management is another important issue that affects the cell performance by altering the saturation pressure of the liquid water, ionic conductivity of the membrane, and reaction kinetics. Figures 4f and 4g show the temperature distribution in the cathode and anode GDLs, respectively. Higher temperature is observed under the channel than under the rib due to the higher conductivity of the ribs than the gas mixture in the channel. Similar results are obtained in the literature as well, for example, Lee et al. [128] measured the temperature distribution in the through-plane direction of a PEMFC by inserting 7 micro-thermocouples between the layers of the cell. Authors report that temperature at the GDL/CL interface is about 2 K higher than the operation temperature which is consistent with the temperature levels in the GDLs for the 3D and P3D models, as shown in Figs. 4b, 4c, 4f, and 4g.

Membrane water content plays an important role on the cell performance. Membrane has to be well-hydrated to ensure high ionic conductivity. However, excess water in the CLs and GDLs acts as a barrier against the transport of gas species and reactants. Figures 4d and 4h show the dissolved water distribution at the mid-plane of the membrane for 3D and P3D models, respectively. Both models predict higher dissolved

water under the ribs and towards the end of the channel. However, P3D model slightly overpredicts the membrane water content under the ribs.

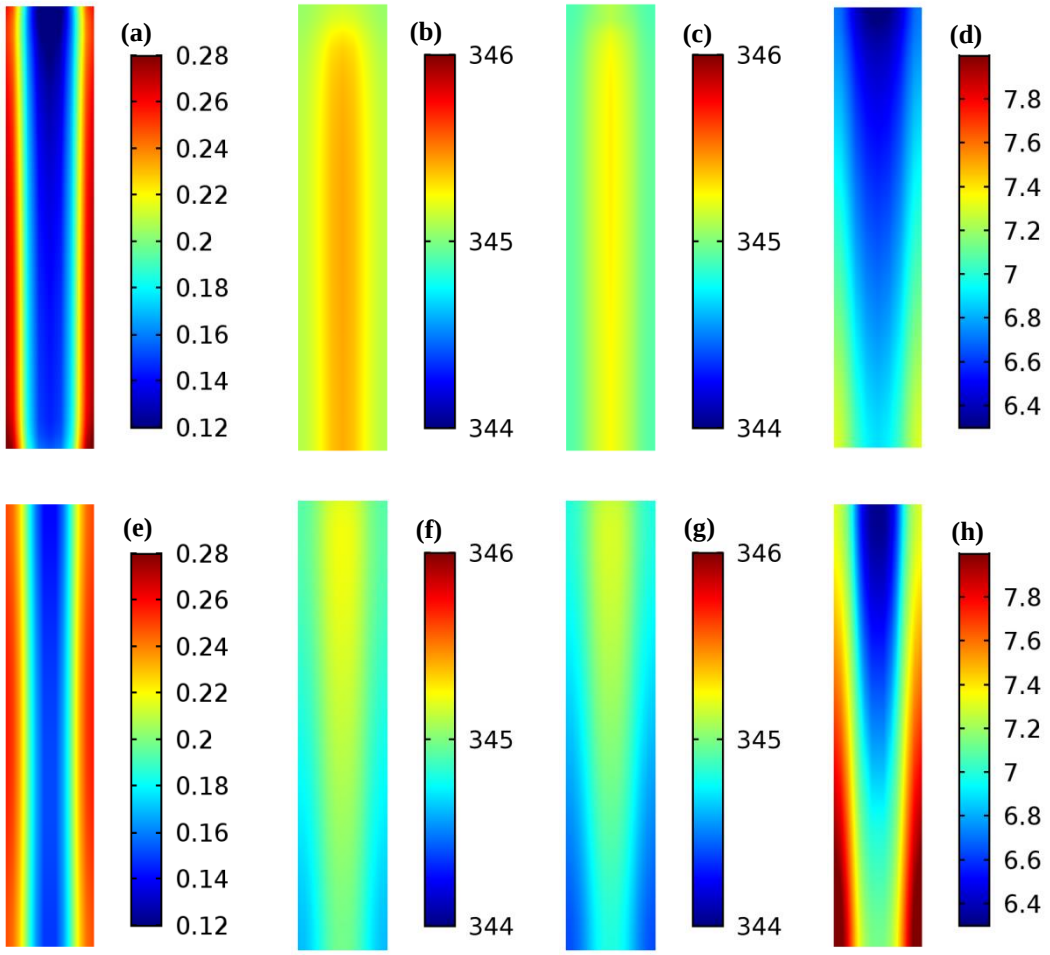

Figure 4: Comparison of the distributions of the liquid water saturation, (a) and (e), cathode temperature, (b) and (f), and anode temperature, (c) and (g), in the GDLs; and dissolved water in the membrane, (d) and (h), at $J_{cell}=1.1\times10^{4}A/m^{2}$; (a), (b), (c), and (d) are from the 3D model; and (e), (f), (g), and (h) are from the P3D model

Distributions of gas species at the anode and cathode sides are important for the design of the flow fields for which an accurate P3D model can be effective. Figure 5 shows the comparisons of species distributions in the GDLs, namely hydrogen and water vapor at the anode GDL and oxygen and water vapor at the cathode GDL. A good agreement is observed between the results of the P3D and 3D models.

Both models predict almost a uniform hydrogen and water vapor distributions at the anode GDL, in Figs. 5a, 5b, 5e and 5f. For the cathode GDL, P3D model predicts the oxygen level at the inlet and its depletion at the bottom of the GDL very well, Figs. 5g and 5c. Moreover, comparison of the Figs. 5h and 5d show that P3D model captures the water vapor distribution in the cathode GDL, but slightly underestimates towards the end of the cell.

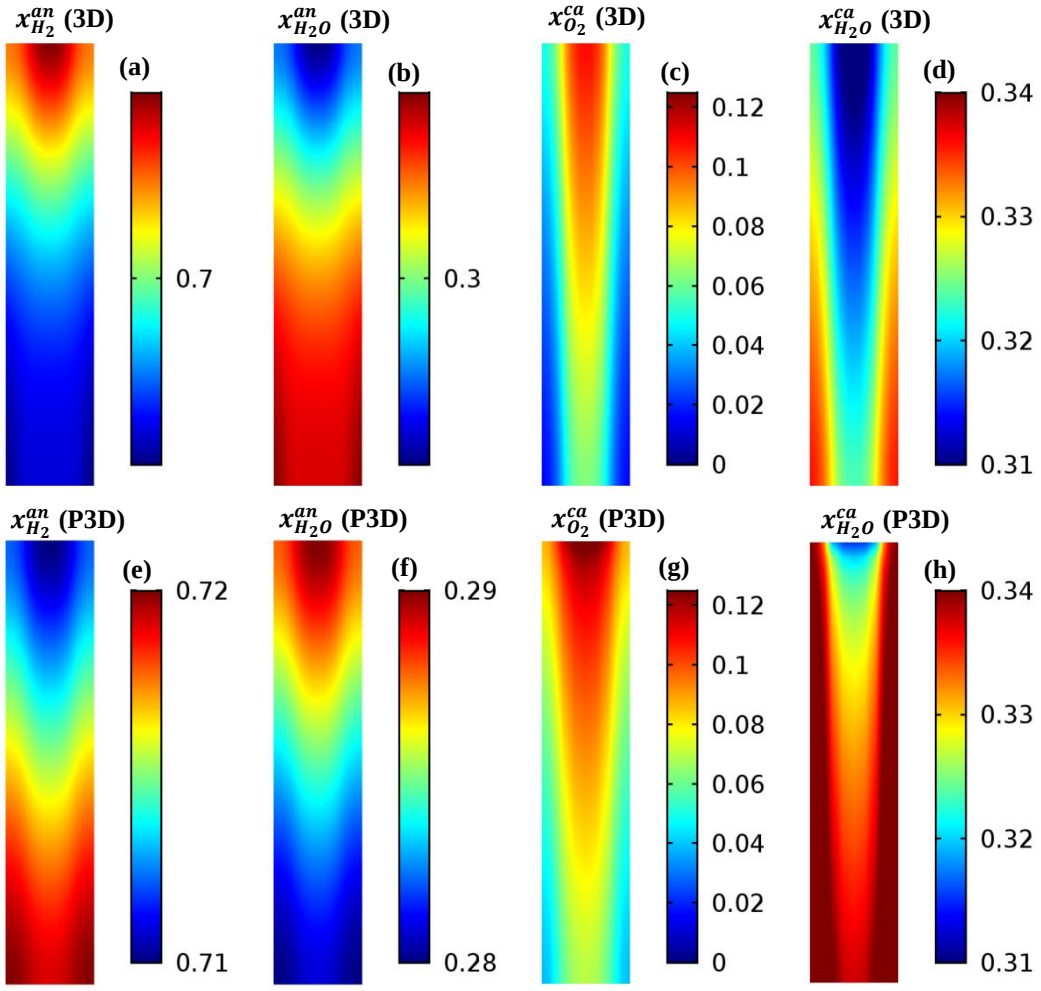

Figure 5: Comparison of the distribution of the hydrogen, (a) and (e), anode water vapor, (b) and (f), oxygen, (c) and (g), and cathode water vapor in the GDL, (d) and (h), at $J_{cell}=1.1\times10^4 A/m^2$; (a), (b), (c), and (d) are from the 3D model; and (e), (f), (g), and (h) are from the P3D model

In addition to comparisons of in-plane distributions, in Figs. 4 and 5, comparisons along the channel at the channel and rib centerlines (sections A-A and B-B, respectively, in Fig. 6a) for the average cell current density of 1700, 6300, and 11200 A/m^2 are also presented. Anode side species, hydrogen and water vapor, are already uniform and change very little. But, significant variations are observed for the cathode side species.

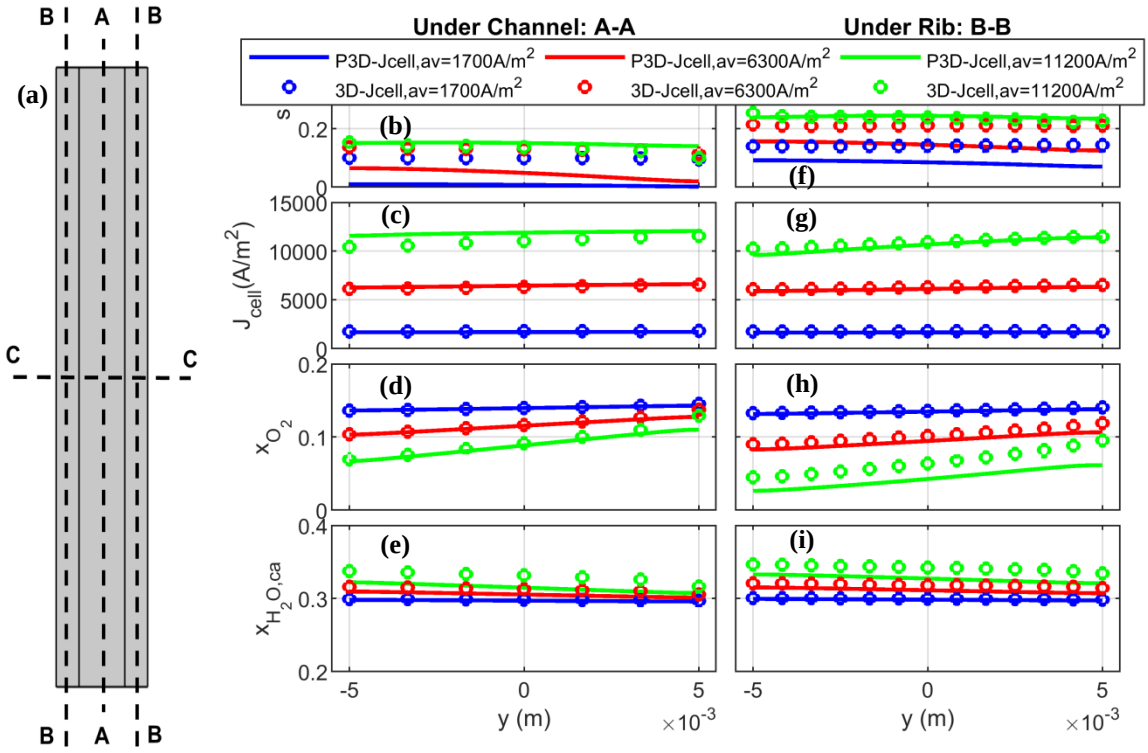

Figure 6: (a) Schematic of the channel with the sections along the channel and at the channel centerline (A-A) and at the ribs centerlines (B-B), and across the channel at the middle of the channel (C-C); comparisons of the distributions of the liquid water saturation, current density, oxygen and water vapor mole fractions at the middle of the GDL and along A-A: (b), (c), (d), and (e), respectively, and along B-B: (f), (g), (h), and (i), respectively; for the average current density of 1700, 6300, and 11200 A/m^2

Agreement is excellent between the P3D and 3D models at the channel and rib centerlines, sections A-A and B-B, for the current density, oxygen and water vapor mole fractions at low and medium average current densities, 1700 and 6300 A/m^2, and a slight

deviation is observed for the high current density, 11200 A/m^2, as demonstrated in Figs. 6c, 6d, 6e, 6g, 6h, and 6i. Moreover, P3D model under-predicts the liquid water saturation at low average current densities, Figs. 6b and 6f, but agrees very well with the 3D model at high current density where the effect of liquid water on the transport of reactants at the cathode-side is more prominent.

Figure 7 shows the comparisons of the distributions of the oxygen and water vapor mole fractions, current density, and liquid water saturation across the channel, section C-C in Fig. 6a, for the average cell current density of 1700, 6300, and 11200 A/m^2.

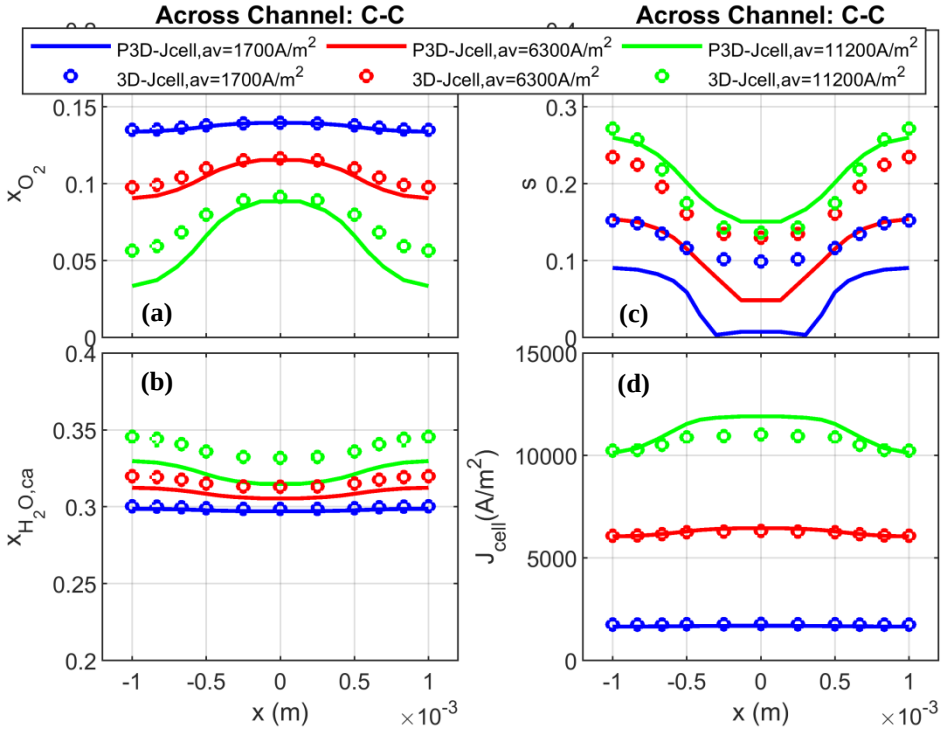

Figure 7: Comparisons of the distributions of the oxygen, water vapor, water saturation, and current density at the middle of the GDL and across the channel, section C-C: (a), (b), (c), and (d), respectively; for the average current density of 1700, 6300, and 11200 A/m^2

A very good agreement is seen for oxygen, water vapor, and current density for the low and medium average cell current densities, 1700 and 6300 A/m^2, and a slight deviation is observed for high current density, 11200 A/m^2, as demonstrated in Figs. 7a, 7b, and 7d.

Moreover, the P3D model predicts the liquid water saturation behavior across the channel and for the current density variation, as demonstrated in Fig. 7c. Nevertheless, the agreement is very good for the higher current density, 11200 A/m^2.

Figure 8 shows the distributions of the liquid water saturation, oxygen mole fraction, and temperature at the middle of the channel cross section at the cell current densities of 6300 and 11200 A/m^2. One can see that the distributions in the channels and GDLs do not change much in the TP direction which is consistent with the assumption of linear and low deviation of the model variables used to develop the P3D model for the average value of the model variables at the middle of the channels and GDLs. Moreover, it can be seen that the IP distribution of the model variables do not change in the TP direction in the CLs which means that the IP distribution in the CLs can be neglected and its resistance against transport of model variables in the TP direction is enough to model the CLs in the P3D model. Furthermore, Figs. 8a and 8b show that the water saturation in the cathode channel is zero, which means that the liquid water is discharged from the channel by convective velocity as soon as it gets to the channel. This is consistent with neglecting water saturation in the cathode channel to reduce the P3D model runtime.

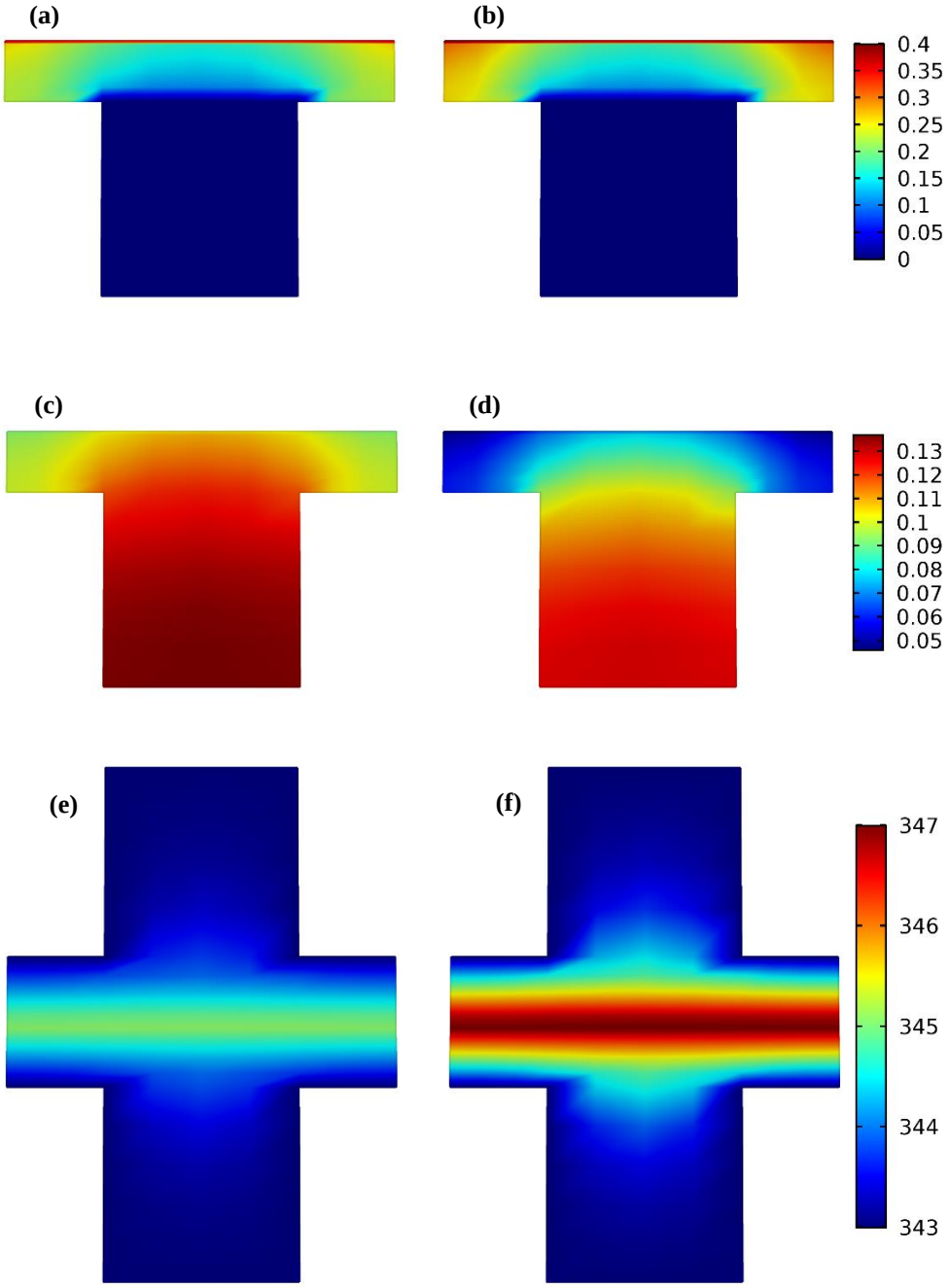

Figure 8: Distributions of: (a) and (b) liquid water saturation, (c) and (d) oxygen mole fraction, and (e) and (f) tempresture of the 3D model in the channel cross section at the middle of the channel; (a), (c), and (e) are for the cell curretn density of 6300 A/m^2; (b), (d), and (f) are for the cell curretn density of 11200 A/m^2; anode and cathode sides are at the top and bottom, respectively

Chapter 3

EFFECTS OF FLOW-FIELD DESIGN AND OPERATING CONDITIONS ON THE PERFORMANCE OF AN ANODE-BLEEDING PEM FUEL CELL

Durability and cost are the main barriers against the commercialization of the proton exchange membrane fuel cell. High hydrogen utilization and stable transient cell voltage are sustained under the anode bleeding operation mode with an ultra-low flow at the anode exit. In this chapter, the pseudo-three-dimensional (P3D) model developed in chapter 2 is improved to a transient model with carbon corrosion to study the cell performance during anode bleeding operation mode. The model is validated against the experimental data by comparing the polarization curves and cell voltage transients during the dead-ended anode operation. The model is used to attain an optimum bleeding rate, which results in a stable transient operation of the cell without carbon corrosion while hydrogen utilization is kept at more than 99%. Moreover, the effects of the operating conditions on cell performance during the anode bleeding operation mode are investigated. Results demonstrate that higher anode pressure, lower relative humidity at the cathode inlet, lower cell temperature, and higher stoichiometric flow for the cathode improves the cell performance. Lastly, performance of the cells with serpentine, straight, and interdigitated channels for the anode flow field and serpentine channels for the cathode flow field under the anode bleeding operation mode are investigated. It is found that the cell with the serpentine channels for both anode and cathode flow fields offers the best performance.

3.1. Methodology

The transient P3D model is applied to the cells with active areas of 8.17, 8.9, and 25 cm^2. Straight and serpentine channels are used for the anode and cathode flow fields, respectively, for the 8.9-cm^2 cell, and serpentine channels are used for both anode and cathode flow fields for other cells. Anode and cathode flow fields are projected on a single surface to form the computational domain, as demonstrated in Fig. 9c for the 8.9-cm^2 cell.

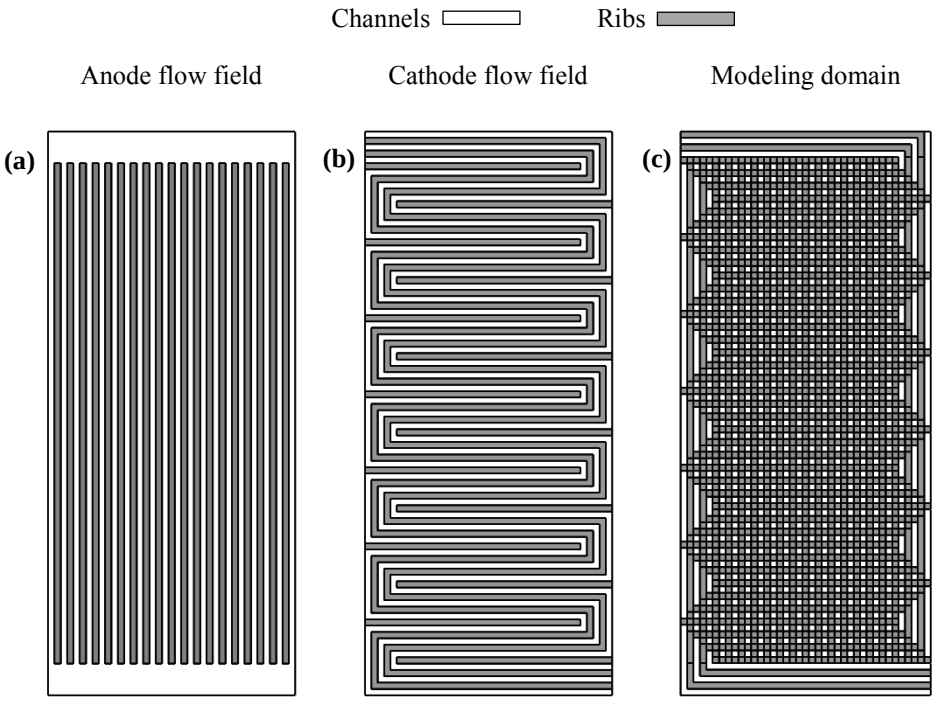

Figure 9: Flow fields (channels and ribs): (a) anode, (b) cathode, (c) anode and cathode on a single surface that forms computational domain for the cell with active area of 8.9 cm^2

3.1.1. Governing equations

Two-dimensional Brinkman and Maxwell-Stefan equations are used to obtain the flow field and species transport, respectively, in the channels and GDLs. Electrochemical reaction rates of the anode HOR and ORR and cathode CCR are calculated from the Butler-

Volmer equations, and the cathode ORR rate is obtained from the agglomerate model. Moreover, the transport of liquid water saturation in the cathode and anode GDLs and anode channel, dissolved water in the electrolyte phase, and the temperature are included in the model. Basic geometric, operation, and model parameters that are common for all cells are listed in Table 8, and Table 9 contains the parameters that are not common for all cells.

Table 8: Basic geometric, operation, and model parameters

Parameter	Value	Description
h_{ch}	1×10^{-3} m	Channel height
h_{GDL}	3×10^{-4} m	GDL thickness
δ_{CL}	15×10^{-6} m	CL thickness
δ_m	25×10^{-6} m	Membrane thickness
ε_{GDL}	0.76	GDL porosity [97]
ε_{CL}	0.2	CL porosity [15]
T_{ref}	298 K	Reference temperature
p_0, p_{ref}	1.5 and 1 atm	Operating and reference pressures
$RH_{\{an,ca\}}$	1 and 1	Inlet relative humidity of the anode and cathode
K_{GDL}	5.09×10^{-12} m^2	GDL intrinsic permeability [98]
K_{cond}	1 s^{-1}	Condensation coefficient [15]
K_{evap}	5×10^{-5} Pa^{-1}s^{-1}	Evaporation coefficient [15]
$\sigma_{GDL}^{\{th,in\}}$	500 and 5000 S m^{-1}	GDL through and in-plane electrical conductivities [99]
σ_{CL}	500 S m^{-1}	CL electrical conductivity [99]
$k_{GDL}^{\{th,in\}}$	1.7 and 21 W m^{-1} K^{-1}	GDL through and in-plane thermal conductivities [99]
k_{CL}	1 W m^{-1} K^{-1}	CL thermal conductivity [99]
k_{mem}	0.95 W m^{-1} K^{-1}	Membrane thermal conductivity [99]
Nu	2.98	Nusselt number for laminar flow in a rectangular channel with constant temperature at the channel perimeter
ρ_{mem}	1.98×10^3 kg m^{-3}	Dry membrane density
EW	1.1×10^3 kg	Membrane equivalent weight

	mol^{-1}	
V_m	9×10^{-4} m^3 mol^{-1}	Membrane molar volume
α_C	0.275	Charge transfer coefficient of CCR [85]
$J_{HOR}^{ref,343K}$	2.82×10^{3} A m^{-2}	Reference current density of HOR at 343 K [15]
$J_{ORR}^{ref,343K}$	0.1065 A m^{-2}	Reference current density of ORR at 343 K [15]
J_{CCR}^{ref}	2.5×10^{-5} A m^{-2}	Reference current density of CCR [85]
$V_{H_2}^{eq}$	0 V	Equilibrium potential of HOR [73]
$V_{O_2}^{eq}$	1.196 V	Equilibrium potential of ORR [85]
V_C^{eq}	0.207 V	Equilibrium potential of CCR [85]
V_θ	1 V	Reference potential of Langmuir isotherm [85]
$m_{C,0}$	2×10^{-3} g cm^{-2}	Initial loading of carbon per unit area [92]
$c_{\{H_2,O_2\}}^{ref}$	56.4 and 3.39 mol m^{-3}	Reference concentrations of H_2 and O_2 [11,100]
$c_{SO_3}^{0}$	1.2×10^{3} mol m^{-3}	Concentration of sulfonic in the membrane
D_s^{ch}	1×10^{-3} m^2 s^{-1}	Capillary diffusivity of the channel [15]
$J_{loss,0}$	10 A m^{-2}	Parasitic current density
R_{solid}	1.25×10^{-5} Ω m^2	Electric resistance of the cell components
r_{pell}	1×10^{-7} m	Radius of the catalyst pellet [15]
δ^{Naf}	1×10^{-8} m	Thickness of the Nafion film around the catalyst pellet [15]
σ	0.0625 N m^{-1}	Surface tension of water
θ_{CL}	60°	Contact angle of the CL

Table 9: Geometric, operation, and model parameters for the cells with active areas of 8.17, 8.9, and 25 cm^2

Parameter	8.17 cm^2	8.9 cm^2	25 cm^2
Channel width (w_{ch})	1×10^{-3} m	0.5×10^{-3} m	0.7×10^{-3} m
Rib width (w_{rib})	1×10^{-3} m	0.5×10^{-3} m	1×10^{-3} m
Operating temperature (T_0)	328 K	343 K	328 K

Anode inlet stoichiometric ratio (St_{an})	3.5	2.5	1.5
Cathode inlet stoichiometric ratio (St_{ca})	6	4	2.5
Charge transfer coefficient of HOR (α_{H_2})	0.5	0.5	0.85
Charge transfer coefficient of ORR (α_{O_2})	0.825	0.81	0.85
Mass transport coefficient for liquid water transport ($h_s^{GDL\text{-}ch}$)	1.625×10^{-6} m s^{-1}	5.5×10^{-6} m s^{-1}	3.225×10^{-6} m s^{-1}

Changes made to the steady P3D model developed in chapter 2 are as follows. Time-dependent governing equations are summarized in Table 10.

Table 10: Governing equations

	Equation	Eq. #
Mass	$\frac{\partial(\varepsilon\rho)}{\partial t}+\nabla\cdot(\rho\mathbf{u})=S_{mass}$	(82)
Momentum	$\rho\frac{\partial\mathbf{u}}{\partial t}+\rho\mathbf{u}\cdot\nabla\mathbf{u}=-\nabla p+\mu\nabla^2\mathbf{u}-\frac{\mu}{K}\mathbf{u}$	(83)
Species	$\varepsilon\rho\frac{\partial w_i}{\partial t}+\nabla\cdot\left(-\rho w_i\sum_j D_{ij}\nabla x_j\right)+\rho(\mathbf{u}\cdot\nabla)w_i=S_i$	(84)
Liquid water	$\frac{\partial(\varepsilon\rho_l s)}{\partial t}+\nabla\cdot(-\rho_l D_s\nabla s)+\nabla\cdot\left(\rho_l\frac{\mu_g}{\mu_l}\frac{K^l}{K^g}\mathbf{u}\right)=S_{liq}$	(85)
Dissolved water	$\frac{\partial\left(\frac{\rho_{mem}}{EW}\lambda\right)}{\partial t}+\nabla\cdot\left(-\frac{\rho_{mem}}{EW}D_{H_2O}^{Naf}\nabla\lambda\right)+\nabla\left(-\frac{n_d}{F}\sigma_l\nabla\phi_l\right)=S_\lambda$	(86)
Energy	$(\rho c_p)_{eff}\frac{\partial T}{\partial t}+(\rho c_p)_{eff}\mathbf{u}\cdot\nabla T+\nabla\cdot(-k_{eff}\nabla T)=S_T$	(87)

Fluxes of the nitrogen and oxygen through the membrane form the cathode side to the anode side are included in the P3D model. These fluxes are defined based on the difference between the partial pressures of them at the cathode and anode sides:

$$N_{N_2}^{ca-an} = M_{N_2}\psi_{N_2}\frac{\left(p_{N_2}^{ca} - p_{N_2}^{an}\right)}{\delta_m} \tag{88}$$

$$N_{O_2}^{ca-an} = M_{O_2}\psi_{O_2}\frac{\left(p_{O_2}^{ca} - p_{O_2}^{an}\right)}{\delta_m} \tag{89}$$

where δ_m is the thickness of the membrane, and ψ_{N_2} and $\psi_{O_2}$are the membrane-water-content dependent coefficients of the nitrogen and oxygen permeance through the membrane, respectively, and given by [43]:

$$\psi_{N_2} = 10^{-14}\left(0.0295 + 1.21 f_v - 1.93 f_v^2\right)\exp\left(\frac{24000}{R}\left(\frac{1}{T_{ref}} - \frac{1}{T}\right)\right) \tag{90}$$

$$\psi_{O_2} = 10^{-14}\left(0.11 + 1.9 f_v\right)\exp\left(\frac{20000}{R}\left(\frac{1}{T_{ref}} - \frac{1}{T}\right)\right) \tag{91}$$

In the previous model, developed in chapter 2, liquid water saturation was only considered in the cathode, whereas here mass exchange between the water vapor and the liquid water is added to the mass sources for the water vapor at the anode GDL. Thus, the TP flux of the water vapor at the anode GDL is modified as:

$$N_{H_2O}^{an} = -S_{phase}h_{GDL} - k_{ads}\frac{\rho_{mem}}{EW}\left(\lambda_{an}^{eq} - \lambda_{an}\right)M_{H_2O} \tag{92}$$

Liquid water distribution and transport in the anode GDL and channel and the CLs are considered. Liquid water sources in the GDLs and anode channel are defined as:

$$S_{liq}^{ca,GDL} = S_{phase} + \left(\frac{J_{cell}}{2Fh_{GDL}} - S_{\lambda} \right) M_{H_2O} + S_{liq}^{GDL-ch} - S_{liq}^{ca-an} \tag{93}$$

$$S_{liq}^{\text{an},GDL} = S_{phase} + S_{liq}^{GDL-ch} + S_{liq}^{ca-an} \tag{94}$$

$$S_{liq}^{ch} = S_{phase} - S_{liq}^{GDL-ch} \tag{95}$$

The pressure-driven permeation of the liquid water through the membrane, $S_{liq}^{ca\text{-}an}$, which is used to add the transport of the liquid water through the membrane form the cathode to anode is given by [107]:

$$S_{liq}^{ca-an} = \rho_l \frac{K_l}{\mu_l} \frac{p_l^{ca} - p_l^{an}}{\delta_m} \tag{96}$$

Here, p_l the pressure of the liquid phase which is determined based on the gas phase and capillary pressures.

Continuity of the capillary pressure at the GDL/CL interface, [107], is used to evaluate the liquid water saturation at the CLs:

$$p_c^{CL} = p_c^{GDL} \tag{97}$$

Capillary pressure at the CL is defined based on the Leverett function [15]:

$$p_c = \sigma \cos\theta \left(\frac{\varepsilon}{K} \right)^{0.5} J(s) \tag{98}$$

$$J(s) = \begin{cases} 1.42(1-\text{s}) - 2.12(1-\text{s})^2 + 1.26(1-\text{s})^3 & \theta < 90^\circ \\ 1.42\,\text{s} - 2.12s^2 + 1.26\,\text{s}^3 & \theta > 90^\circ \end{cases} \tag{99}$$

where σ and θ are the surface tension and contact angle, respectively.

3.1.2. Carbon corrosion

Oxygen crosses over the membrane to the anode side at hydrogen-starved regions because of the concentration difference. Therefore, oxygen reduction reaction (ORR) takes place at the anode side at the hydrogen-starved regions which reduces the interfacial potential and leads to higher potential for the cathode side high enough for the carbon corrosion reaction (CCR) at the cathode CL:

$$C + 2H_2O \rightarrow CO_2 + 4H^+ + 4e^- \tag{100}$$

It has been shown that CCR at the anode CL is negligible [92]. Therefore, reactions allowed to occur at the anode side are HOR and ORR, and at the cathode side are ORR and CCR. The concentration-dependent Butler-Volmer equation is used to describe HOR at the anode side [95].

The cathodic part of the Butler-Volmer equation is used to describe the ORR at the anode side [73]:

$$J_{ORR}^{an} = J_{ORR}^{ref}\left(\frac{c_{O_2}^{CL}}{c_{O_2}^{ref}}\right)\exp\left[-\frac{\left(1-\alpha_{O_2}\right)F}{RT}\left(V_s^{an} - V_m^{an} - V_{O_2}^{eq}\right)\right] \tag{101}$$

Two-phase agglomerate model is used to describe the ORR at the cathode side [95].

The anodic part of the Butler-Volmer equation with Langmuir adsorption term is used to describe the CCR at the cathode side [73,85,92]:

$$J_{CCR}^{ca} = J_{CCR}^{ref}\varepsilon_C\theta_C \exp\left[\frac{\alpha_C F}{RT}\left(V_s^{ca} - V_m^{ca} - V_C^{eq}\right)\right] \tag{102}$$

where J_{CCR}^{ref} is the reference current density of CCR, ε_C a factor corrects the reaction kinetics based on the remaining carbon, α_C the charge transfer coefficient for the CCR, V_s^{ca} and V_m^{ca} are the solid and electrolyte potentials at the cathode side, respectively, V_C^{eq} the equilibrium potential of CCR, and θ_C the Langmuir isotherm that is used to moderate the CCR rate at potentials less than V_θ [85]:

$$\theta_C = \frac{\exp\left[\frac{F}{RT}\left(V_s^{ca} - V_m^{ca} - V_\theta\right)\right]}{1+\exp\left[\frac{F}{RT}\left(V_s^{ca} - V_m^{ca} - V_\theta\right)\right]} \tag{103}$$

The factor ε_C is given by [92]:

$$\varepsilon_C = \left[\frac{m_C}{m_{C,0}}\right]^q \tag{104}$$

Here, m_C and $m_{C,0}$ are the remaining and initial masses of the carbon per unit area, respectively, and q is the power factor that can be fitted based on the experimental observations. The carbon mass loss is calculated based on the CCR rate [92]:

$$\frac{\partial m_C}{\partial t} = -\frac{M_C J_{CCR}^{ca}}{4F} \tag{105}$$

The net current density at the anode and cathode sides is the summation of the main and parasitic reactions which is equal for both sides:

$$J_{cell} = J_{HOR}^{an} + J_{ORR}^{an} = J_{ORR}^{ca} + J_{CCR}^{ca} \tag{106}$$

It has to be noted that the anodic current, producing proton, is positive and the cathodic current, consuming proton, is negative. Activation overpotential is defined based on the solid, electrolyte, and equilibrium potentials:

$$\eta = V_s - V_m - V^{eq} \tag{107}$$

3.1.3. Boundary conditions

Following boundary conditions are considered for the open-ended anode (OEA) operation mode. Inlet boundary conditions are the operating temperature, constant velocities based on the stoichiometric flow ratios (Eqs. (77) and (78)), and mass fractions

of the species calculated based on the inlet relative humidity (Eqs. (79) and (80)). Outlet boundary conditions are the specified pressure, and the outflow boundary conditions for the temperature, liquid water, and species (Eq. (81)).

For the dead-ended anode (DEA) operation mode, the boundary conditions for the anode flow field are changed to 2.5 atm pressure at the inlet and zero velocity at the anode outlet. Moreover, relative humidity (RH) at the anode inlet is set to 0.25 [45].

3.1.4. Numerical approach

Brinkman, Maxwell-Stefan, Butler-Volmer, liquid water saturation, dissolved water, and energy equations are coupled and solved numerically by the commercial finite element package COMSOL Multiphysics. Quadrangular mesh over the channels and the ribs are used to discretize the governing equations. Linear finite-elements are used in the polarization curve studies, while quadratic finite-elements are used for the transport equations in the anode side for the dead-ended-anode (DEA) and the anode-bleeding (AB) studies. Fully coupled solver with Newton iterations and direct PARDISO solver are used to solve the linear system of equations. Transient simulations for the DEA and AB operation modes take about two days on a high-end workstation.

3.2. Experiments

A detailed description of the experimental setup and procedures are given in [45], and a summary is presented here. The Pt-loading of 0.5 mg/cm^2 is used for the catalyst coating of both GDLs by hand-spraying. The membrane electrode assembly (MEA) was produced by hot-pressing a Nafion 212 membrane in between two identical catalyst-coated Sigracet 39 BC GDLs and Teflon coated fiberglass gaskets. Experiments were performed using a Model 850e (Scribner Associates Inc., USA) fuel cell test station. The experimental

setup enables to operate the fuel cell in the flow-through (FT), dead-ended-anode (DEA) and anode-bleeding (AB) operation modes [45].

The anode and cathode sides were supplied with hydrogen and air at 100% relative humidity (RH) respectively for the polarization curves obtained in the FT mode. In the DEA and AB operation modes, the anode and cathode sides were supplied with hydrogen and air at the RHs of 25% and 100%, respectively. Both the anode and cathode mass flow controllers were fully opened so that the flow was driven by the pressure difference, which is set to 1.5 atm for both sides at the backpressure unit. The cell was operated under the galvanostatic operation during the DEA and AB operation modes. The leak-free operation was confirmed by the typical DEA voltage transients.

3.3. Results

3.3.1. Model validation

Figure 10 shows an excellent agreement between the polarization curves from the P3D model and the experimental data for the cells with active areas of 8.17, 8.9, and 25 cm^2 for the operation, geometric, and model parameters listed in Tables 8 and 9. Charge transfer coefficients for the HOR and ORR and the mass transport coefficient for the liquid water transport between the GDL and channel are varied slightly, as listed in Table 9. These changes are due to small differences between handmade membrane electrode assemblies (MEA), which are prepared by coating the CL on the GDL manually.

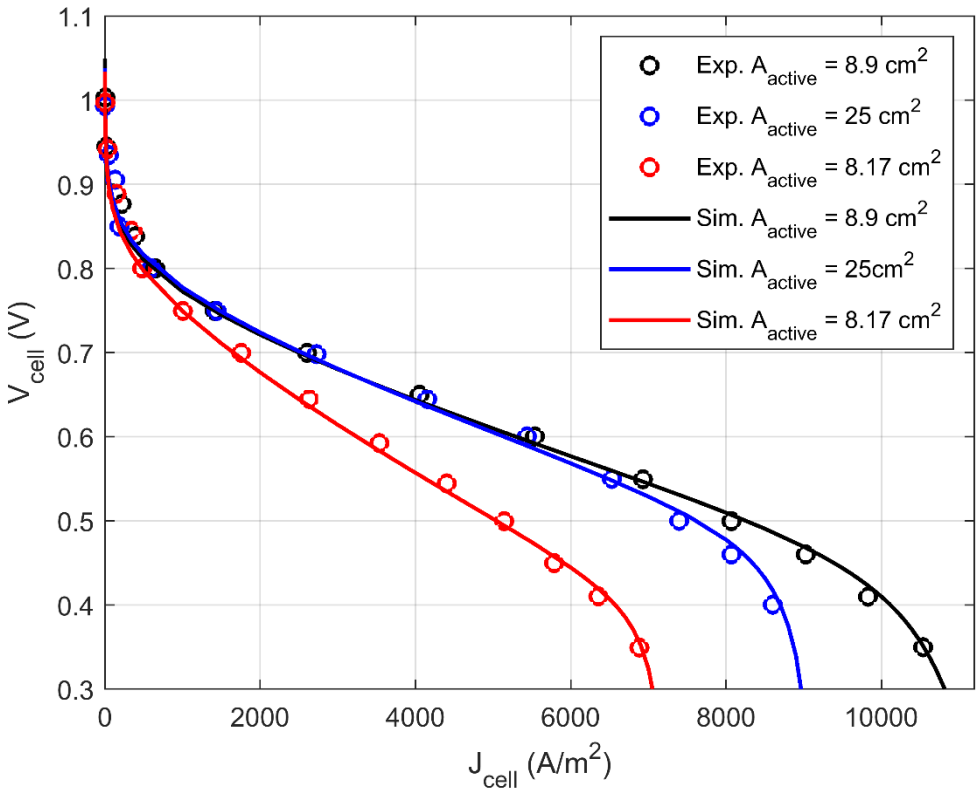

Figure 10: Comparisons of the polarization curves from the simulations and the experimental data for the cells with active areas of 8.17, 8.9, and 25 cm^2

Figures 11a and 11b show a good agreement for the transient cell voltage during the DEA operation from the P3D model and the experimental data for the cell current densities of 6700 and 5000 A/m^2 for the 8.17- and 25-cm^2 cells, respectively; black circles in the graphs represent the average values of 46 and 3 cycles for the 8.17-cm^2 cell and the 25-cm^2 cell, respectively, and error bars correspond to the minimum and maximum values. Simulation results slightly underestimate the initial drop in the cell voltage following the purge for the 8.17-cm^2 cell.

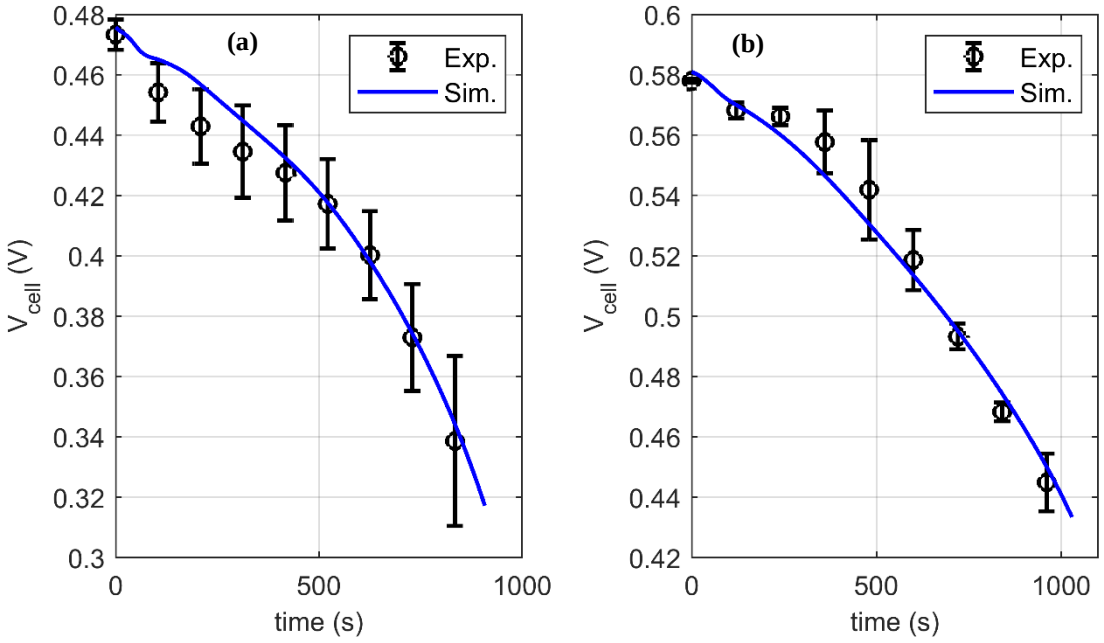

Figure 11: Comparisons of the cell voltage transients from the simulations and experimental data for: a) 8.17-cm^2 cell with the cell current density of 6700 A/m^2, and b) 25-cm^2 cell with the cell current density of 5000 A/m^2

3.3.2. Anode bleeding rate optimization

In the anode-bleeding (AB) operation mode, a bleed rate is prescribed as an ultra-low flowrate at the anode exit to discharge the crossover gasses, especially nitrogen from the anode. The bleed rate must be slightly larger than the crossover rate of nitrogen through the membrane to sustain a stable transient cell voltage and to avoid carbon corrosion reaction (CCR) at the cathode CL while maintaining a high utilization rate of hydrogen. Figures 12 and 13 show the effects of the anode bleed rate on the cell voltage drop and average carbon corrosion rate for the 8.17- and 25-cm^2 cells, which operate at the load current densities of 6700 and 5000 A/m^2 respectively. According to the figures, the cell voltage is stable for the bleed rates higher than 30 and 60 µl/min for the 8.17- and 25-cm^2 cells, respectively, and consistently with the experimental data reported in [45], while the hydrogen utilization for these bleed rates is 99.9%. Moreover, the carbon corrosion is not

observed at the cathode CL at these bleed rates, and very low even for the bleed rate of 7.5 µl/min for the 8.17-cm^2 cell, since the cathode interfacial potential (0.96 V) is below the limiting potential of 1 V, as suggested by [85] and used in the Langmuir isotherm given by Eq. (103). Reiser et al. [73] showed that the cathode interfacial potential is increased to about 0.59 V above the cell potential in the hydrogen starved parts of the active area. In principle, the CCR can be diminished by operating the cell at low potentials less than 0.4 V even in the case of localized hydrogen starvation under DEA and AB operation modes. However, operating the cell at low potentials (high currents) leads to important issues such as flooding and overheating of the membrane.

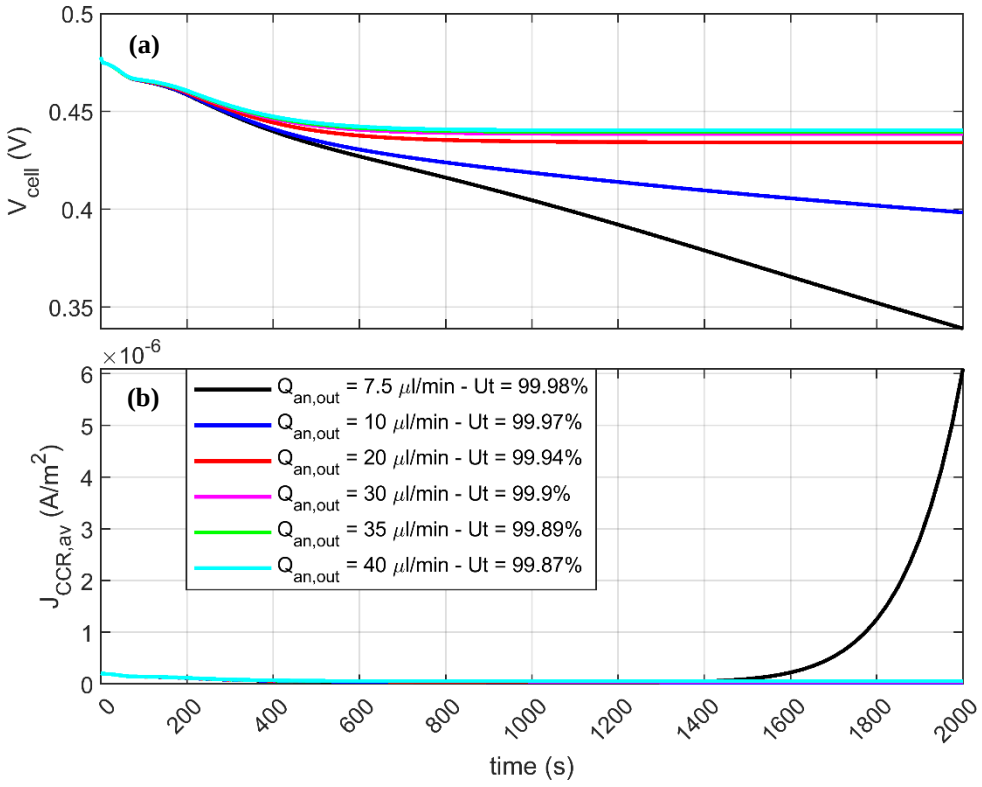

Figure 12: Effect of the anode bleeding rate on: a) cell voltage drop, and b) average carbon corrosion rate for the cell with active area of 8.17 cm^2

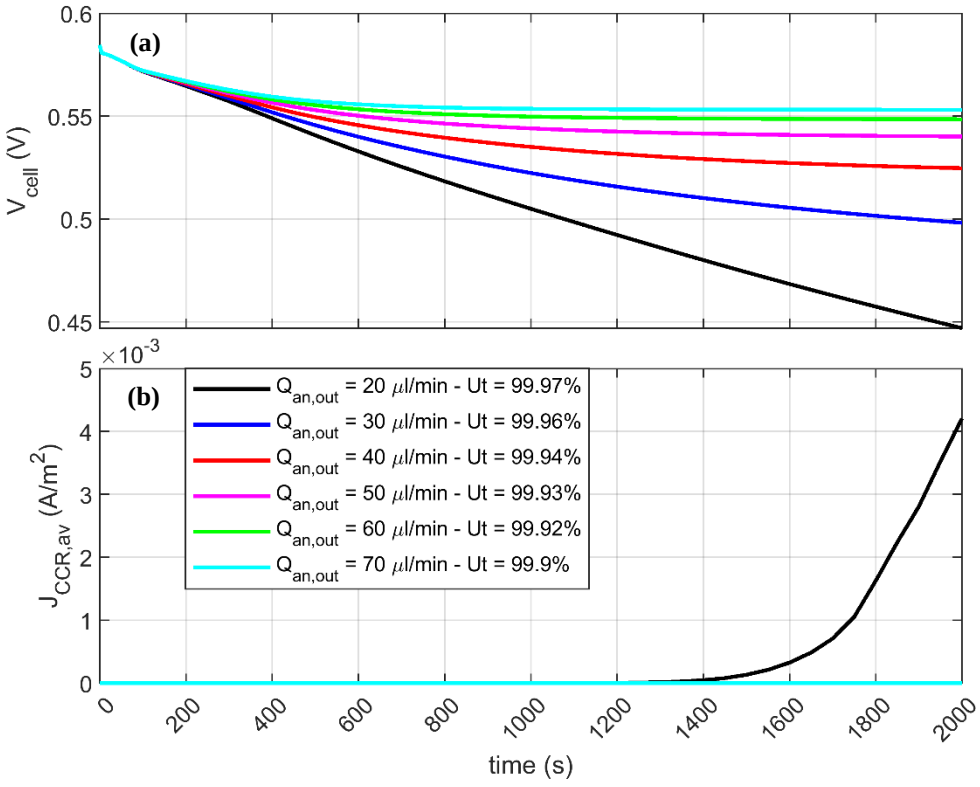

Figure 13: Effect of the anode bleeding rate on: a) cell voltage drop, and b) average carbon corrosion rate for the cell with active area of 25 cm^2

3.3.3. Effects of the operating conditions on anode bleeding operation

The difference between the partial pressures of nitrogen between the cathode and the anode is the main driving force for nitrogen crossover, Eq. (88). The crossover rate is very small but if the exit is closed, blocked, or the exit flow rate is very low then nitrogen accumulates in the anode channels. The accumulated nitrogen in the anode leads to localized hydrogen starvation, which causes a drop in the cell voltage and carbon corrosion in the cathode CL. Operating conditions play an important role on the nitrogen accumulation rate and the cell performance as the permeation rate of nitrogen through the membrane strongly depends on the water content of the membrane. The cell performance under the anode-bleeding (AB) operation mode depends on the operating conditions as well

as the bleed rate. In order to isolate the effects of the operating conditions per se, voltage transients of the 25-cm^2 cell under the AB operation with the bleed rate of 30 µl/min are considered here. The effects of the operation conditions are studied one at a time while the other conditions are fixed, and the results are shown in Figure 14.

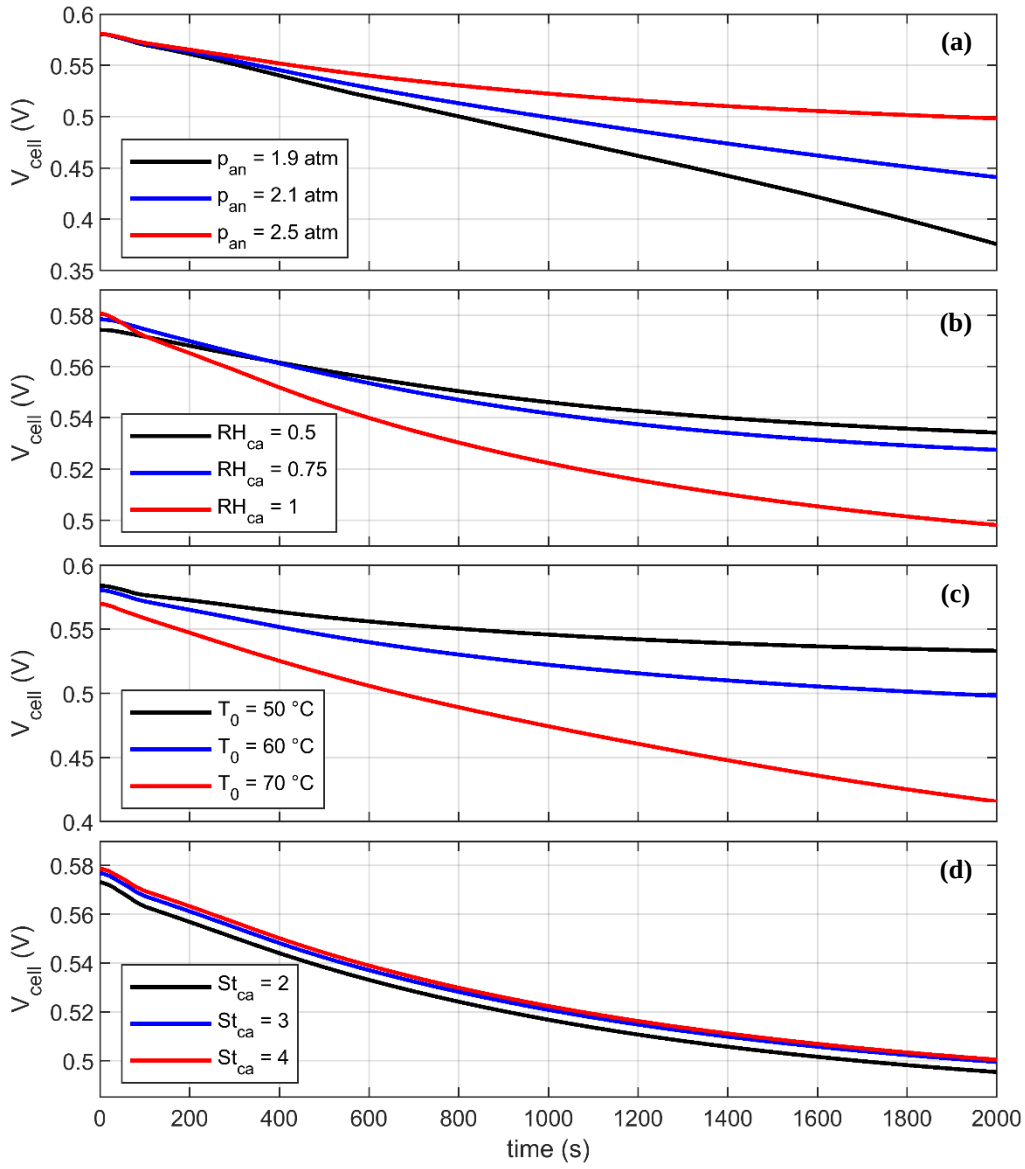

Figure 14: Effects of the operating conditions: a) anode pressure, b) relative humidity of the reactants at the cathode inlet, c) cell temperature, and d) flow stoichiometric ratio at the cathode inlet on the transient cell voltage during the anode bleeding (AB) performance for the cell with active area of 25 cm^2 and bleeding rate of 30 µl/min

Figure 14a shows the effect of the anode pressure on the transient cell-potential under the AB operation. The cell potential increases with the anode pressure, as also reported by [45], which is due to decreasing crossover rate as the partial pressure of nitrogen increases in the anode as described in Eq. (88).

The cell potential drop decreases as the relative humidity of the cathode (RH_{ca}) decreases, as shown in Fig. 14b. A lower RH_{ca} leads to a lower water content in the membrane reducing the permeance and crossover rate of nitrogen, as indicated in Eq. (90), hence the nitrogen accumulation in the anode and the cell potential drop decrease together. Despite the improvement of the AB performance for a lower RH_{ca}, its effect is opposite at the beginning of the cycle due to the increasing ohmic loss in the membrane as the water content decreases [95,127].

Cell temperature has an impact on the crossover rate of nitrogen, saturation pressure, reaction kinetics, and the proton conductivity of the electrolyte phase [113]. Figure 14c indicates that the drop in the cell potential increases with the cell temperature because of the direct effect of temperature on the nitrogen permeance through the membrane, as given in Eq. (90).

Lastly, the effect of the cathode stoichiometric flow ratio (St_{ca}) is shown in Fig. 14d. A higher St_{ca} slightly decreases the cell-potential loss during the transient as a higher flow rate can discharge the liquid water from the cathode channels more effectively and results in a slight dry out of the membrane that reduces the crossover rate of nitrogen to the anode side. However, the rate of performance improvement with the St_{ca} is very small and increasing the St_{ca} increases the parasitic power.

3.3.4. Flow field design for anode bleeding operation

The 8.17-cm^2 cell is used to compare three different flow field designs in the anode while the cathode has serpentine channels: serpentine (sp-sp), straight (st-sp) and interdigitated (int-sp). Figure 15 shows the comparison of the polarization curves for these configurations for the model parameters listed in Tables 8 and 9. Polarization curves (cells

performance) are almost the same for all flow field designs for the flow-through (FT) operation mode for both anode and cathode sides.

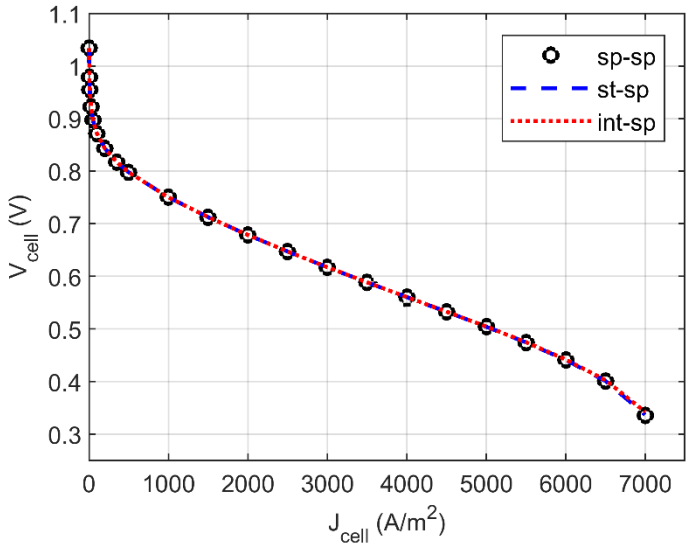

Figure 15: Comparison of the polarization curves for the flow field designs with the serpentine channels for the anode and cathode flow fields (sp-sp), straight and serpentine channels for the anode and cathode flow fields, respectively, (st-sp), and interdigitated and serpentine channels for the anode and cathode flow fields, respectively, (int-sp)

A level-set metric is used to quantify the coverage ratio of hydrogen in the anode as the normalized portion of the active area where the hydrogen mole fraction exceeds a certain mole-fraction limit, $0 < x_k < 1$:

$$\Phi = \frac{A(x_{H_2} > x_k)}{A_{active}} \tag{1}$$

where A_{acitve} is the total active area.

Figure 16a shows the comparisons of the coverage ratios for mole-fraction limits of 0.4, 0.6 and 0.8 as a function of the bleed rate for different flow field designs under the average current density of 5000 A/m^2. The coverage ratio drops sharply below one for all designs when the bleed rate is smaller than a limit that depends on the mole-fraction limit. Coverage ratios are the highest for the serpentine channels at very low bleed rates,

however, there is a crossover bleed rate for which the coverage for the serpentine channels becomes the lowest as the bleed rate increases to limit rate for which the ratio drops below one.

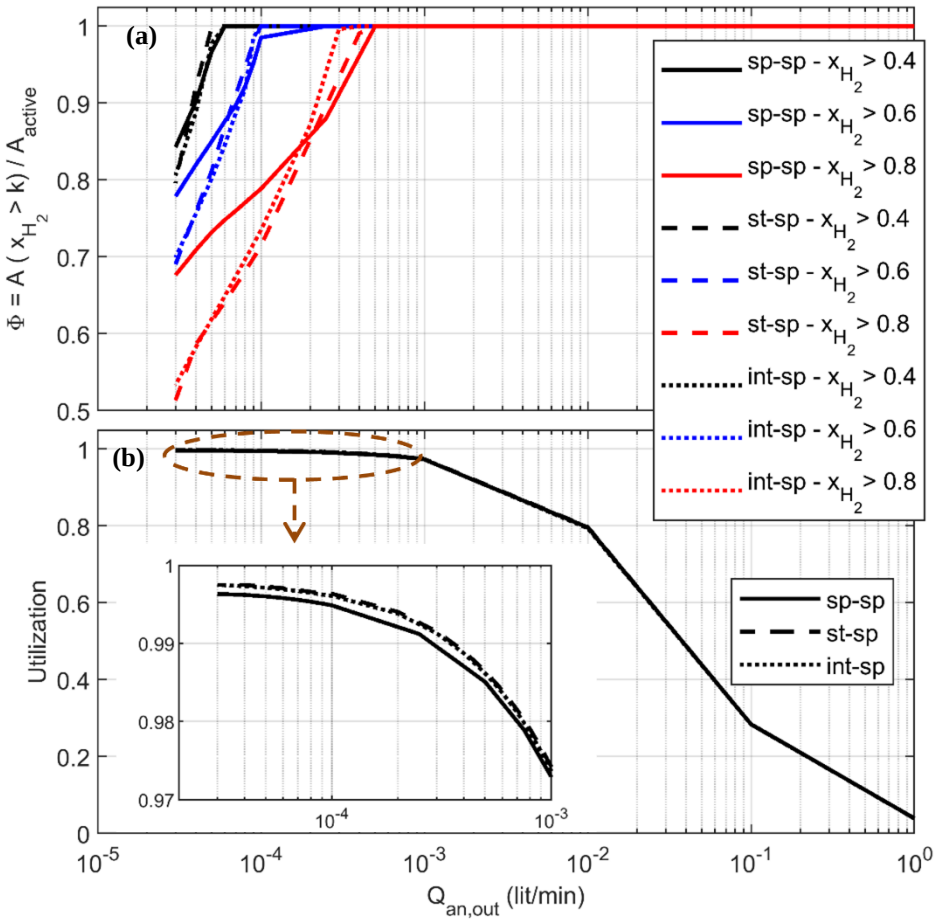

Figure 16: Comparisons of: a) hydrogen coverage metric, Φ, and b) hydrogen utilization versus bleeding rate for the cell current density of 5000 A/m^2 and the cell designs with the serpentine channels for the anode and cathode flow fields (sp-sp), straight and serpentine channels for the anode and cathode flow fields, respectively, (st-sp), and interdigitated and serpentine channels for the anode and cathode flow fields, respectively, (int-sp)

According to Figure 16b, the anode-flow-field design does not have a strong impact on the hydrogen utilization, which is higher than 99% for the bleeding rates less than 2×10^{-4} lit/min for all flow fields. The hydrogen utilization is slightly lower (~0.1%) for the cell

with serpentine channels than for the cells with straight or interdigitated channels in the anode flow field. Overall, serpentine channels in the anode flow field can be deemed to have a better performance under the AB operation mode.

Figure 17 shows the mole fractions of hydrogen in the anode GDL for the flow field designs (sp-sp, st-sp, and int-sp) considered here and for the bleed rate of 3×10^{-5} lit/min which causes hydrogen starvation near the exit of the anode. According to the figure, the coverage ratio of hydrogen is the highest for the cell with serpentine channels in the anode. For instance, for the mole fraction limit of 0.8, the coverage ratio of hydrogen is about 0.68 for the serpentine channels while it is about 0.51 for the straight and interdigitated channels.

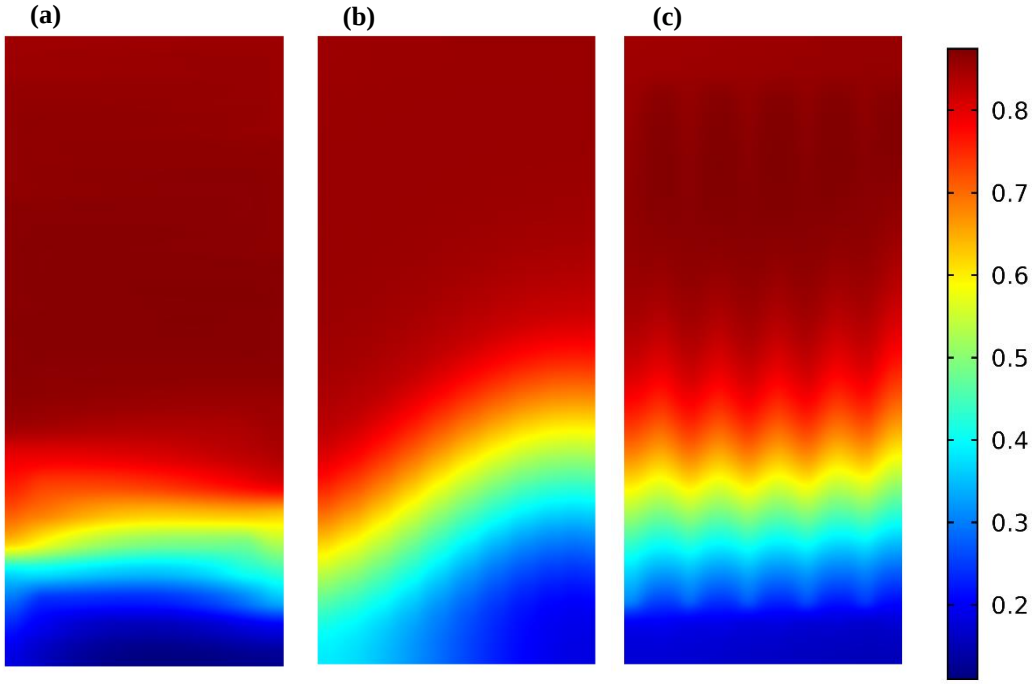

Figure 17: Comparison of the hydrogen distribution in the anode GDL for the bleeding rate of 3×10^{-5} lit/min and cell current density of 5000 A/m^2 for the cell designs with: a) serpentine channels for the anode and cathode flow fields (sp-sp); b) straight and serpentine channels for the anode and cathode flow fields, respectively, (st-sp); and c) interdigitated and serpentine channels for the anode and cathode flow fields, respectively, (int-sp); inlet and outlet are at the upper left and bottom right edges, respectively

Finally, the P3D model is used to investigate the performance of a large cell with an active area of 336 cm^2 under the AB operation mode. Serpentine channels with 19 channels and 2 turns are used for the anode and cathode flow fields. Figure 18 shows the hydrogen coverage level and utilization versus the bleeding rate for this cell. Hydrogen utilization exceeds 99% for the bleed rates less than 10^{-2} lit/min while the hydrogen starvation is not observed, i.e. the mole fraction of hydrogen is above 0.45 everywhere in the anode.

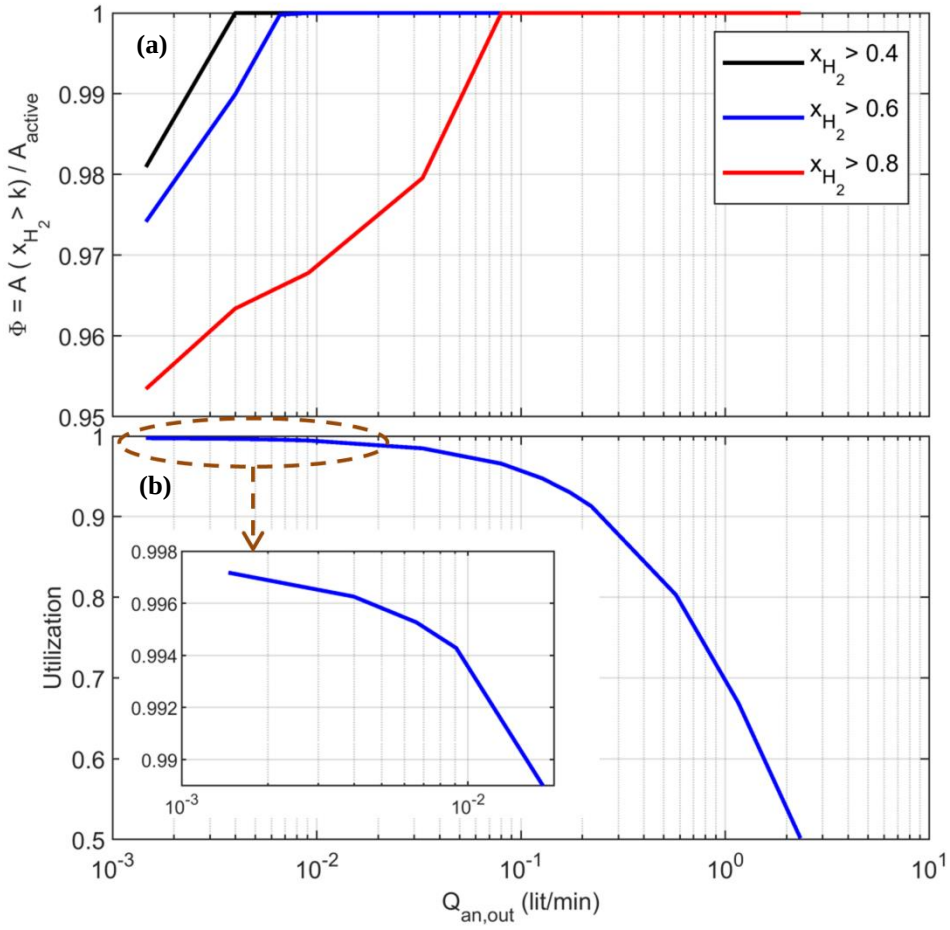

Figure 18: a) Hydrogen coverage metric, Φ, and b) hydrogen utilization versus bleeding rate for the large cell with active area of 336 cm^2 and the cell current density of 10^4 A/m^2

Figures 19a and 19b show the hydrogen distribution in the anode channels and GDL, respectively, for the anode bleeding rate of 1.5×10^{-3} lit/min and the cell current density of 10^4 A/m^2. Hydrogen utilization for this bleeding rate is about 99.7% while

hydrogen mole fraction is more than 0.45 over the active area. Therefore, a stable transient operation without carbon corrosion is expected for this cell design under the AB mode with mentioned operating conditions while the cost of the cell is reduced by losing less amount of hydrogen.

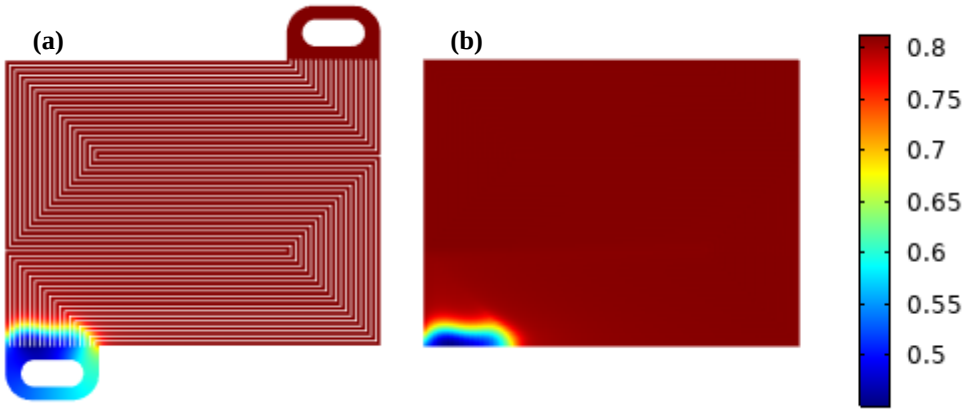

Figure 19: Hydrogen distribution in the anode: a) channel, and b) GDL for the bleeding rate of 1.5×10^{-3} lit/min and cell current density of 10^4 A/m^2

Chapter 4

EFFECTS OF GEOMETRIC AND OPERATION PARAMETERS ON THE PEM FUEL CELL WITH DEAD-ENDED ANODE MODE

The high energy density of hydrogen is very advantageous for automotive applications; however high cost and low durability of proton exchange membrane (PEM) fuel cells limit the commercial use. Dead-ended anode (DEA) is an operation mode that is used to reduce the PEM fuel cell cost by improving the hydrogen utilization. In this chapter, the pseudo-three-dimensional (P3D), transient, two-phase, and non-isothermal model developed in chapter 3 is used to study the cell performance and carbon corrosion during dead-ended and anode bleeding operation modes. The model is validated against the experimental data reported by Abbou et al. [96] and used to investigate the effects of the geometric and operation parameters on the voltage transients and carbon corrosion rates. Results demonstrate that lower load current density, higher anode pressure, the lower relative humidity of the reactants at the cathode inlet, higher stoichiometric flow for the cathode, higher cell temperature, and shorter, deeper and wider channels can improve the cell performance under the dead-ended anode operation. Finally, optimal anode bleeding rate is obtained to sustain a stable transient cell voltage without the carbon corrosion reaction in the cathode catalyst layer while the hydrogen utilization is kept at more than 99%.

4.1. Methodology

The transient P3D model with two-phase and non-isothermal assumptions, developed in chapter 3, is used for a PEMFC with counter-flow single straight channels, which are

projected on a surface as demonstrated in Fig. 1. The anode and cathode channels and ribs overlap due to the symmetry of the flow fields.

4.1.1. Governing equations

Two-dimensional Brinkman and Maxwell-Stefan equations are used to obtain the flow field and species transport, respectively, in the channels and GDLs. Electrochemical reaction rates of the anode HOR and ORR and cathode CCR are calculated from the Butler-Volmer equations, and the cathode ORR rate is obtained from the agglomerate model. Moreover, the transport of liquid water saturation in the cathode and anode GDLs and anode channel, dissolved water in the electrolyte phase, and the temperature are included in the model. Cell geometry and operating conditions are given in Table 11, and the values of the model parameters are listed in Table 12. Detailed discussion of the governing equations can be found in chapters 2 and 3.

Table 11: Cell geometry and operating conditions

Parameter	Value	Description
L	3×10^{-1} m	Channel length
w_{ch}	1×10^{-3} m	Channel width
w_{rib}	1×10^{-3} m	Rib width
h_{ch}	5×10^{-4} m	Channel height
h_{GDL}	2×10^{-4} m	GDL thickness
δ_{CL}	15×10^{-6} m	CL thickness
δ_m	25×10^{-6} m	Membrane thickness
ε_{GDL}	0.76	GDL porosity [97]
ε_{CL}	0.2	CL porosity [15]
T, T_{ref}	338 and 298 K	Operating and reference temperatures
p, p_0	1 atm	Operating and reference pressures

$RH_{\{an,ca\}}$	0.9 and 0.7	Anode and cathode relative humidity

Table 12: Parameters and their values used in the model

Parameter	Value	Description
K_{GDL}	5.09×10^{-12} m^2	GDL intrinsic permeability [98]
K_{cond}	1 s^{-1}	Condensation coefficient [15]
K_{evap}	5×10^{-5} Pa^{-1}s^{-1}	Evaporation coefficient [15]
$\sigma_{GDL}^{\{th,in\}}$	500 and 5000 S m^{-1}	GDL through and in-plane electrical conductivities [99]
σ_{CL}	500 S m^{-1}	CL electrical conductivity [99]
$k_{GDL}^{\{th,in\}}$	1.7 and 21 W m^{-1} K^{-1}	GDL through and in-plane thermal conductivities [99]
k_{CL}	1 W m^{-1} K^{-1}	CL thermal conductivity [99]
k_{mem}	0.95 W m^{-1} K^{-1}	Membrane thermal conductivity [99]
ρ_{mem}	1.98×10^{3} kg m^{-3}	Density of the dry membrane
EW	1.1×10^{3} kg mol^{-1}	Equivalent weight of the membrane
V_m	9×10^{-4} m^3 mol^{-1}	Molar volume of the membrane
Nu	2.98	Nusselt number for laminar flow in a rectangular channel with constant temperature at the channel perimeter
α_{H_2}	0.7	Charge transfer coefficient of HOR
α_{O_2}	1	Charge transfer coefficient of ORR
α_C	0.275	Charge transfer coefficient of CCR [85]
$J_{HOR}^{ref,343K}$	2.82×10^{3} A m^{-2}	Exchange current density of HOR at 343 K [15]
$J_{ORR}^{ref,343K}$	0.1065 A m^{-2}	Exchange current density of ORR at 343 K [15]
J_{CCR}^{ref}	6×10^{-7} A m^{-2}	Reference current density of CCR
$V_{H_2}^{eq}$	0 V	Equilibrium potential of HOR [73]
$V_{O_2}^{eq}$	1.196 V	Equilibrium potential of ORR [85]
V_C^{eq}	0.207 V	Equilibrium potential of CCR [85]
V_θ	1 V	Reference potential of Langmuir isotherm [85]
$m_{C,0}$	2×10^{-3} g cm^{-2}	Initial loading of carbon per unit area [92]

$c^{ref}_{\{H_2,O_2\}}$	56.4 and 3.39 mol m^{-3}	H_2 and O_2 reference concentrations [11,100]
$c^{0}_{SO_3}$	1.2×10^{3} mol m^{-3}	Concentration of sulfonic in the membrane
D^{ch}_{s}	1×10^{-3} m^2 s^{-1}	Capillary diffusivity of the channel [15]
$h^{GDL\text{-}ch}_{s}$	1.25×10^{-6} m s^{-1}	Mass transport coefficient for the liquid water transport
$J_{loss,0}$	10 A m^{-2}	Parasitic current density
R_{solid}	1×10^{-6} Ω m^2	Cell components electric resistance
r_{pell}	1×10^{-7} m	Radius of the catalyst pellet [15]
δ^{Naf}	1×10^{-8} m	Thickness of the Nafion film around the catalyst pellet [15]
σ	0.0625 N m^{-1}	Surface tension of water
θ_{CL}	65°	Contact angle of the CL

4.1.2. Boundary conditions

Following boundary conditions are considered for the open-ended anode (OEA) operation mode. Inlet boundary conditions are the operating temperature, constant velocities [96], and mass fractions of the species calculated based on the inlet relative humidity (Eqs. (79) and (80)). Outlet boundary conditions are the specified pressure, and the outflow boundary conditions for the temperature, liquid water, and species (Eq. (81)).

For the dead-ended anode (DEA) operation mode, the boundary conditions for the anode flow field are changed to 1.3 bar pressure at the inlet and zero velocity at the anode outlet. Relative humidity (RH) at the anode inlet is set to zero, [96], for the dry inlet.

4.1.3. Numerical approach

COMSOL Multiphysics software is used to solve the coupled governing equations numerically. The unknowns are the velocities and pressures at the GDLs and the channels; hydrogen, oxygen, and water vapor mass fractions at the anode GDL and channel and

oxygen and water vapor mass fractions at the cathode GDL and channel; cell potential and cathode and anode activation overpotentials; liquid water saturation at the anode and cathode GDLs and CLs and the anode channel; membrane water content at the cathode- and anode-membrane interfaces and the middle of the membrane; and temperatures in the GDLs and channels; total of 33 variables.

Structured quadrilateral linear elements with double boundary layers at the rib-channel interfaces and a denser mesh close the inlets and outlets are used as shown in Fig. 20.

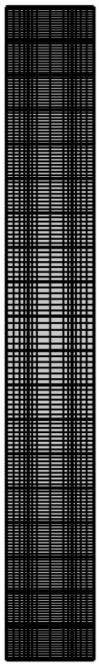

Figure 20: Mesh distribution, the channel is scaled by 1/20 in the y-direction

The number of elements and degrees of freedom (DOF) are about 2.9 and 94.5 K, respectively. The fully-coupled solver is used to solve nonlinear equations with Newton iterations, and the direct PARDISO solver is used to solve the linear system of equations at each iteration. The maximum time step is set to 5 seconds in transient simulations which employ the fifth-order backward-differences formula. The transient simulation for the DEA operation in Fig. 21b took about 5 hours and the peak memory usage of 3.86 GB on a workstation with an i7-6700 3.4 GHz quad-core processor.

4.2. Results

4.2.1. Model validation

The P3D model is validated against the experimental data reported in the literature [96] for a segmented cell with a counter flow in straight channels. Geometric, operation, and model parameters are listed in Tables 11 and 12. A 5-cm long reservoir with the same width and height of the channel is connected to the anode exit for the transient DEA simulations since the shut-off valve is not placed exactly at the end of the anode channel in practice, which has a small effect on the voltage transients. In addition to the polarization curves for the steady-state operation, cell voltage drops, local cathode and anode interfacial potentials, and current densities are compared for the DEA operation.

The agreement between the polarization curves from the P3D model and experiments reported in [96] is very good as shown in Fig. 21a, and an excellent agreement between the cell voltage drop during the DEA operation from the model and experimental data is shown in Fig. 21b.

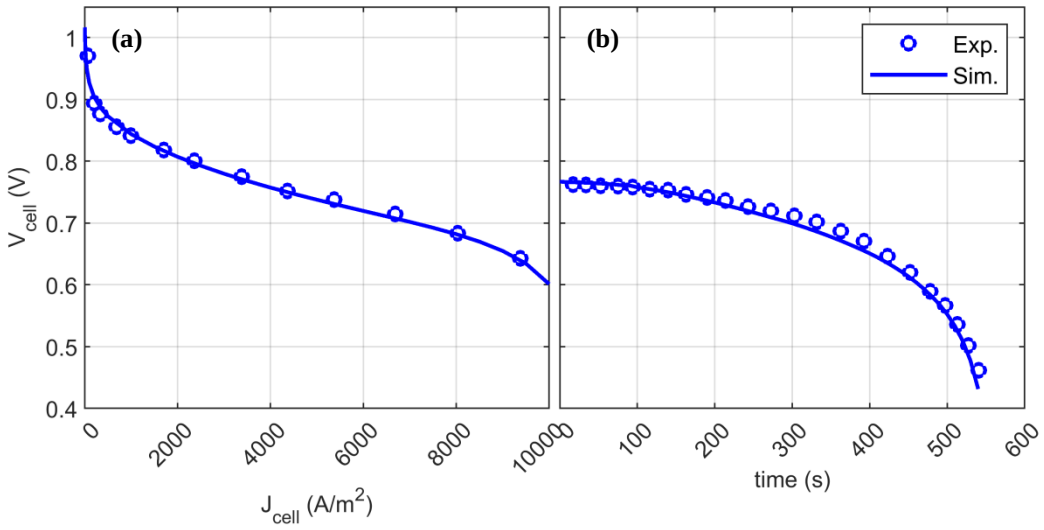

Figure 21: Comparisons of the model results and experimental data reported in [96]: a) polarization curves, b) transient cell voltages

In experiments [96], the cell is divided into 20 segments to obtain the local interfacial potentials and current densities; the segments are numbered in the air flow direction, i.e. segment 1 represents the cathode inlet or the anode outlet and segment 20 represents the cathode outlet or the anode inlet. Figures 22a-c show the comparisons of the cathode and anode interfacial potentials and current densities during the DEA operation at segments 1, 5, 10, 15, and 20. The model predicts the transients of local interfacial potentials and current densities very well. Having a convective effect, the flow of hydrogen in the anode channel pushes the nitrogen towards the end of the channel, [106], where the starvation of hydrogen first begins and propagates towards the anode inlet as the transient continues. Therefore, the current density goes to zero faster for the segments closer to the anode outlet than the ones closer to the inlet due to the gradual accumulation of nitrogen, as demonstrated in Fig. 22e. A good agreement is seen between the model and experimental data quantitatively for the beginning and middle of the DEA cycle, and some deviations are observed towards the end of the cycle.

Figures 22d and 22e show the model results for the variations of the hydrogen and nitrogen mole fractions at the anode side, respectively, during DEA at segments 1, 5, 10, 15, and 20. It is seen that the hydrogen mole fraction is about 0.8 at the beginning except for segment 20, which is located at the anode inlet with pure hydrogen, and drops to zero faster for the segments closer to the anode outlet than to the inlet, and the opposite behavior is seen for the nitrogen mole fraction variation. The model predicts that the water vapor accumulates very fast in the anode side and reaches an equilibrium RH-level the same as the cathode, demonstrating the self-humidification capability of the DEA operation.

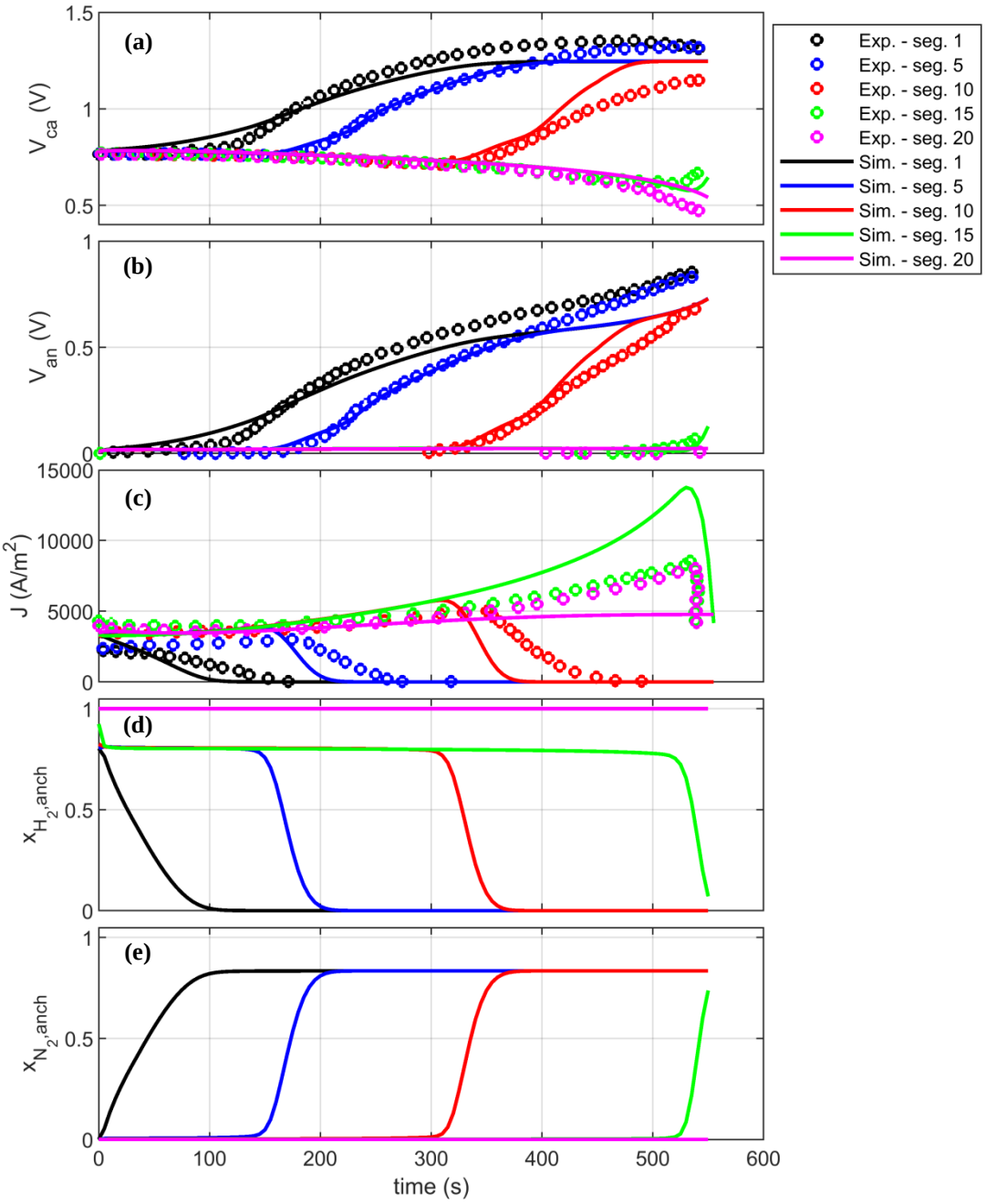

Figure 22: Comparisons of the model results and experimental data reported in [96]: a) cathode interfacial potentials, b) anode interfacial potentials, and c) current densities; and the model results for d) and e) hydrogen and nitrogen mole fractions at the anode side, respectively, at segments 1, 5, 10, 15, and 20

4.2.2. Effects of the operation parameters on dead-ended anode operation

As the cell potential drops during the DEA transient, the exit valve must be opened intermittently to discharge nitrogen and liquid water to recover the cell voltage. The time it takes for the cell voltage to drop to 0.5 V, $t_{0.5V}$, is chosen as the purge interval to show the effects of operation and geometric parameters on the DEA performance. The time-averaged crossover rate of nitrogen crossover during the transient is another metric that helps explain the effects of the operation and geometric parameters:

$$\dot{n}_{N_2,av} = \frac{1}{t_{0.5V}} \int_0^{t_{0.5V}} \int_{A_{active}} N_{N_2}^{ca-an} dA dt \tag{108}$$

Figure 23a shows the effect of load current density on the cell voltage for current densities of 3300, 6000, and 9000 A/m^2. The cell potential decreases faster as the cell current density increases consistently with previous reports [39,40]. Increasing the cell current density shortens the time it takes until the hydrogen starvation begins. Moreover, higher load currents lead to more water production and higher water content in the membrane, which increases the nitrogen permeance of the membrane as described in Eq. (90). Therefore, nitrogen transport through the membrane increases for higher current densities as well, as illustrated in Fig. 23f, and promotes the decrease in the purge interval.

A higher anode pressure can improve the DEA operation performance as demonstrated in Fig. 23b. The $t_{0.5V}$ increases about two times for a pressure increase of 0.6 bar at the anode side. The anode pressure increases the partial pressure of nitrogen at the anode side and reduces the crossover rate of nitrogen as described in Eq. (88) and shown in Fig. 23g.

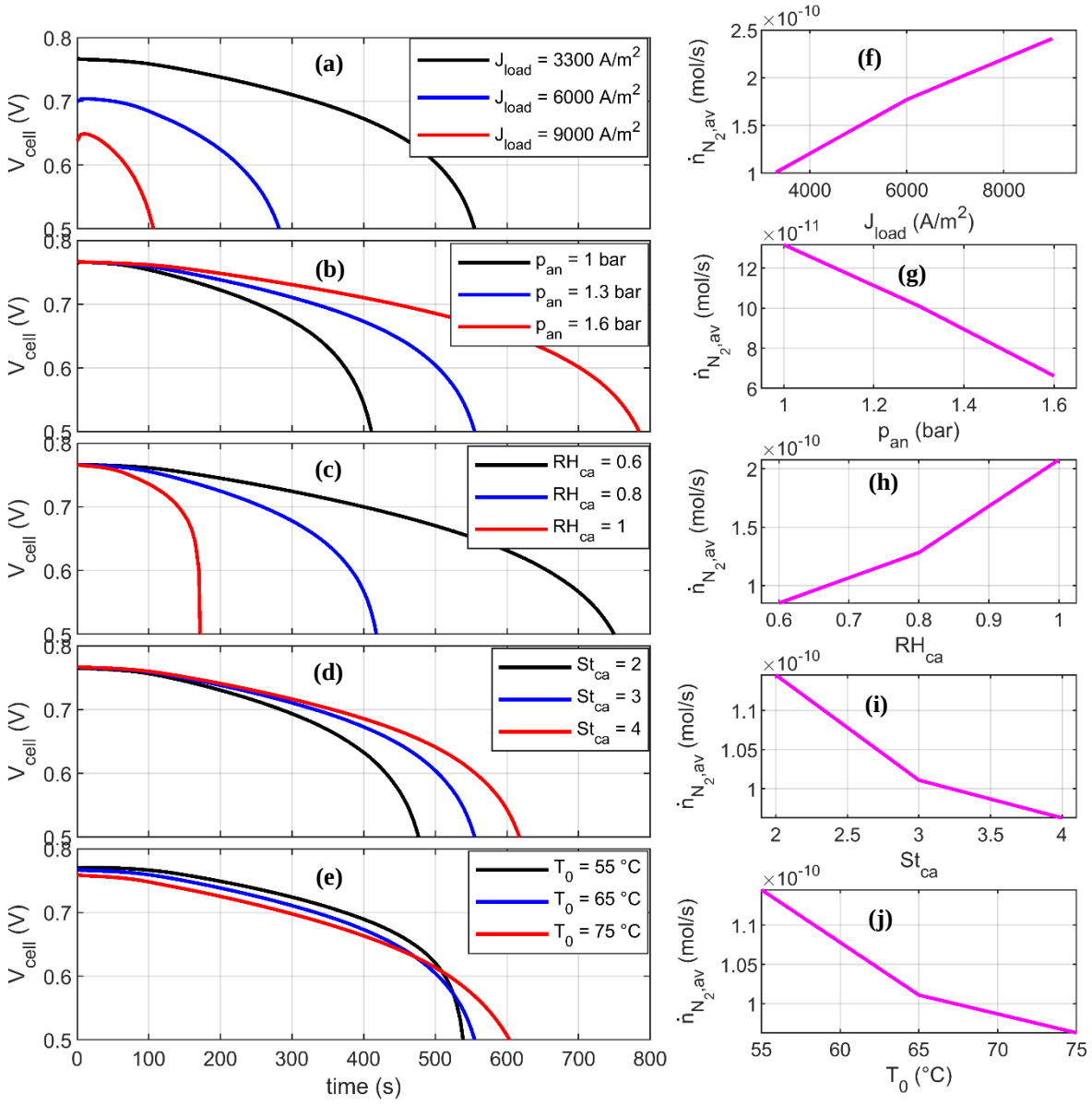

Figure 23: Effects of the operation parameters: a) load current density, b) anode pressure, c) relative humidity of the reactants at the cathode inlet, d) flow stoichiometric ratio at the cathode inlet, and e) cell temperature on the DEA performance, the time it takes for the cell voltage to drop to 0.5 V ($t_{0.5V}$); variation of the average nitrogen mole rate crossover the membrane versus f) load current density, g) anode pressure, h) relative humidity of the reactants at the cathode inlet, i) flow stoichiometric ratio at the cathode inlet, and j) cell temperature

The relative humidity (RH) of the anode and cathode inlets are important operating parameters that affect the DEA performance. Figure 23c shows the effect of the cathode RH on $t_{0.5V}$ for RH_{ca} values of 0.6, 0.8, and 1. The purge interval, $t_{0.5V}$, increases with decreasing RH_{ca} as reported by [39,40] also. As shown in Fig. 23h, the average crossover of nitrogen increases with RH_{ca} as well and decreases the purge interval. According to Eq. (90), nitrogen permeance of the membrane increases with the membrane water content, which increases with the cathode RH.

Figure 23d shows the effect of the cathode stoichiometric flow ratio (St_{ca}) on the cell voltage during the DEA transient. The purge interval, $t_{0.5V}$, improves with the increase in St_{ca}, as reported [39,40] also, e.g. an approximately 10% increase in $t_{0.5V}$ for two times increase in the cathode stochiometric flow. Higher St_{ca} can discharge the liquid water from the cathode side more effectively, which leads to a lower amount of the liquid water in the cell and lower water content in the membrane, which reduces the nitrogen transport to the anode side, as indicated in Fig. 23i. However, the parasitic power also increases to increase the cathode flow and the St_{ca}.

Figure 23e shows the effect of cell temperature on the cell voltage during the DEA transient. The purge interval, $t_{0.5V}$, improves slightly with the cell temperature. Even though the permeance of nitrogen increases slightly with the temperature, the overall effect of the cell temperature on the crossover rate is the opposite as illustrated in Fig. 23j due to the effect of the cell temperature on the overall water content of the membrane, which increases slightly with the cell temperature. Moreover, despite the slight improvement in $t_{0.5V}$ with the cell temperature, overall performance is opposite prior to the sharp voltage drop at the end of the DEA cycle.

Similarly to nitrogen, liquid water accumulates in the anode also as a result of back diffusion, pressure-driven permeation (Eq. (96)), and condensation of water vapor (Eq. (95)) in the anode channels. The formation of liquid droplets can clog the channels especially near the exit of the anode and cause local blockages that cause hydrogen starvation in the DEA operation. Abbou et al. [96] showed that when the anode (cathode) operates 2.5 °C higher (lower) than the cell temperature, the DEA performance improves due to the reduction in the liquid water at the anode side. The authors reduced the cathode

temperature to a degree equal to the increase in the anode temperature to keep the cell temperature the same. Our saturation-based model cannot predict this improvement since the saturation in the anode channels remains very low. It is likely that a few liquid droplets in the anode channel can cause a blockage in the channel and hydrogen starvation in the downstream in the absence of anode flow; when the anode temperature is increased, the droplet formation and blockage would be less, causing an improvement in the cell performance. Thus, other modeling approaches are necessary as the saturation-based two-phase models are not very effective in predicting the local effects of droplets.

4.2.3. Effects of the geometric parameters on dead-ended anode operation

Geometric parameters (length, width, and height of the channel) have a strong effect on the cell performance during the DEA operation as well. Figure 24a shows that $t_{0.5V}$ decreases with increasing channel length, which increases the active area and the nitrogen crossover as demonstrated in Fig. 24d, and thus the hydrogen starvation at the end of the channel is observed sooner.

Figure 24b shows that $t_{0.5V}$ increases with the depth of the channel, which does not have an effect on the active area but increases the anode volume, thus despite the slow increase in the crossover rate as shown in Fig. 24e, the onset of hydrogen starvation is delayed. The crossover rate increases due to the increase in the water content of the membrane when the convective velocity in cathode channels is lower. Similar to the effect of the St_{ca} on the DEA performance, a slight decrease in the convective velocity at the cathode channel leads to higher membrane water content and vice versa.

The purge interval, $t_{0.5V}$, increases with the increasing width of the channels while the total width of the ribs and channels is kept consonant as demonstrated in Fig. 24c, because of the higher anode volume for nitrogen and liquid water, similarly to the effect of the channel depth. Moreover, the nitrogen crossover rate is lower for wider channels, as shown in Fig. 24f, since the liquid accumulation under the ribs is lessened as the total width, $w_{rib} + w_{ch}$, is kept the same. Here, the effect of slower convective velocity in the channel is minor, as also seen for St_{ca}.

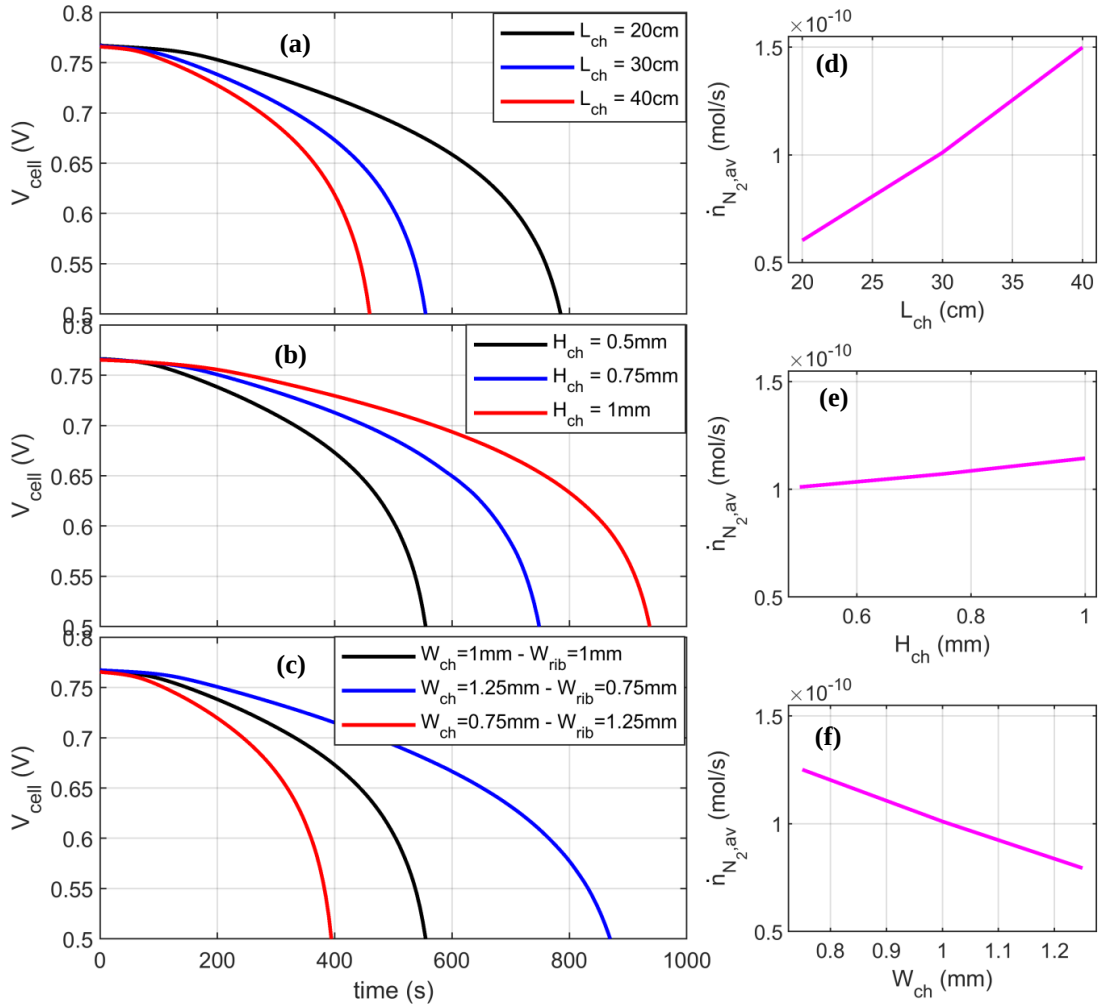

Figure 24: Effects of the geometric parameters: a) length of the channel, b) height of the channel, and c) widths of the channel and rib on the DEA performance; variation of the average nitrogen mole rate crossover the membrane versus d) length of the channel, e) height of the channel, and f) width of the channel

4.2.4. Carbon corrosion

The carbon corrosion reaction (CCR) takes place at the cathode CL because of the high over potential in the cathode that develops due to the oxygen reduction reaction (ORR) in the anode side where the hydrogen starvation occurs [73,85]. Abbou et al. [96] measured the CO_2 in the cathode exit stream to obtain the CCR rate at the cathode CL

assuming that CO_2 at the cathode exit comes from the CCR at the CL since the CCR at the GDL is negligible and the air supplied to the inlet was filtered with soda lime to remove CO_2 at the inlet.

Figure 25a shows the comparison of CO_2 concentrations at the cathode outlet during the DEA transient. Model results are compared with the experimental data reported by Abbou et al. [96]. A good agreement is seen between the model prediction and the experimental data except for the pick at the beginning of the cycle and gradual reduction to zero for 200 seconds, which Abbou et al. [96] proposed to be because of the rapid reduction of platinum oxides, [96], something not included in the model as platinum degradation is not considered. After the initial transient, the CCR gradually increases and promotes the degradation of the cell by the loss of electrochemical surface area (ECSA) [92]. Figure 25b shows the CCR along the channel in the direction of the anode flow at 150, 300, 450, and 540 seconds. The CCR is higher at the end of the anode channel where the hydrogen depletion starts first and causes an increase in the cathode interfacial potential, after which the CCR reaches its maximum level and remains constant, following the trend in the cathode interfacial potential shown in Fig. 22a.

Chen et al. [92] predicted the performance decay of the cell voltage during DEA operation via a power law relation based on the ratio of the remaining carbon and its initial level, which modifies the exchange current density of the ORR at the cathode CL. The same approach is used here assuming that the initial carbon load is 2 mg cm^{-2} as Abbou et al. [96] did not specify the carbon loading of the cell used in the experiments. The power factor is set to 2, as suggested by [92]. Then, the value of carbon loss factor, ε_C, is obtained as 0.979, i.e. about 2% carbon loss, after 818 cycles in 216 hours of DEA operation in the experiments [96]. A correction to the exchange current density of the ORR at the cathode CL by this factor, 0.979, does not affect the cell voltage notably. Moreover, even if this factor is decreased arbitrarily to even lower values, such as 0.5 and 0.1, the performance loss in the experiments cannot be predicted, as demonstrated in Fig. 26, since this approach only moves the polarization curve downward as its effect is solely on the cathode activation overpotential through the modification of the exchange current density.

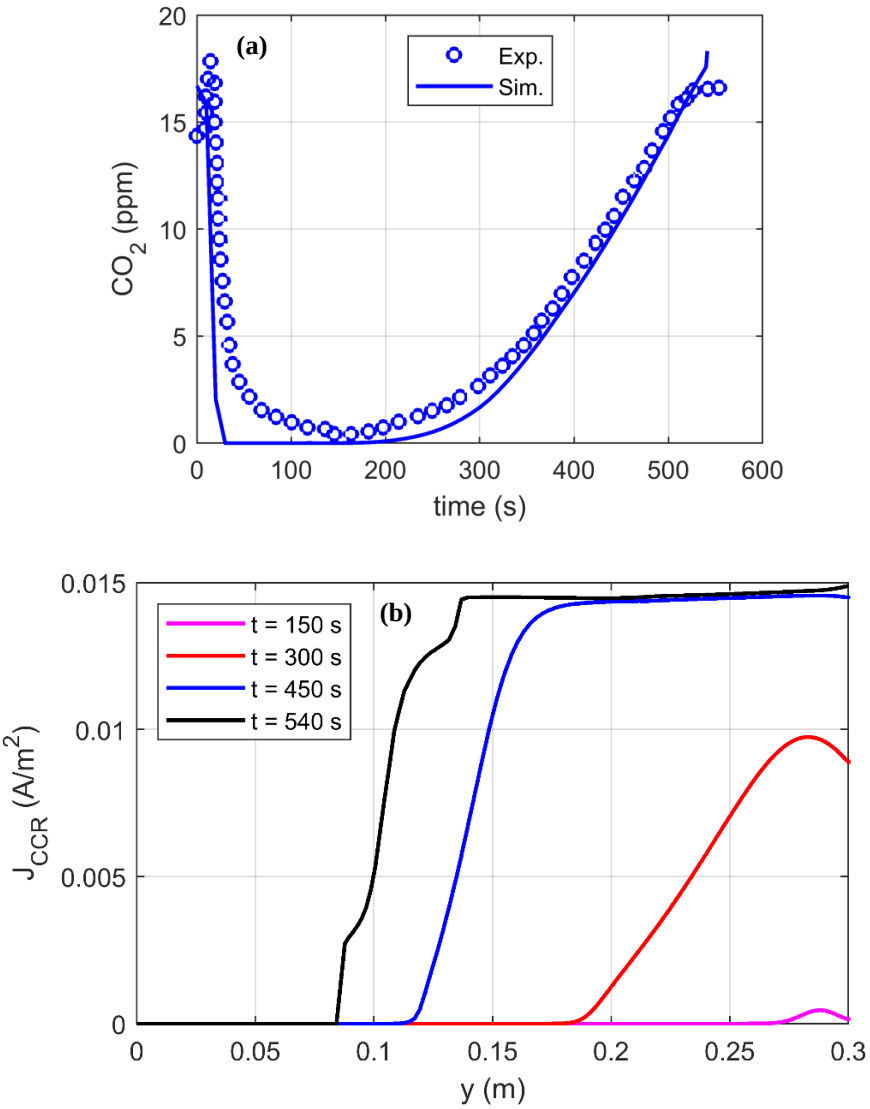

Figure 25: a) Comparison of the CO_2 concentrations at the cathode exit during a DEA cycle from the model and experimental data from [96]; and b) carbon corrosion rate along the channel from the anode inlet (y=0) to the anode outlet (y=0.3m)

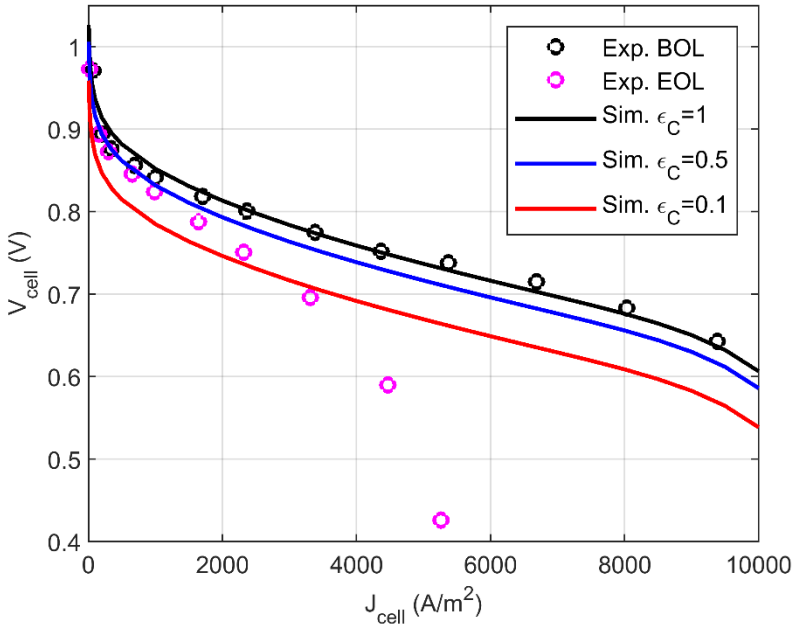

Figure 26: Polarization curves reported by [96] for the beginning of life (BOL) and end of live (EOL) conditions, and polarization curves from the model for the ε_C of 1, 0.5, and 0.1

The comparison of the polarization curves reported by [96] for the beginning of life (BOL) and end of life (EOL) in Fig. 26 indicates that performance loss is likely to be due to transport losses and morphological changes in the cathode CL. Kulikovsky [93] reported that oxygen diffusivity and proton conductivity of the cathode CL decrease dramatically due to the CCR based on a fitting study for the half-cell polarization equation for pristine and aged cells. The effects of the carbon corrosion on performance loss are not well-understood and cannot be studied without considering platinum degradation in the CL. Thus, the development of a complete model for the CL that considers the effects of aging is necessary and will be a part of our future work.

4.2.5. Anode bleeding

The anode bleeding (AB) operation mode uses an ultra-low flow at the anode exit to discharge nitrogen and liquid water from the anode flow field while limiting the disposal of

unused hydrogen to avoid hydrogen starvation and to achieve high utilization of hydrogen [45]. The bleeding rate can be optimized to attain a stable transient cell voltage and to avoid CCR at the cathode CL. Figures 27a and 27b show the effects of the AB rate on the cell voltage drop and the average CCR rate, respectively, for 2000 seconds and the load current density of 3300 A/m^2. The cell voltage drop is negligible if the anode outlet flow rate is more than 20 µl/min for which the hydrogen utilization is about 99.8%. Moreover, the carbon corrosion rate is negligible for an anode outlet flow rate as low as 15 µl/min, which means that the cathode interfacial potential is not increased to values of more than 1 V, the limiting potential used for the Langmuir isotherm, Eq. (103) [85]. Lastly, the severity of the voltage drops in the transient can be deemed as a good indicator of the carbon corrosion rate, especially at high cell potentials.

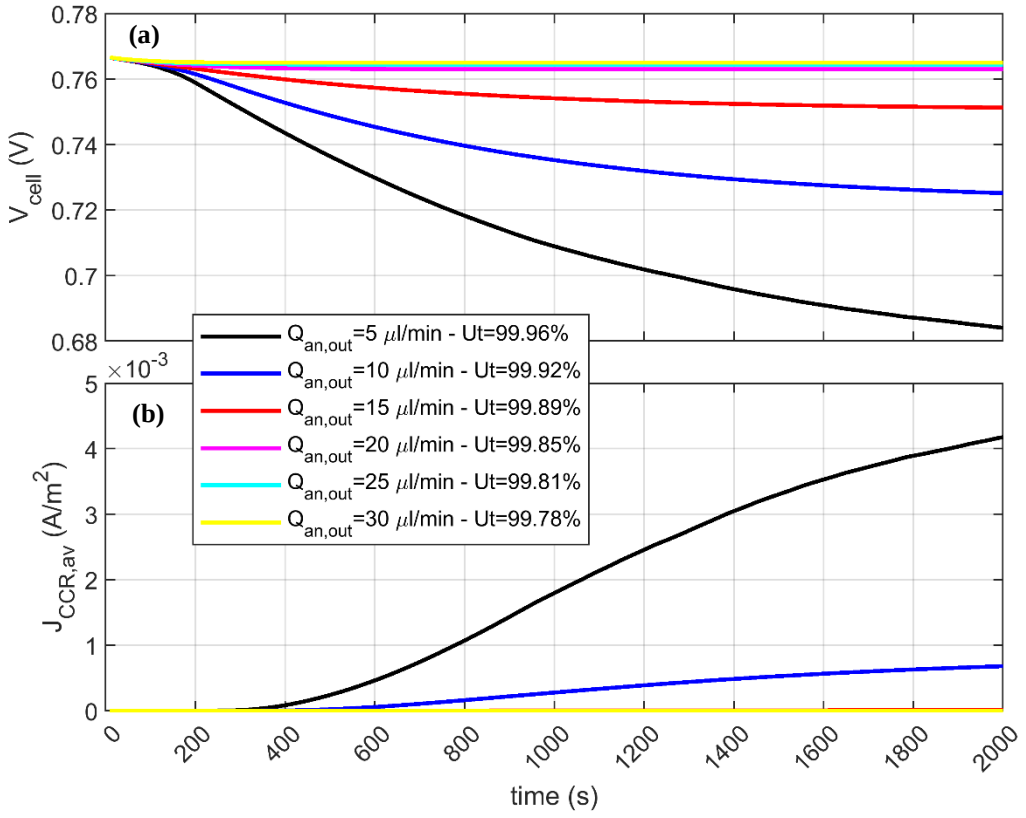

Figure 27: Effects of the anode bleeding rate on: a) cell voltage drop, and b) average carbon corrosion rate

Chapter 5

EFFECTS OF PEM FUEL CELL DEGRADATION ON THE TRANSPORT PROPERTIES OF THE CATHODE CATALYST LAYER

Low durability is a major issue against the commercialization of PEMFCs. Several mechanisms play an important role on the degradation of the cathode catalyst layer (CCL) by deteriorating the transport properties of reactants in the CCL mainly. In this chapter, the pseudo-three-dimensional (P3D) model developed in chapter 2 is used to study the effects of cell degradation on transport properties of the CCL. Accuracy of the model is verified by comparing the polarization curves from the model with the experimental ones reported by Spernjak et al. [129]. The model is used to investigate the effects of CCL transport properties and agglomerate parameters on cell performance. Results demonstrate that the cell performance is improved for thinner ionomer film around agglomerates, smaller agglomerates, higher exchange current density, lower transport resistance and higher proton conductivity of the CCL. The transport parameters of the CCL are varied to fit the polarization curves to the experimental ones for an accelerated stress test reported in [129]. Results demonstrate that the transport resistances of the CCL increase exponentially with the carbon loss in the CCL.

5.1. Methodology

The P3D model with two-phase and non-isothermal assumptions, developed in chapter 2, is considered for the simulations. Modified serpentine-channel flow fields with 5-pass channels and manifolds at the sides are used for both anode and cathode flow fields, as shown in Fig. 28. Flow fields are mirror images of each other with an active area of 50

cm^2. Anode and cathode flow fields are projected on a single surface to form the computational domain, as demonstrated in Fig. 28c.

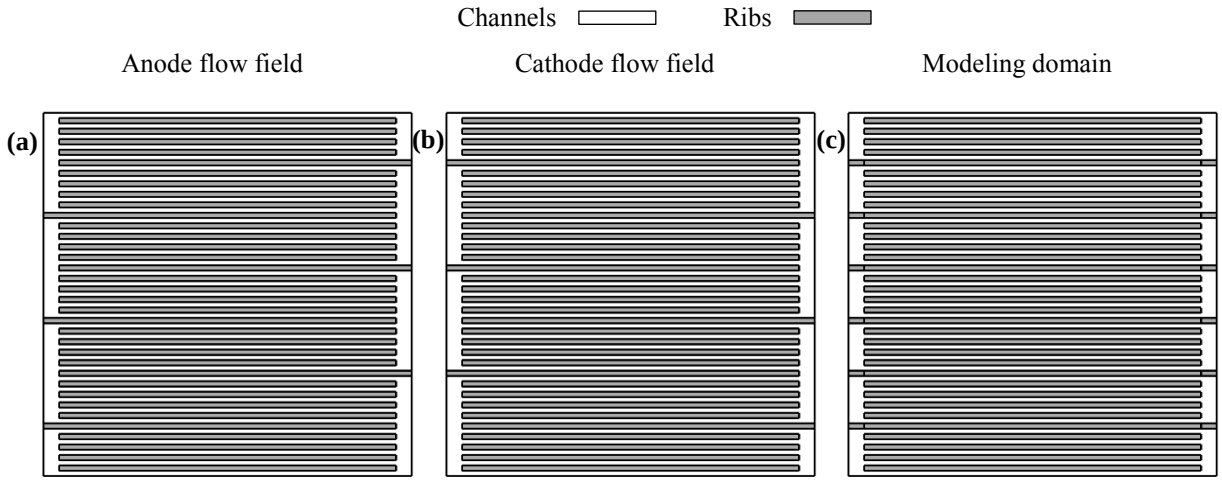

Figure 28: Flow fields (channels and ribs): (a) anode, (b) cathode, and (c) anode and cathode on a single surface which forms the modeling domain; anode and cathode inlets are at top right and left corners, respectively, and anode and cathode outlets are at bottom left and right corners, respectively

5.1.1. Governing equations

Brinkman equations are used to obtain the velocity field in the channels and GDLs, Maxwell-Stefan equations are used for the transport of the species by diffusion and advection, Butler-Volmer equations are used for the anode HOR, and an agglomerate model is used for the cathode ORR. Distribution and transport of the liquid water in the cathode GDL, dissolved water distribution and transport in the electrolyte phase, and temperature distribution in the channels and GDLs are included in the model as well. Detailed discussion of the governing equations can be found in chapter 2. Basic model parameters are the same as the ones given in Table 2, and geometric, operation, and model parameters modified for this study are listed in Table 13.

In chapter 2, the resistance of the CCL against the oxygen transport is defined based on the CL thickness, porosity, and diffusion coefficient, Eq. (61), and proton conductivity of the CL is defined based on the water content and temperature, Eq. (52). However, constant values are considered for them in this study as the aim is to determine their variations with the cell degradation, and it has been reported in recent studies that those definitions are not accurate enough, as mentioned by Karan [121].

Table 13: Geometric, operation, and model parameters

Parameter	Value	Description
w_{ch}	1×10^{-3} m	Channel width [130]
w_{rib}	1.03×10^{-3} m	Rib width [130]
w_{man}	3×10^{-3} m	Manifold width [130]
h_{ch}	1×10^{-3} m	Channel height [130]
h_{GDL}	2×10^{-4} m	GDL thickness [130]
δ_{CL}	7 and 12×10^{-6} m	Anode and cathode CLs thicknesses [130]
δ_m	18×10^{-6} m	Membrane thickness [130]
T	353 K	Operating temperature [129]
p	2.75 bar	Operating pressure [129]
$RH_{\{an,ca\}}$	1	Anode and cathode inlet relative humidity [129]
$St_{\{an,ca\}}$	1.2 and 2	Anode and cathode flow stoichiometric ratios [129]
$R_{O_2,CL}$	0.1 s m^{-1}	Resistance of the cathode CL against oxygen transport
σ_{CL}	4 S m^{-1}	Proton conductivity of the CL
$\alpha_{\{an,ca\}}$	1	Anodic and cathodic charge transfer coefficients
R_{solid}	3.5×10^{-6} Ω m^2	Electric resistance of the cell components
r_{agg}	1×10^{-7} m	Agglomerates radius [15]
δ_i	1×10^{-8} m	Ionomer film thickness around the agglomerates [15]

5.1.2. Boundary conditions

Inlet boundary conditions are constant flow rates calculated based on the flow stoichiometric ratios (Eqs. (77) and (78)), operating temperature, and mass fractions of the species calculated based on the inlet relative humidity (Eqs. (79) and (80)). Outlet boundary conditions are the operating pressure and outflow boundary conditions for the species, water saturation, and temperature (Eq. (81)). Moreover, no-slip, no-flux, and thermal insulation boundary conditions are applied to the walls of the computational domains.

5.1.3. Numerical approach

Brinkman, Maxwell-Stefan, Butler-Volmer, water saturation, dissolved water, and energy equations are coupled and solved numerically by the COMSOL Multiphysics software. Quadrangular mesh with linear elements is used to discretize the governing equations. The number of elements and degrees of freedom (DOF) are about 23 and 603.5 K. Fully-coupled solver with Newton iterations and direct MUMPS are used to solve the equations. The runtime of the simulations for each polarization curve is about 3 hours.

5.2. Results

5.2.1. Model validation

Accuracy of the model is verified by comparing the polarization curves from the model and the experimental data reported by Spernjak et al. [129]. Figure 29 shows a very good agreement between the polarization curves for the operation, geometric, and model parameters listed in Tables 13.

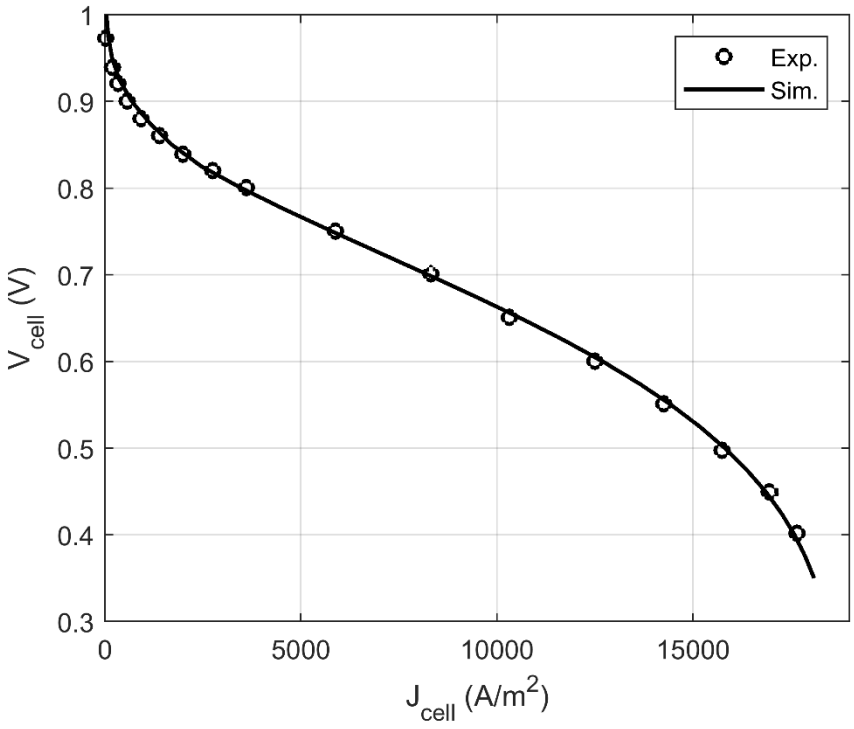

Figure 29: Comparison of the polarization curves from the simulations and the experimental data reported in [129]

5.2.2. Effects of the CL transport parameters on cell performance

In several studies, e.g. [74,75,79], it has been shown that carbon corrosion and platinum degradations at the CL make changes in the CL resistance against reactants transport, conductivity, and reaction kinetics. Figure 30 shows the effects of the CL resistance against oxygen transport, $R_{O_2,CL}$, proton conductivity of the CL, σ_{CL}, and exchange current density of ORR, $J_{0,ORR}$, on the polarization curve (cell performance). It is seen that $R_{O_2,CL}$ has an important effect on the limiting current density, σ_{CL} affects the ohmic part of the polarization curve by varying its slope, and $J_{0,ORR}$ moves the polarization curve downward due to its effect on the cathodic activation overpotential.

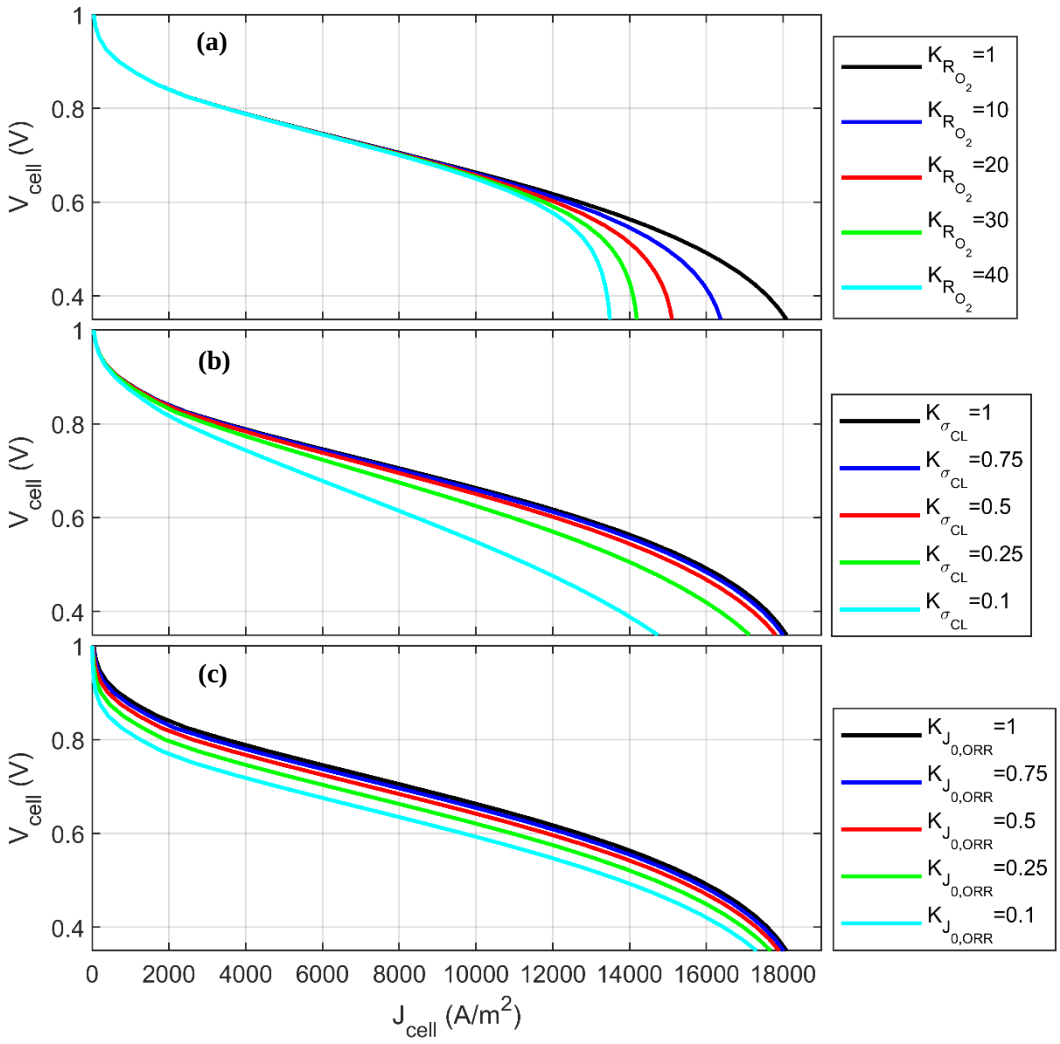

Figure 30: Polarization curves for different: a) resistance of the CL against oxygen transport, b) proton conductivity of the CL, and c) exchange current density of ORR; K is a coefficient that multiplies to these parameters for their variations

5.2.3. Effects of the agglomerate parameters on cell performance

In addition to the modifications in the transport properties according to the level of degradation in the CCL, the agglomerate parameters need to be modified as well. For instance, Pokhrel et al. [131] showed the agglomeration of the Pt/C and increase in the thickness of the ionomer film around the agglomerates by X-ray computed tomography of a

CL under degradation by an AST. Figure 31 shows the effects of the ionomer film thickness around the agglomerates, δ_i, and the agglomerates radius, r_{agg}, on the polarization curve (cell performance). The limiting current density is reduced for thicker ionomer films due to a longer pass for oxygen diffusion through the ionomer to reach the active sites for the ORR, as indicated in Eq. (33). Moreover, the cell performance is dropped for bigger agglomerates, which is because of the effect of the agglomerate radius on the effectiveness factor through changing Thiele modulus, as shown in Table 6.

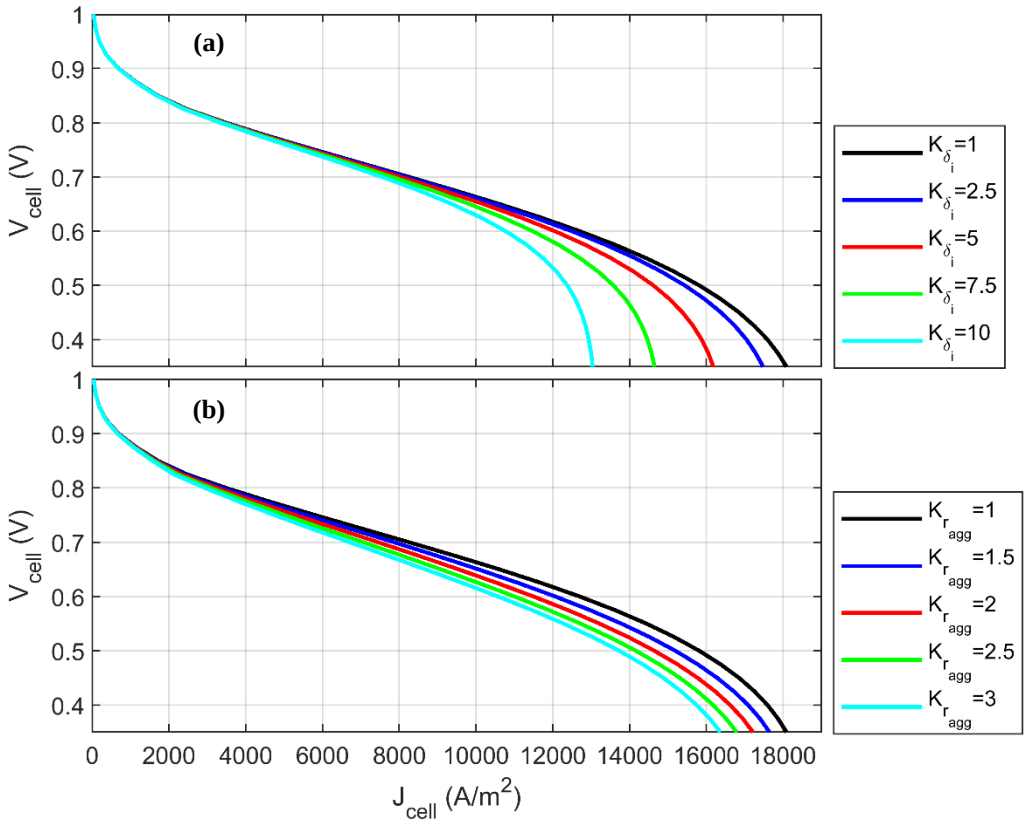

Figure 31: Polarization curves for different: a) ionomer film thickness around the agglomerates, and b) agglomerates radius; K is a coefficient that multiplies to these parameters for their variations

5.2.4. Variations of the CL transport parameters with carbon loss of CL

Polarization curves from the experiments during an AST, [129], show changes in all parts of the curve, i.e. activation, ohmic, and transportation losses, as shown in Fig. 32. $R_{O_2,CL}$, σ_{CL}, and $J_{0,ORR}$ are varied to capture the changes in the CL transport properties through matching the polarization curves. Agglomerate parameters are not varied here and their effects are considered in $R_{O_2,CL}$ as agglomerate parameters mostly affect the transportation part of the polarization curve, as shown in Fig. 31. Therefore, $R_{O_2,CL}$, σ_{CL}, and $J_{0,ORR}$ are varied to fit the changes in the transportation losses, the slope of the ohmic losses, and activation losses of the polarization curves, respectively.

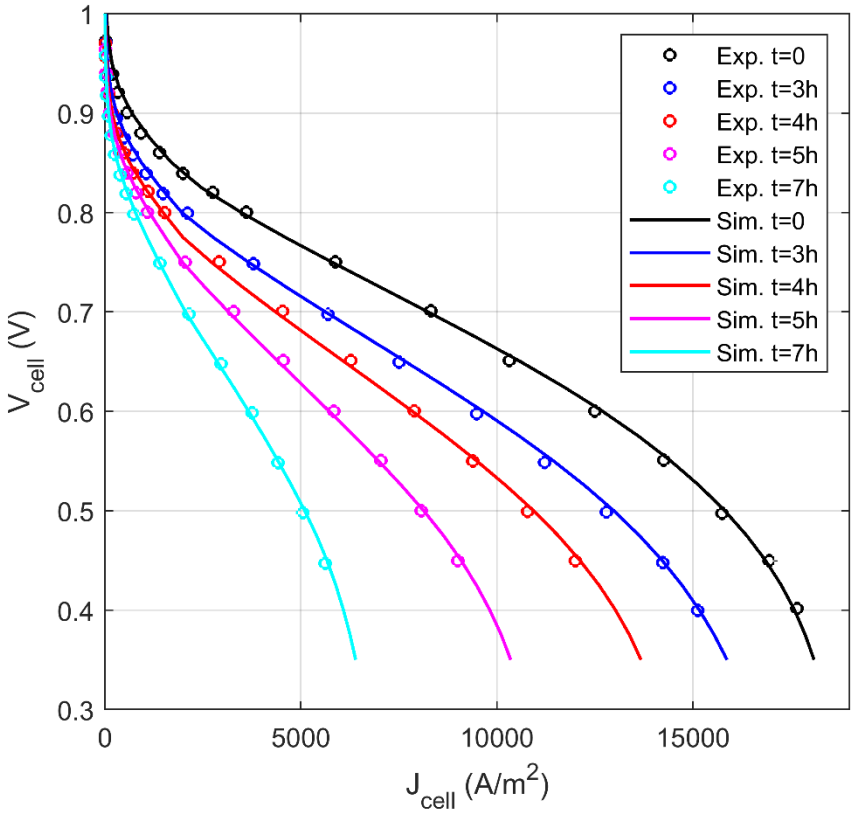

Figure 32: Comparisons of the polarization curves from the simulations and experiments, [129], at 0, 3, 4, 5, and 7 h

Figure 32 shows the comparisons of the polarization curves from the simulations and the experiments reported in [129] at 0, 3, 4, 5, and 7 h with a very good agreement between them. $R_{O_2,CL}$, σ_{CL}, and $J_{0,ORR}$ are varied to match the polarization curves and plotted versus the carbon loss in the CL in Fig. 33. Interestingly, variations of the transport parameters with the carbon loss are exponential, similar to the behavior reported in [94] for potential losses versus carbon losses.

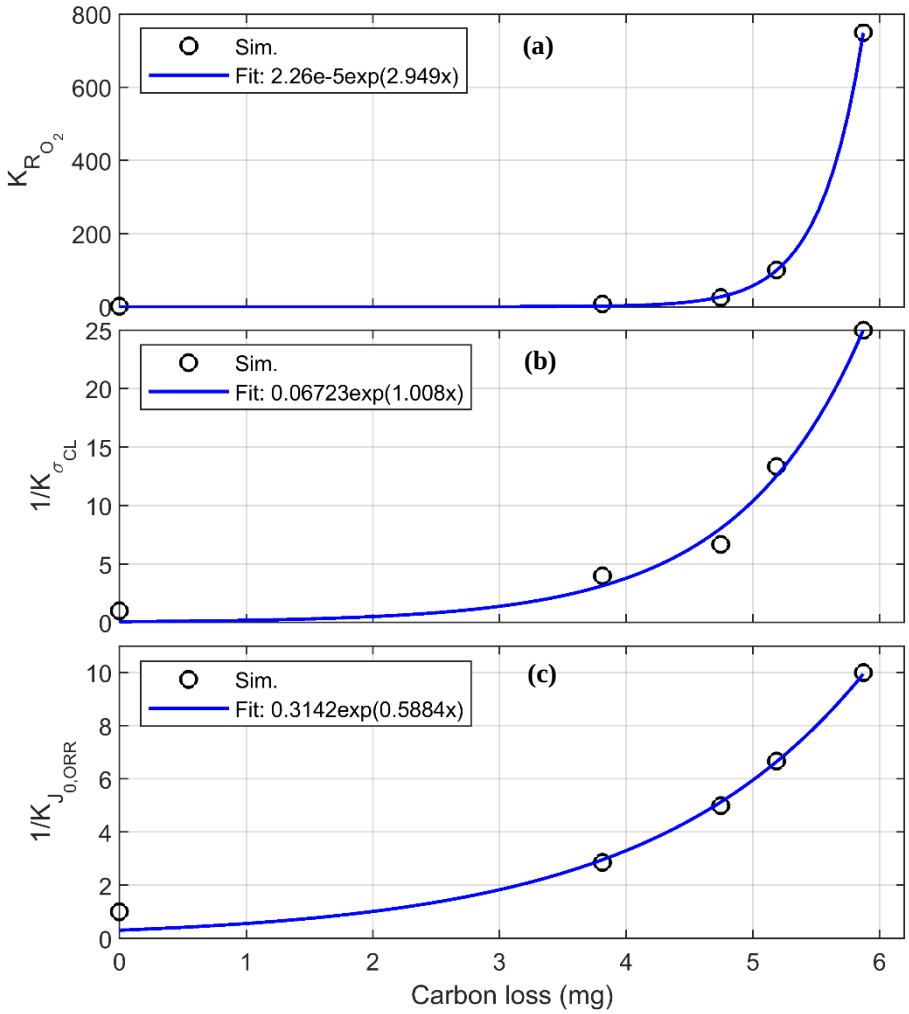

Figure 33: Variations of a) resistance of the CL against oxygen transport, b) proton conductivity of the CL, and c) exchange current density of ORR versus carbon loss of the CL; K is a coefficient that multiplies to these parameters for their variations

Chapter 6

CONCLUSION

Three dimensional (3D) model of the proton exchange membrane fuel cell (PEMFC) is necessary for the flow field design and analysis of the PEMFC. However, complete 3D models are computationally too expensive to conduct sensitivity analysis studies for a full cell. In-plane models based on resistance relationships for through-plane variations are advantageous as they can offer accurate results at reduced computational cost. In this dissertation, a pseudo-three-dimensional (P3D) model with two-phase and non-isothermal assumptions is developed for the analysis of the dead-ended anode (DEA) and anode bleeding (AB) operation modes and the cell degradation with carbon corrosion.

In chapter 2, the P3D model is developed and applied to a simple cell-portion that has straight channels at the anode and cathode sides. The model domain includes the anode and cathode channels and GDLs at the same plane, but solves for distributions of species, temperature, and liquid saturation as separate variable for each layer. Conservation equations including mass, momentum, species, charge, energy, liquid water, and dissolved water are included in the model for the transport and in-plane distributions of the velocity, species, current density, temperature, liquid water saturation, and dissolved water. Resistive relations are used in the through-plane direction. It is concluded that the developed P3D model, which is substantially faster than the 3D model, is very accurate based on the comparisons of polarization curves for variations of the height of the channel, GDL thickness, widths of the channels and ribs, operating temperature, and relative humidity of the reactant gases at the inlets against the ones obtained from the 3D model. Moreover, the comparisons of the in-plane distributions of the liquid water saturation, temperature, dissolved water, and species also demonstrate the accuracy of the approach qualitatively. A very good agreement is seen for both quantitative and qualitative comparisons of the P3D and 3D models.

In chapter 3, the P3D model is improved to a transient model with carbon corrosion to investigate the PEMFC performance under the AB operation mode. The model is validated by comparing its results with the experimental data including the polarization curves and the cell voltage transients during the DEA operation mode. The model is used to optimize the bleeding rate to achieve a stable transient cell voltage and avoid carbon corrosion while hydrogen utilization is kept at more than 99%. Moreover, the effects of the operating conditions on the cell performance under the AB operation mode are investigated. It is found that higher anode pressure, lower relative humidity (RH) of the reactants at the cathode inlet, lower cell temperature, and higher stoichiometric flow (St) for the cathode can improve the cell performance under the AB operation mode. Furthermore, the performance of the cells with the serpentine, straight, and interdigitated channels for the anode flow field and serpentine channels for the cathode flow field under the AB operation mode are investigated. Results demonstrated that the cell performance under the flow-through (FT) operation mode for both anode and cathode sides is almost the same for different flow field designs, while the cell with the serpentine channels for both anode and cathode flow fields has the best performance under the AB operation mode.

In chapter 4, the transient P3D model is used to investigate the effects of geometric and operation parameters on the cell voltage and carbon corrosion during the DEA and AB operation modes. The model is validated by comparisons with the experimental data reported in [96]. In addition to the polarization curves, cell voltage transients, local cathode and anode interfacial potentials and current densities, and the CO_2 concentration at the cathode exit are compared against the model. The model is used to investigate the effects of the load current density, anode pressure, RH of the cathode inlet, St of the cathode flow, and the cell temperature, as operation parameters; and the length, height, and width of the channel, as geometric parameters on the purge interval, which is the duration until the cell voltage drops to 0.5 V. It is found that lower load current density, higher anode pressure, lower relative humidity of the cathode inlet, higher stoichiometric flow ratio of the cathode, and shorter, deeper and wider channels can improve the DEA performance. Moreover, CO_2 concentration at the cathode outlet is evaluated based on the carbon corrosion rate at the cathode CL and compared with experimental measurements reported in [96]. Lastly, the

anode bleeding operation mode is studied to obtain an optimal bleeding rate to achieve a stable transient operation of the cell by avoiding cell voltage drop and carbon corrosion in the cell.

In chapter 5, the P3D-model is used to study the effects of the cell degradation on transport properties of the cathode CL. The model is validated by comparing the polarization curves with the experimental data reported in [129]. The model is used to investigate the effects of CL transport properties (resistance against oxygen transport, proton conductivity, and exchange current density of ORR) and agglomerate parameters (ionomer film thickness around the agglomerates and agglomerates radius) on the cell performance. It is found that thinner ionomer film, smaller agglomerates, higher exchange current density, lower transport resistance, and higher proton conductivity improve the cell performance. Transport parameters of the CL are varied to fit the polarization curves to the ones reported in [129] for an accelerated stress tests (AST). Results demonstrate that transport parameters of the cathode CL change exponentially with carbon loss of the CL.

Some future works are suggested as follows:

- Improving the liquid water transport model or using other two-phase models to predict the local effects of droplets more effectively.
- Developing a metric for the optimized bleeding rate per active area of the cell.
- Adding the platinum degradation to the P3D model.
- Improving the agglomerate model used for the ORR at the cathode CL
- Using the P3D model to develop a systematic degradation analysis for the effect of the carbon corrosion and platinum degradation at the cathode CL on the cell performance. The analysis will be done by defining the variations in the CL properties and parameters such as diffusivity, conductivity, thickness, porosity, electrochemical active surface area (ECSA), and agglomerate parameters as a function of the rates of the carbon corrosion and platinum degradation at the cathode CL.

REFERENCES

[1] Verhage, A. J., Coolegem, J. F., Mulder, M. J., Yildirim, M. H., & de Bruijn, F. A. (2013). 30,000 h operation of a 70 kW stationary PEM fuel cell system using hydrogen from a chlorine factory. international journal of hydrogen energy, 38(11), 4714-4724.

[2] Chen, H., Pei, P., & Song, M. (2015). Lifetime prediction and the economic lifetime of proton exchange membrane fuel cells. Applied Energy, 142, 154-163.

[3] He, W., Yi, J. S., & Van Nguyen, T. (2000). Two-phase flow model of the cathode of PEM fuel cells using interdigitated flow fields. AIChE Journal, 46(10), 2053-2064.

[4] Wang, Z. H., Wang, C. Y., & Chen, K. S. (2001). Two-phase flow and transport in the air cathode of proton exchange membrane fuel cells. Journal of power sources, 94(1), 40-50.

[5] Berg, P., Promislow, K., Pierre, J. S., Stumper, J., & Wetton, B. (2004). Water management in PEM fuel cells. Journal of the Electrochemical Society, 151(3), A341-A353.

[6] Kulikovsky, A. A. (2004). 1D+ 1D model of a DMFC: localized solutions and mixed potential. Electrochemistry communications, 6(12), 1259-1265.

[7] Freunberger, S. A., Santis, M., Schneider, I. A., Wokaun, A., & Büchi, F. N. (2006). In-plane effects in large-scale PEMFCs model formulation and validation. Journal of The Electrochemical Society, 153(2), A396-A405.

[8] Siegel, N. P., Ellis, M. W., Nelson, D. J., & Von Spakovsky, M. R. (2004). A two-dimensional computational model of a PEMFC with liquid water transport. Journal of Power Sources, 128(2), 173-184.

[9] Shah, A. A., Kim, G. S., Gervais, W., Young, A., Promislow, K., Li, J., & Ye, S. (2006). The effects of water and microstructure on the performance of polymer electrolyte fuel cells. Journal of Power Sources, 160(2), 1251-1268.

[10] Shah, A. A., Kim, G. S., Sui, P. C., & Harvey, D. (2007). Transient non-isothermal model of a polymer electrolyte fuel cell. Journal of Power Sources, 163(2), 793-806.

[11] Xing, L., Liu, X., Alaje, T., Kumar, R., Mamlouk, M., & Scott, K. (2014). A two-phase flow and non-isothermal agglomerate model for a proton exchange membrane (PEM) fuel cell. Energy, 73, 618-634.

[12] Berning, T., & Djilali, N. (2003). A 3D, multiphase, multicomponent model of the cathode and anode of a PEM fuel cell. Journal of the Electrochemical Society, 150(12), A1589-A1598.

[13] Hu, G., Fan, J., Chen, S., Liu, Y., & Cen, K. (2004). Three-dimensional numerical analysis of proton exchange membrane fuel cells (PEMFCs) with conventional and interdigitated flow fields. Journal of Power Sources, 136(1), 1-9.

[14] Ju, H., Meng, H., & Wang, C. Y. (2005). A single-phase, non-isothermal model for PEM fuel cells. International Journal of Heat and Mass Transfer, 48(7), 1303-1315.

[15] Ye, Q., & Van Nguyen, T. (2007). Three-dimensional simulation of liquid water distribution in a PEMFC with experimentally measured capillary functions. Journal of the Electrochemical Society, 154(12), B1242-B1251.

[16] Yesilyurt, S. (2007, January). Three-dimensional simulations of transient response of PEM fuel cells. In ASME 2007 International Mechanical Engineering Congress

and Exposition (pp. 597-605). American Society of Mechanical Engineers.

[17] Cordiner, S., Lanzani, S. P., & Mulone, V. (2011). 3D effects of water-saturation distribution on polymeric electrolyte fuel cell (PEFC) performance. international journal of hydrogen energy, 36(16), 10366-10375.

[18] Rostami, L., Nejad, P. M. G., & Vatani, A. (2016). A numerical investigation of serpentine flow channel with different bend sizes in polymer electrolyte membrane fuel cells. Energy, 97, 400-410.

[19] Karvonen, S., Hottinen, T., Saarinen, J., & Himanen, O. (2006). Modeling of flow field in polymer electrolyte membrane fuel cell. Journal of power sources, 161(2), 876-884.

[20] Iranzo, A., Munoz, M., Rosa, F., & Pino, J. (2010). Numerical model for the performance prediction of a PEM fuel cell. Model results and experimental validation. International Journal of Hydrogen Energy, 35(20), 11533-11550.

[21] Vazifeshenas, Y., Sedighi, K., & Shakeri, M. (2015). Numerical investigation of a novel compound flow-field for PEMFC performance improvement. International Journal of Hydrogen Energy, 40(43), 15032-15039.

[22] Macedo-Valencia, J., Sierra, J. M., Figueroa-Ramírez, S. J., Díaz, S. E., & Meza, M. (2016). 3D CFD modeling of a PEM fuel cell stack. International Journal of Hydrogen Energy, 41(48), 23425-23433.

[23] Rizvandi, O. B., & Yesilyurt, S. (2016, July). Design of Anode Flow Channels and Headers for a Large PEMFC Operating at Ultra-Low Stoichiometric Flow Conditions at the Anode Exit. In ASME 2016 14th International Conference on Nanochannels, Microchannels, and Minichannels collocated with the ASME 2016 Heat Transfer Summer Conference and the ASME 2016 Fluids Engineering Division Summer Meeting (pp. V001T13A002-V001T13A002). American Society

of Mechanical Engineers.

[24] Raj, A., & Shamim, T. (2014). Investigation of the effect of multidimensionality in PEM fuel cells. Energy Conversion and Management, 86, 443-452.

[25] Nandjou, F., Poirot-Crouvezier, J. P., Chandesris, M., & Bultel, Y. (2016). A pseudo-3D model to investigate heat and water transport in large area PEM fuel cells–Part 1: Model development and validation. International Journal of Hydrogen Energy, 41(34), 15545-15561.

[26] Rizvandi, O. B., & Yesilyurt, S. (2018, June). Modeling of Flow Distribution in Proton Exchange Membrane Fuel Cell. In ASME 2018 16th International Conference on Nanochannels, Microchannels, and Minichannels collocated with the ASME 2018 Heat Transfer Summer Conference and the ASME 2018 Fluids Engineering Division Summer Meeting. American Society of Mechanical Engineers.

[27] Jang, J. H., Yan, W. M., Chiu, H. C., & Lui, J. Y. (2015). Dynamic cell performance of kW-grade proton exchange membrane fuel cell stack with dead-ended anode. Applied Energy, 142, 108-114.

[28] Tsai, S. W., & Chen, Y. S. (2017). A mathematical model to study the energy efficiency of a proton exchange membrane fuel cell with a dead-ended anode. Applied energy, 188, 151-159.

[29] Xu, L., Fang, C., Li, J., Ouyang, M., & Lehnert, W. (2018). Nonlinear dynamic mechanism modeling of a polymer electrolyte membrane fuel cell with dead-ended anode considering mass transport and actuator properties. Applied Energy, 230, 106-121.

[30] Hu, Z., Yu, Y., Wang, G., Chen, X., Chen, P., Chen, J., & Zhou, S. (2016). Anode purge strategy optimization of the polymer electrode membrane fuel cell system

under the dead-end anode operation. Journal of Power Sources, 320, 68-77.

[31] Wang, B., Deng, H., & Jiao, K. (2018). Purge strategy optimization of proton exchange membrane fuel cell with anode recirculation. Applied Energy, 225, 1-13.

[32] Promislow, K., St-Pierre, J., & Wetton, B. (2011). A simple, analytic model of polymer electrolyte membrane fuel cell anode recirculation at operating power including nitrogen crossover. Journal of Power Sources, 196(23), 10050-10056.

[33] Bao, C., Ouyang, M., & Yi, B. (2006). Modeling and control of air stream and hydrogen flow with recirculation in a PEM fuel cell system—I. Control-oriented modeling. International journal of hydrogen energy, 31(13), 1879-1896.

[34] Bao, C., Ouyang, M., & Yi, B. (2006). Modeling and control of air stream and hydrogen flow with recirculation in a PEM fuel cell system—II. Linear and adaptive nonlinear control. International journal of hydrogen energy, 31(13), 1897-1913.

[35] Bao, C., Zhang, K., Ouyang, M., Yi, B., & Ming, P. (2006). Dynamic test and real-time control platform of anode recirculation for PEM fuel cell systems. Journal of fuel cell science and technology, 3(3), 333-345.

[36] Chen, J., Siegel, J. B., Stefanopoulou, A. G., & Waldecker, J. R. (2013). Optimization of purge cycle for dead-ended anode fuel cell operation. international journal of hydrogen energy, 38(12), 5092-5105.

[37] Chen, Y. S., Yang, C. W., & Lee, J. Y. (2014). Implementation and evaluation for anode purging of a fuel cell based on nitrogen concentration. Applied Energy, 113, 1519-1524.

[38] Hwang, J. J. (2013). Effect of hydrogen delivery schemes on fuel cell efficiency. Journal of Power Sources, 239, 54-63.

[39] Yang, Y., Zhang, X., Guo, L., & Liu, H. (2017). Overall and local effects of

operating conditions in PEM fuel cells with dead-ended anode. International Journal of Hydrogen Energy, 42(7), 4690-4698.

[40] Lee, Y., Kim, B., & Kim, Y. (2009). An experimental study on water transport through the membrane of a PEFC operating in the dead-end mode. International journal of hydrogen energy, 34(18), 7768-7779.

[41] Gomez, A., Raj, A., Sasmito, A. P., & Shamim, T. (2014). Effect of operating parameters on the transient performance of a polymer electrolyte membrane fuel cell stack with a dead-end anode. Applied Energy, 130, 692-701.

[42] Sasmito, A. P., & Mujumdar, A. S. (2011). Performance evaluation of a polymer electrolyte fuel cell with a dead-end anode: A computational fluid dynamic study. international journal of hydrogen energy, 36(17), 10917-10933.

[43] Ahluwalia, R. K., & Wang, X. (2007). Buildup of nitrogen in direct hydrogen polymer-electrolyte fuel cell stacks. Journal of Power Sources, 171(1), 63-71.

[44] Zhu, W. H., Payne, R. U., & Tatarchuk, B. J. (2006). Critical flow rate of anode fuel exhaust in a PEM fuel cell system. Journal of Power Sources, 156(2), 512-519.

[45] Eskin, M. G., & Yeşilyurt, S. (2019). Anode bleeding experiments to improve the performance and durability of proton exchange membrane fuel cells. International Journal of Hydrogen Energy.

[46] Rabbani, A., & Rokni, M. (2013). Effect of nitrogen crossover on purging strategy in PEM fuel cell systems. Applied energy, 111, 1061-1070.

[47] Steinberger, M., Geiling, J., Oechsner, R., & Frey, L. (2018). Anode recirculation and purge strategies for PEM fuel cell operation with diluted hydrogen feed gas. Applied Energy, 232, 572-582.

[48] Meyer, Q. P. G., Ashton, S., Curnick, O., Reisch, T., Adcock, P., Shearing, P. R., & Brett, D. J. (2014). Effect of Controlled Anode Flow Release on Dead-Ended

Anode Proton Exchange Membrane Fuel Cells. ECS Transactions, 61(27), 239-247.

[49] Ge, S. H., & Yi, B. L. (2003). A mathematical model for PEMFC in different flow modes. Journal of Power Sources, 124(1), 1-11.

[50] Maharudrayya, S., Jayanti, S., & Deshpande, A. P. (2005). Flow distribution and pressure drop in parallel-channel configurations of planar fuel cells. Journal of Power Sources, 144(1), 94-106.

[51] Maharudrayya, S., Jayanti, S., & Deshpande, A. P. (2006). Pressure drop and flow distribution in multiple parallel-channel configurations used in proton-exchange membrane fuel cell stacks. Journal of power sources, 157(1), 358-367.

[52] Kee, R. J., Korada, P., Walters, K., & Pavol, M. (2002). A generalized model of the flow distribution in channel networks of planar fuel cells. Journal of Power Sources, 109(1), 148-159.

[53] Jackson, J. M., Hupert, M. L., & Soper, S. A. (2014). Discrete geometry optimization for reducing flow non-uniformity, asymmetry, and parasitic minor loss pressure drops in Z-type configurations of fuel cells. Journal of Power Sources, 269, 274-283.

[54] Fahim, K. H., & Dhahad, E. M. A. H. A. Effect of Geometric Design of the Flow Fields Plat on the Performance of A PEM Fuel Cell: A.

[55] Koh, J. H., Seo, H. K., Lee, C. G., Yoo, Y. S., & Lim, H. C. (2003). Pressure and flow distribution in internal gas manifolds of a fuel-cell stack. Journal of Power Sources, 115(1), 54-65.

[56] Karimi, G., Baschuk, J. J., & Li, X. (2005). Performance analysis and optimization of PEM fuel cell stacks using flow network approach. Journal of Power Sources, 147(1-2), 162-177.

[57] Ma, Z., Jeter, S. M., & Abdel-Khalik, S. I. (2002). Flow network analysis

application in fuel cells. Journal of Power Sources, 108(1-2), 106-112.

[58] Zhang, W., Hu, P., Lai, X., & Peng, L. (2009). Analysis and optimization of flow distribution in parallel-channel configurations for proton exchange membrane fuel cells. Journal of Power Sources, 194(2), 931-940.

[59] Barreras, F., Lozano, A., Valino, L., Marin, C., & Pascau, A. (2005). Flow distribution in a bipolar plate of a proton exchange membrane fuel cell: experiments and numerical simulation studies. Journal of Power sources, 144(1), 54-66.

[60] Martin, D., Guinea, D. M., Moreno, B., Gonzalez, L., Garcia-Alegre, M. C., & Guinea, D. (2007). Electric modeling and image analysis of channel flow in bipolar plates. International journal of hydrogen energy, 32(10-11), 1572-1581.

[61] Nguyen, T. V. (1996). A Gas Distributor Design for Proton-Exchange-Membrane Fuel Cells. Journal of the Electrochemical Society, 143(5), L103-L105.

[62] Kumaran, R. M., Kumaraguruparan, G., & Sornakumar, T. (2013). Experimental and numerical studies of header design and inlet/outlet configurations on flow mal-distribution in parallel micro-channels. Applied Thermal Engineering, 58(1-2), 205-216.

[63] Wei, M., Fan, Y., Luo, L., & Flamant, G. (2015). CFD-based evolutionary algorithm for the realization of target fluid flow distribution among parallel channels. Chemical Engineering Research and Design, 100, 341-352.

[64] Guo, N., Leu, M. C., & Koylu, U. O. (2013). Network based optimization model for pin-type flow field of polymer electrolyte membrane fuel cell. International journal of hydrogen energy, 38(16), 6750-6761.

[65] Shimpalee, S., Greenway, S., & Van Zee, J. W. (2006). The impact of channel path length on PEMFC flow-field design. Journal of Power Sources, 160(1), 398-406.

[66] Shimpalee, S., & Van Zee, J. W. (2007). Numerical studies on rib & channel

dimension of flow-field on PEMFC performance. International Journal of Hydrogen Energy, 32(7), 842-856.

[67] Jeon, D. H., Greenway, S., Shimpalee, S., & Van Zee, J. W. (2008). The effect of serpentine flow-field designs on PEM fuel cell performance. International journal of hydrogen energy, 33(3), 1052-1066.

[68] Watkins, D. S., Dircks, K. W., & Epp, D. G. (1991). U.S. Patent No. 4,988,583. Washington, DC: U.S. Patent and Trademark Office.

[69] Watkins, D. S., Dircks, K. W., & Epp, D. G. (1992). U.S. Patent No. 5,108,849. Washington, DC: U.S. Patent and Trademark Office.

[70] Li, X., & Sabir, I. (2005). Review of bipolar plates in PEM fuel cells: Flow-field designs. International Journal of Hydrogen Energy, 30(4), 359-371.

[71] Wu, J., Yuan, X. Z., Martin, J. J., Wang, H., Zhang, J., Shen, J., ... & Merida, W. (2008). A review of PEM fuel cell durability: Degradation mechanisms and mitigation strategies. Journal of Power Sources, 184(1), 104-119.

[72] Pei, P., Chang, Q., & Tang, T. (2008). A quick evaluating method for automotive fuel cell lifetime. International Journal of Hydrogen Energy, 33(14), 3829-3836.

[73] Reiser, C. A., Bregoli, L., Patterson, T. W., Jung, S. Y., Yang, J. D., Perry, M. L., & Jarvi, T. D. (2005). A reverse-current decay mechanism for fuel cells. Electrochemical and Solid-State Letters, 8(6), A273-A276.

[74] Dubau, L., Castanheira, L., Maillard, F., Chatenet, M., Lottin, O., Maranzana, G., ... & ElKaddouri, A. (2014). A review of PEM fuel cell durability: materials degradation, local heterogeneities of aging and possible mitigation strategies. Wiley Interdisciplinary Reviews: Energy and Environment, 3(6), 540-560.

[75] Park, J. H., Yim, S. D., Kim, T., Park, S. H., Yoon, Y. G., Park, G. G., ... & Park, E. D. (2012). Understanding the mechanism of membrane electrode assembly

degradation by carbon corrosion by analyzing the microstructural changes in the cathode catalyst layers and polarization losses in proton exchange membrane fuel cell. Electrochimica Acta, 83, 294-304.

[76] Park, S., Shao, Y., Viswanathan, V. V., Liu, J., & Wang, Y. (2012). Non-kinetic losses caused by electrochemical carbon corrosion in PEM fuel cells. international journal of hydrogen energy, 37(10), 8451-8458.

[77] Fairweather, J. D., Spernjak, D., Weber, A. Z., Harvey, D., Wessel, S., Hussey, D. S., ... & Borup, R. L. (2013). Effects of cathode corrosion on through-plane water transport in proton exchange membrane fuel cells. Journal of The Electrochemical Society, 160(9), F980-F993.

[78] Liu, Z. Y., Brady, B. K., Carter, R. N., Litteer, B., Budinski, M., Hyun, J. K., & Muller, D. A. (2008). Characterization of carbon corrosion-induced structural damage of PEM fuel cell cathode electrodes caused by local fuel starvation. Journal of The Electrochemical Society, 155(10), B979-B984.

[79] Lin, R., Li, B., Hou, Y. P., & Ma, J. M. (2009). Investigation of dynamic driving cycle effect on performance degradation and micro-structure change of PEM fuel cell. International Journal of Hydrogen Energy, 34(5), 2369-2376.

[80] Zhang, T., Wang, P., Chen, H., & Pei, P. (2018). A review of automotive proton exchange membrane fuel cell degradation under start-stop operating condition. Applied energy, 223, 249-262.

[81] Shen, Q., Hou, M., Liang, D., Zhou, Z., Li, X., Shao, Z., & Yi, B. (2009). Study on the processes of start-up and shutdown in proton exchange membrane fuel cells. Journal of Power Sources, 189(2), 1114-1119.

[82] Hinds, G., & Brightman, E. (2012). In situ mapping of electrode potential in a PEM fuel cell. Electrochemistry Communications, 17, 26-29.

[83] Lamibrac, A., Maranzana, G., Lottin, O., Dillet, J., Mainka, J., Didierjean, S., ... & Moyne, C. (2011). Experimental characterization of internal currents during the start-up of a proton exchange membrane fuel cell. Journal of Power Sources, 196(22), 9451-9458.

[84] Lamibrac, A., Maranzana, G., Dillet, J., Lottin, O., Didierjean, S., Durst, J., ... & Chatenet, M. (2012). Local degradations resulting from repeated start-ups and shut-downs in proton exchange membrane fuel cell (PEMFC). Energy Procedia, 29, 318-324.

[85] Meyers, J. P., & Darling, R. M. (2006). Model of carbon corrosion in PEM fuel cells. Journal of the Electrochemical Society, 153(8), A1432-A1442.

[86] Tang, H., Qi, Z., Ramani, M., & Elter, J. F. (2006). PEM fuel cell cathode carbon corrosion due to the formation of air/fuel boundary at the anode. Journal of Power Sources, 158(2), 1306-1312.

[87] Lin, R., Cui, X., Shan, J., Técher, L., Xiong, F., & Zhang, Q. (2015). Investigating the effect of start-up and shut-down cycles on the performance of the proton exchange membrane fuel cell by segmented cell technology. International Journal of Hydrogen Energy, 40(43), 14952-14962.

[88] Patterson, T. W., & Darling, R. M. (2006). Damage to the cathode catalyst of a PEM fuel cell caused by localized fuel starvation. Electrochemical and Solid-State Letters, 9(4), A183-A185.

[89] Liu, Z., Yang, L., Mao, Z., Zhuge, W., Zhang, Y., & Wang, L. (2006). Behavior of PEMFC in starvation. Journal of power sources, 157(1), 166-176.

[90] Baumgartner, W. R., Parz, P., Fraser, S. D., Wallnöfer, E., & Hacker, V. (2008). Polarization study of a PEMFC with four reference electrodes at hydrogen starvation conditions. Journal of Power Sources, 182(2), 413-421.

[91] Hu, J., Sui, P. C., Kumar, S., & Djilali, N. (2009). Modelling and simulations of carbon corrosion during operation of a polymer electrolyte membrane fuel cell. Electrochimica Acta, 54(23), 5583-5592.

[92] Chen, J., Siegel, J. B., Matsuura, T., & Stefanopoulou, A. G. (2011). Carbon corrosion in PEM fuel cell dead-ended anode operations. Journal of The Electrochemical Society, 158(9), B1164-B1174.

[93] Kulikovsky, A. A. (2014). Understanding Catalyst Layer Degradation in PEM Fuel Cell Through Polarization Curve Fitting. Electrocatalysis, 5(3), 221-225.

[94] Dhanushkodi, S. R., Kundu, S., Fowler, M. W., & Pritzker, M. D. (2014). Use of mechanistic carbon corrosion model to predict performance loss in Polymer Electrolyte Membrane fuel cells. Journal of Power Sources, 267, 171-181.

[95] Rizvandi, O. B., & Yesilyurt, S. (2019). A pseudo three-dimensional, two-phase, non-isothermal model of proton exchange membrane fuel cell. Electrochimica Acta, 302, 180-197.

[96] Abbou, S., Dillet, J., Maranzana, G., Didierjean, S., & Lottin, O. (2017). Local potential evolutions during proton exchange membrane fuel cell operation with dead-ended anode–Part I: Impact of water diffusion and nitrogen crossover. Journal of Power Sources, 340, 337-346.

[97] Sadeghifar, H., Djilali, N., & Bahrami, M. (2014). Effect of Polytetrafluoroethylene (PTFE) and micro porous layer (MPL) on thermal conductivity of fuel cell gas diffusion layers: Modeling and experiments. Journal of Power Sources, 248, 632-641.

[98] El-kharouf, A., Mason, T. J., Brett, D. J., & Pollet, B. G. (2012). Ex-situ characterisation of gas diffusion layers for proton exchange membrane fuel cells. Journal of Power Sources, 218, 393-404.

[99] Cao, T. F., Lin, H., Chen, L., He, Y. L., & Tao, W. Q. (2013). Numerical investigation of the coupled water and thermal management in PEM fuel cell. Applied energy, 112, 1115-1125.

[100] Xing, L., Song, X., Scott, K., Pickert, V., & Cao, W. (2013). Multi-variable optimisation of PEMFC cathodes based on surrogate modelling. international journal of hydrogen energy, 38(33), 14295-14313.

[101] Brinkman, H. C. (1949). A calculation of the viscous force exerted by a flowing fluid on a dense swarm of particles. Applied Scientific Research, 1(1), 27-34.

[102] Shi, Z., & Wang, X. (2007, October). Comparison of Darcy's law, the Brinkman equation, the modified NS equation and the pure diffusion equation in PEM fuel cell modeling. In COMSOL Conference.

[103] Vasil'ev, A. (2009). From the Hele-Shaw experiment to integrable systems: a historical overview. Complex analysis and operator theory, 3(2), 551-585.

[104] Bird, R. B., Stewart, W. E., & Lightfoot, E. N. (2002). Transport phenomena. 2nd. New York.

[105] Petersen, E. E. (1958). Diffusion in a pore of varying cross section. AIChE Journal, 4(3), 343-345.

[106] Yesilyurt, S., Siegel, J. B., & Stefanopoulou, A. G. (2012). Modeling and experiments of voltage transients of polymer electrolyte membrane fuel cells with the dead-ended anode. Journal of Fuel Cell Science and Technology, 9(2), 021012.

[107] Wang, X., & Van Nguyen, T. (2010). Modeling the effects of the microporous layer on the net water transport rate across the membrane in a PEM Fuel Cell. Journal of The Electrochemical Society, 157(4), B496-B505.

[108] Ge, S., Li, X., Yi, B., & Hsing, I. M. (2005). Absorption, desorption, and transport of water in polymer electrolyte membranes for fuel cells. Journal of the

Electrochemical Society, 152(6), A1149-A1157.

[109] Sonntag, R. E., Borgnakke, C., Van Wylen, G. J., & Van Wyk, S. (1998). Fundamentals of thermodynamics (Vol. 6). New York: Wiley.

[110] Jomori, S., Nonoyama, N., & Yoshida, T. (2012). Analysis and modeling of PEMFC degradation: Effect on oxygen transport. Journal of Power Sources, 215, 18-27.

[111] Froment, G. F., Bischoff, K. B., & De Wilde, J. (1990). Chemical reactor analysis and design (Vol. 2). New York: Wiley.

[112] Lin, G., He, W., & Van Nguyen, T. (2004). Modeling liquid water effects in the gas diffusion and catalyst layers of the cathode of a PEM fuel cell. Journal of the Electrochemical Society, 151(12), A1999-A2006.

[113] Siegel, J. B., Bohac, S. V., Stefanopoulou, A. G., & Yesilyurt, S. (2010). Nitrogen front evolution in purged polymer electrolyte membrane fuel cell with dead-ended anode. Journal of the Electrochemical Society, 157(7), B1081-B1093.

[114] You, L., & Liu, H. (2002). A two-phase flow and transport model for the cathode of PEM fuel cells. International journal of heat and mass transfer, 45(11), 2277-2287.

[115] Ebrahimi, S., Ghorbani, B., & Vijayaraghavan, K. (2017). Optimization of catalyst distribution along PEMFC channel through a numerical two-phase model and genetic algorithm. Renewable Energy, 113, 846-854.

[116] Ferreira, R. B., Falcão, D. S., Oliveira, V. B., & Pinto, A. M. F. R. (2017). 1D+ 3D two-phase flow numerical model of a proton exchange membrane fuel cell. Applied Energy, 203, 474-495.

[117] Ji, M., & Wei, Z. (2009). A review of water management in polymer electrolyte membrane fuel cells. Energies, 2(4), 1057-1106.

[118] Jiao, K., & Li, X. (2011). Water transport in polymer electrolyte membrane fuel cells. Progress in energy and combustion Science, 37(3), 221-291.

[119] He, M., Huang, Z., Sun, P., & Wang, C. (2013). Modeling and numerical studies for a 3D two-phase mixed-domain model of PEM fuel cell. Journal of The Electrochemical Society, 160(4), F324-F336.

[120] Zhang, G., & Jiao, K. (2018). Multi-phase models for water and thermal management of proton exchange membrane fuel cell: A review. Journal of Power Sources, 391, 120-133.

[121] Karan, K. (2017). PEFC catalyst layer: Recent advances in materials, microstructural characterization, and modeling. Current Opinion in Electrochemistry, 5(1), 27-35.

[122] Shim, H. K., Paul, D. K., & Karan, K. (2015). Resolving the contradiction between anomalously high water uptake and low conductivity of nanothin Nafion films on SiO2 substrate. Macromolecules, 48(22), 8394-8397.

[123] Morawietz, T., Handl, M., Friedrich, K. A., & Hiesgen, R. (2018). Structure, Properties, and Degradation of Ultrathin Ionomer Films in Catalytic Layers of Fuel Cells. ECS Transactions, 86(13), 179-191.

[124] Muzaffar, T., Kadyk, T., & Eikerling, M. (2017). Physical Modeling of the Proton Density in Nanopores of PEM Fuel Cell Catalyst Layers. Electrochimica Acta, 245, 1048-1058.

[125] Chun, J. H., Park, K. T., Jo, D. H., Kim, S. G., & Kim, S. H. (2011). Numerical modeling and experimental study of the influence of GDL properties on performance in a PEMFC. international journal of hydrogen energy, 36(2), 1837-1845.

[126] Wang, X. D., Duan, Y. Y., & Yan, W. M. (2007). Numerical study of cell

performance and local transport phenomena in PEM fuel cells with various flow channel area ratios. Journal of Power Sources, 172(1), 265-277.

[127] Ozen, D. N., Timurkutluk, B., & Altinisik, K. (2016). Effects of operation temperature and reactant gas humidity levels on performance of PEM fuel cells. Renewable and Sustainable Energy Reviews, 59, 1298-1306.

[128] Lee, S. K., Ito, K., Ohshima, T., Noda, S., & Sasaki, K. (2009). In situ measurement of temperature distribution across a proton exchange membrane fuel cell. Electrochemical and Solid-State Letters, 12(9), B126-B130.

[129] Spernjak, D., Fairweather, J., Mukundan, R., Rockward, T., & Borup, R. L. (2012). Influence of the microporous layer on carbon corrosion in the catalyst layer of a polymer electrolyte membrane fuel cell. Journal of Power Sources, 214, 386-398.

[130] Carnes, B., Spernjak, D., Luo, G., Hao, L., Chen, K. S., Wang, C. Y., ... & Borup, R. L. (2013). Validation of a two-phase multidimensional polymer electrolyte membrane fuel cell computational model using current distribution measurements. Journal of Power Sources, 236, 126-137.

[131] Pokhrel, A., El Hannach, M., Orfino, F. P., Dutta, M., & Kjeang, E. (2016). Failure analysis of fuel cell electrodes using three-dimensional multi-length scale X-ray computed tomography. Journal of Power Sources, 329, 330-338.